Study and Optimisation of Undulator-based Polarised Positron Sources for Linear Colliders

Thesis submitted in accordance with the requirements of the University of Liverpool for the degree of Doctor in Philosophy by

Lei Zang

September 2010

Abstract

High-energy accelerators play an important role in physics research. The International Linear Collider (ILC) and Compact Linear Collider (CLIC) are proposed future accelerators which will require of order 10^{14} positrons per second to fulfil their luminosity requirements. In addition, polarisation of the positron beam will increase the scope of the physics studies that can be performed using a linear collider. Production of large quantities of polarised positrons is one of the major challenges for the research, development and design of any future linear collider. A polarised positron source based on gamma rays produced by a high energy electron beam in a helical undulator has been selected as the baseline option for ILC. The design is relatively mature, and previous studies have shown that it should be capable of producing the required positron beam intensity and polarisation. We review the design using a range of analytical and simulation tools. We also consider, in more detail than in previous studies, two options for the design of a photon collimator that could be used to improve the positron polarisation. Although a Compton source is presently the baseline choice for the positron source for CLIC, an undulator-based scheme remains an option. We discuss the possibility of an undulator-based polarised positron source for CLIC Stage 1 (500 GeV centre of mass collision energy), and consider options for an undulator-based positron source in the upgrade to Stage 2 (3 TeV centre of mass collision energy). For both ILC and CLIC, energy deposition from the gamma rays striking the positron production target is a concern. For ILC, the energy density can be reduced by rotating the target at high speed; however, this raises concerns about the eddy currents induced by the strong field of the matching device. We report the results of experiments at Daresbury Laboratory to understand the eddy current effects, and to validate models for predicting the effects in the final system.

Acknowledgements

First and foremost I offer my heartfelt gratitude to my supervisor, Dr. Andy Wolski, who has supported me throughout my thesis with his patience and knowledge whilst allowing me the room to work in my own way. I also owe my deepest gratitude to Dr. Ian Bailey, who gave steadfast support and invaluable advice through the four years of the research. The thesis would not have been completed or written without their encouragement and effort.

There are many other people who have helped me over the years I have been studying for this PhD. Especially my acknowledgements go to Prof. Jim Clarke and Dr Louis Rinolfi for their willingness to share their knowledge. They have always been helpful, encouraging and knowledgeable. Thanks also to Prof. Neil Marks for organising lectures in past few years, which gave me tools that turned out to be essential in my PhD research.

I would also like to thank our colleges from DESY Zeuthen, Andriy Ushakov and Andreas Schaelicke for making their software available so I was able to use it in this work.

All members of University of Liverpool accelerator group and Cockcroft Institute have always shown a constant interest in the study and provided a lot of encouragement. Thanks to Luis Fernandez-Hernando, Duncan Scott, Ian Shinton, Praveen Ambattu, Julian McKenzie, Larisa Malysheva, Yoel Giboudot and Kosmas Panagiotidis for all kinds of interesting discussions and valuable suggestions.

Finally, I would like to thank my family, my mother ShuYu Zheng, my father QingBo Zang and my wonderful wife, Qun Yang. Thanks for supporting me during my studies and urging me on. To all of you, thanks for always being there for me.

Contents

List of Figures

List of Tables

LIST OF TABLES

1

Introduction: Positron Sources for Accelerators

1.1 Background: Particle Accelerators

Why do we need to build accelerators? Simply, an accelerator is an instrument for researching and knowing the microcosmic world. What is the composition of our boundless universe? In all ages, people keep thinking about and exploring this question. Ancient philosophers can only deduce the answer based on the natural phenomena which they can feel they can see. For instance, the Greek philosopher Aristotle believed that all objects in the world consisted of four fundamental elements: earth, water, fire and air. China also had that kind of description, but instead of four they believed there were five fundamental elements, with gold as the extra one. Human society evolved over thousands of years to arrive at modern life. Along with technological developments, people started to use more reliable methods – experiments – to validate their thinking. Particle accelerators are a bit like extremely powerful microscopes. They use high voltages to accelerate particles to high energies so that their wavelengths get smaller. An accelerator is a device that produces beams of particles, with controllable:

1. intensity (number of particles/unit time);
2. energy;
3. energy spread;
4. transverse (with respect to its velocity) size;

5. angular spread.

1.2 Accelerator Overview

Since the 1920's high-energy accelerators have played a more and more important role in the research of fundamental particles and their interactions [1]. There are now several thousands of particle accelerators in the world. They are spread across many different fields such as industry, medicine and chemistry. But there are still also accelerators that are built in laboratories dedicated to academic research. For that purpose, the most advanced device is the collider, which accelerates two beams of particles to high energy and then lets them impact against each other. By observing and analysing the results of the collision, scientists find new particles and understand new phenomena [2]. In order to achieve higher energies, these machines have become progressively larger and more complex over time as shown in Fig. 1.1 [3]. There are several kinds of colliders, which may be classified according to the beams of particles they collide, such as proton-proton, proton-antiproton, electron-positron, etc. In this thesis, we will focus on electron-positron linear colliders. In the following sections of this chapter, some examples of electron-positron colliders over the past 50 years are briefly described, starting with the world's first electron-positron collider – AdA [4] – and moving on to the electron-positron collider in China (the Beijing Electron-Positron Collider, BEPC [5]), the world's largest electron positron collider, LEP and the first (also the only) linear collider the SLAC Linear Collider – SLC.

1.2.1 The First Electron-Positron Collider – AdA

The history of the electron-positron collider begins in 1960 at the Frascati National Laboratory, LNF. The first electron-positron collider project, Anello di Accumulazione (AdA), shown in Fig. 1.2 [3], was proposed by Bruno Touschek. AdA consisted of a storage ring for an electron and a positron beam rotating in opposite directions on the same trajectory, with collision beam energy of $2 \times 220\,\mathrm{MeV}$. A first stored beam of few electrons was obtained at the end of May 1961, using the Frascati Electron Synchrotron as an injector. AdA was capable of keeping particles up to 0.25 GeV on a circular orbit of 65 cm radius. A radio frequency cavity with a longitudinal field oscillating at 147 MHz with a peak voltage of 5 kV compensated the energy loss due

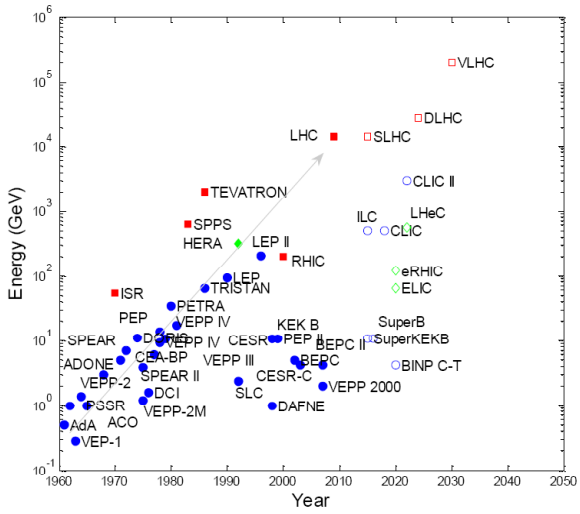

Figure 1.1: Centre of mass energies in colliders, history and future prospect. Full symbol: past and present project. Empty symbols: future. Blue: leptons, Red: hadrons, Green: leptons-hadrons.

Table 1.1: AdA parameters.

Maximum c.o.m. energy	0.5 GeV
Radius	65 cm
Status	Active from 1962 to 1965

to synchrotron radiation emission from the stored particles. Four years later, Frascati gave the first measurable luminosity value of $10^{25}\,\mathrm{cm}^{-2}\mathrm{sec}^{-1}$, which demonstrated the feasibility of the technology. In fact, after Anderson's discovery of the positron, this was the first time positrons had been used in collider. The method of producing the positron beam in AdA became known as a "conventional" positron source. First of all, an electron beam struck an external target to produce bremsstrahlung gamma rays that entered the collider ring; the gamma rays then struck a metallic target (a thin tantalum sheet) that converted the gamma rays to electron-positron pairs.

AdA opened another door to accelerator science: electron-positron colliders become a powerful tool in many high-energy physics laboratories. AdA detected the single photon production from an electron-positron interaction (single beam-beam bremsstrahlung): the rate of such events was found to be in agreement with the calculated cross section and storage ring parameters. Although AdA did not make any new discoveries, it

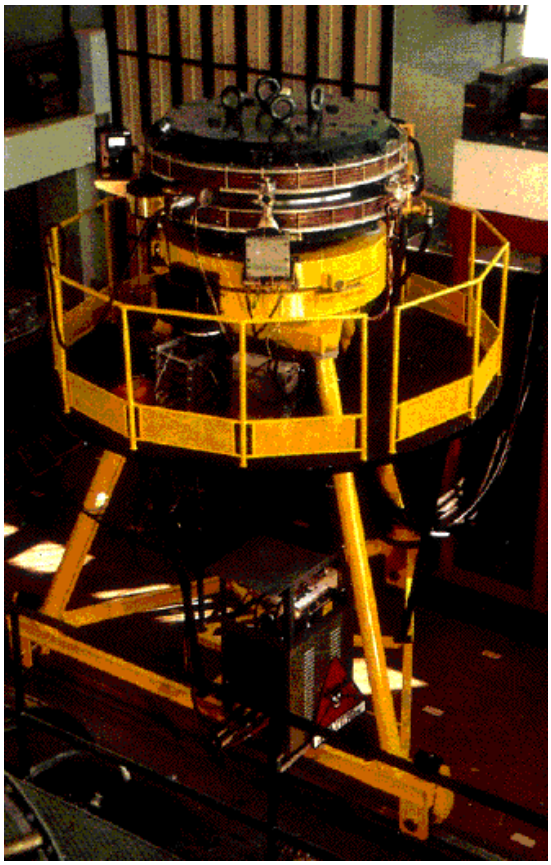

Figure 1.2: AdA: the first electron-positron collider.

revolutionised the use of accelerators in high-energy physics. It led to a rapid growth in the interest and development of electron-positron colliders, with more ambitious parameters, which in turn led to further research about positron sources.

1.2.2 The Chinese Electron-Positron Collider BEPC

The Beijing Electron-Positron Collider (BEPC) is a high energy accelerator designed for both high energy physics experiments and synchrotron radiation applications. It was proposed and designed in 1982, and was the first high energy particle accelerator to be built in China [6]. There are four main parts in the machine, including a 1.4 GeV electron and positron linac, a 2.2-2.8 GeV storage ring, a magnetic spectrometer for the high energy physics experiments, and synchrotron radiation facilities. Electrons are generated by an electron gun and then injected into the linac which is 202 m long. When the electron beam is accelerated to an energy of 150 MeV, the beam strikes a 10 mm tungsten target to create electromagnetic cascade showers. Electrons, positrons and photons are generated and are emitted from the target. The positrons are focused and captured, and accelerated to higher energy, to produce the positron beam for later collision. After the linac, there is a storage ring with circumference 240.4 m. The shape of the ring consists of two long straight sections of 27.4 m and two approximately semi-circular arcs. There is an interaction point in the middle of one long straight section. When the electrons and positrons are injected into the ring, the beam is accumulated until we obtain sufficient numbers of particle, and then the energy is ramped. The electron and positron beams are accelerated to the operating energy. Finally, the magnetic fields are maintained at constant levels, and the beams start to collide. The BEPC storage ring is refilled with electron and positron beams every 4–6 hours.

BEPC-II is an upgrade project of BEPC, and achieved its first collisions in 2008. There are two storage rings in the tunnel, so that electron and positron beams stay in their own ring. The luminosity that can be achieved is two orders of magnitude higher than the BEPC, up to $10^{33}\,\mathrm{cm}^{-2}\mathrm{s}^{-1}$. A comparison between the BEPC and BEPC-II parameters is shown in Table 1.2.

The positron source is an extremely important system in BEPC-II to produce sufficient positrons in order to achieve the goal of two orders of magnitude higher luminosity. Comparing with the BEPC, the injection rate needs to be at least 50 mA/min, which is approximately ten times that of the old system. The BEPC-II positron source is a

Table 1.2: BEPC and BEPC-II parameters.

	BEPC-II	BEPC
Energy (GeV)	1.0 – 2.1	1.0 – 2.5
circumference (m)	237.5	240.4
β_x^*/β_y^* (cm)	100/1.5	120/5
Number of bunches (N_b)	93	1
Beam intensity ($E = 1.89\,\mathrm{GeV}$)	2×910	2×35
Luminosity ($E = 1.89\,\mathrm{GeV}$) ($10^{33}\,\mathrm{cm}^{-2}\mathrm{s}^{-1}$)	100	1

conventional source [7]. Electrons are accelerated to 240 MeV (140 MeV for BEPC) and strike a 10 mm diameter, 8 mm thick copper-plated, disc-shaped tungsten target. The target can be moved in and out of the beam line easily with the help of an actuation system. The positrons generated by pair-production will have a large divergence angle which needs to be focused to a reasonable size ready to be used in the later accelerating section. In BEPC-II, there is a flux concentrator providing a longitudinal magnetic field for this job. The flux concentrator is a device that has a 12-turn 10 mm long copper coil with a cylindrical outside radius of 53 mm and a conical inside radius growing from 3.5 mm to 26 mm. This device helps to match the phase space distribution of the positron beam from the target to the linac as explained in Chapter 2. The new BEPC-II positron source has been designed and fabricated since 2002, and has been shown to be a successful design.

1.2.3 The Large Electron-Positron Collider, LEP

The Large Electron-Positron collider (LEP) is the largest electron-positron collider that has been built [8]. LEP was located in CERN, Geneva. The main ring tunnel (now occupied by LHC) has a circumference of 26.67 km. Operation began in the summer of 1989 with a collision energy of 91.2 GeV. Regarding the positron source of LEP, it used the classic design of a conventional positron source. There are several small subsections playing roles as injectors or boosters, such as LIL and EPA. LIL was the LEP Injector Linac, that accelerated electrons to 200 MeV. The high energy electron beam struck a tungsten target to produce the positrons; the remaining electrons, along with the positrons, were then passed into the Electron Positron Accumulator ring (EPA), where they were stored and accumulated before injection. The conventional positron source

achieved its target to produce sufficiently intense positron beams for LEP to reach its luminosity goals. The main purpose of LEP was for precision studies of both the Z and W bosons and for the search for new particles. In order to achieve the goal, the energy and luminosity of the machine were key parameters. From 1994 to 2000, by the hard work of many scientists, the energy and luminosity of LEP was improved significantly. In 1999, LEP reached its peak luminosity of just over $10^{32}\,\mathrm{cm}^{-2}\mathrm{s}^{-1}$ [9], with an average daily integrated luminosity of close to $1.4\,\mathrm{pb}^{-1}$. In 2000 the beam energy achieved a record high of 104.3 GeV. However, the luminosity was lower than the value of 1999 as a trade-off with the energy. The reduction is mainly due to the lower beam currents, shorter fills and larger horizontal beam sizes.

1.2.4 The SLAC Linear Collider, SLC

The Stanford Linear Collider (SLC) began construction in 1983 and was completed in 1989. Initially, the SLC was constructed as a prototype to demonstrate the feasibility of a high energy electron-positron linear collider. The SLC was the world's first and only linear collider [10]. A schematic of the facility is shown in Fig. 1.3. SLC accelerated electrons and positrons to about 50 GeV using the same, two-mile long linac. In each machine pulse, the source generated two bunches of polarised electrons. The first one was used for collision, and the second one was used to generate a positron bunch. The electron and positron bunches were first injected into damping rings, to reduce the bunch dimensions to sizes suitable for generating luminosity. When the electron and positron bunches were extracted from the damping rings, they were then injected into the linac, which accelerated the particles to 46.6 GeV. At the end of the linac, the electron and positron bunches were separated into two long curving arcs. In the arcs, the particles lost about 1 GeV energy, because of synchrotron radiation. The electron and positron bunches then collided head-on at the interaction point (IP) with a centre-of-mass energy of 91.2 GeV. The bunches were dumped after collision.

At the interaction point, SLC needed 3×10^{10} to 7×10^{10} positrons per bunch, with a repetition rate of 120 Hz. There was only one bunch per machine pulse, therefore the total number of positrons needed per second was only about 8.4×10^{12} positrons per second. For comparison, ILC will need about 2.7×10^{14} positrons per second, more than 30 times as many. In order to produce sufficient positrons for collision, SLC used a conventional positron source. A bunch of electrons with energy 33 GeV was incident on

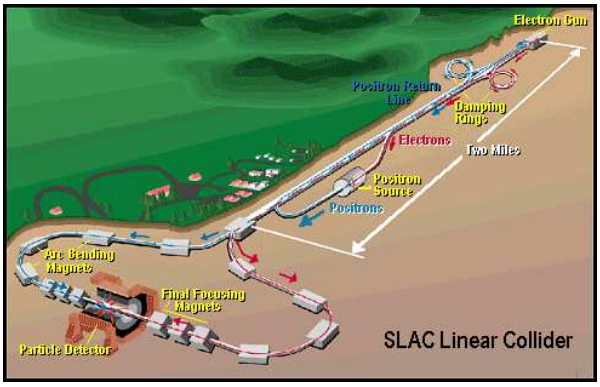

Figure 1.3: Schematic view of the SLAC Linear Collider.

a thick, high-Z material target to generate positrons by cascade shower. Due to the large divergence angle of the positrons coming from the target, a flux concentrator was used, which helped to improve the capture efficiency, and so increased the overall positron yield. The SLC positron source has been discussed in detail in references [11] and [12]. As the first and only linear collider in the world, SLC provided essential experience for the design of a next generation electron-positron linear collider. Future linear collider projects presently under study will be introduced in the following sections.

1.3 From Circular to Linear Colliders

From 1999 to 2000, LEP was upgraded to increase the energy. Although there was a significant drop in luminosity, the increase in beam energy was relatively small. One of the reasons for this was synchrotron radiation. The 100 GeV particles stored in LEP radiated 3% of their total energy per turn. The amount of energy radiated by particles in a storage ring is proportional to the fourth power of beam energy and inversely proportional to the square of the bending radius. So LEP is still the largest circular electron-positron collider ever built, because the synchrotron radiation means that to accelerate electrons and positrons to higher energies, a bigger (and more expensive) circular collider would be needed. However, the synchrotron radiation power is also inversely proportional to the fourth power of the mass of the particle: therefore, the highest energy circular colliders (such as Tevatron and LHC) are hadron machines. But because hadrons interact through the strong nuclear force as well as the electromag-

netic and weak nuclear forces, detector backgrounds are much higher in proton-proton colliders than in electron-positron colliders. For precision measurements using electron-positron collisions, a linear collider is the best answer [13][14]. There are two future linear colliders that have been proposed: these are the International Linear Collider (ILC), and the Compact Linear Collider (CLIC), which we will introduce in later sections.

In 2010, one of the most exciting events in scientific research will be operation of the Large Hadron Collider (LHC) in CERN, Geneva. The advantage of LHC is its high collision energy of 7 TeV protons, but as already mentioned, the detector backgrounds in LHC will be much higher than in an electron-positron collider, because of the strong interactions of the hadrons, and their sub-structure. Hence, in general, LHC will be a discovery machine for new physical phenomena, but not sufficient for precision measurements and research. Therefore, a precision machine is needed that can be complementary to the LHC.

An electron-positron collider will be ideal, because the particles have no sub-structure, and interact only through the electromagnetic and weak interactions. However, if we want to accelerate electrons or positrons to energies of the order of 1 TeV in a storage ring, there will be significant power losses because of synchrotron radiation. When charged particles circulate in storage rings, they lose energy at a rate proportional to the fourth power of the beam energy, and inversely proportional to the square of the radius of the trajectory:

$$P_s = \frac{e^2 c}{6\pi\varepsilon_0}\frac{1}{(m_0c^2)^4}\frac{E^4}{R^2}, \tag{1.1}$$

where P_s is the radiated power during transverse acceleration, E is the energy of the particle, e the charge on the particle, m_0 the rest mass of the particle, R is the bending radius of the particle orbit, c is the speed of light, and ε_0 is the permittivity of free space.

For particles of a given energy and charge, the radiated power varies inversely with the fourth power of the rest mass. Comparing the power radiation from an electron (m_ec^2=0.511 MeV) with that from a proton of the same energy (m_pc^2=938.19 MeV) gives:

$$\frac{P_{s,e}}{P_{s,p}} = \left(\frac{m_pc^2}{m_ec^2}\right)^4 \approx 1.13 \times 10^{13}. \tag{1.2}$$

The radiation power at a given energy and a given bending radius is thirteen orders

of magnitude larger for electron than for protons: thus a proton-proton machine such as the LHC which is circular with TeV energy is practicable, but a circular electron-positron machine operating at similar energy is not. In order to avoid the loss of large amounts of energy by synchrotron radiation that happens when high energy electrons or positrons follow a circular trajectory, the next generation electron-positron collider must be linear. However, to keep costs realistic, the size of the linear collider needs to be kept reasonable. In general, the accelerating gradient of superconducting RF cavities has a fundamental limit at about 60 MV/m. With normal conducting RF structures, higher gradients are achievable, but the technology is not trivial and still under development. A linear collider will need high gradient RF cavities, since the beam needs to be accelerated to high energy in a limited distance. There are two linear colliders, based on different technologies, that have been proposed and are being developed in parallel. The ILC will use superconducting technology to accelerate the electron and positron beams to 250 GeV, to achieve collisions at centre-of-mass energy of 500 GeV. CLIC is based on two beam acceleration to reach centre-of-mass energy of 3 TeV. In later sections, further details about these two machines will be introduced.

1.4 Positron Sources for Linear Colliders

From the history we have introduced, we can see that positrons have been used in important applications in accelerator science for 50 years. In order to produce sufficiently intense positron beams, there are several schemes of positron production that have been proposed and studied [15]. The conventional scheme, based on impacting high-energy electrons on a target, leading to bremsstrahlung and pair production, has been implemented many times in different accelerators. However, other schemes are still in the development stage, and have a number of challenges to overcome. As developments in accelerator science lead to higher luminosity goals (driven by the demands in high energy physics), a good positron source design will be very important. In the following sub-sections, we will briefly introduce some positron source designs which either have been already implemented or are still undergoing development.

1.4.1 Conventional Source

A conventional positron source is based on the use of high energy electrons striking a high Z material target to generate electromagnetic cascade showers (thick target) or pairs of electron and positrons (thin target) [16]. In general, the electron beam will have an energy of a few GeV; when the electrons impinge onto the target, the electrons will lose energy by radiation and collision with the atoms. In this process, the energy lost through radiation (bremsstrahlung) is distributed among photons which interact with the Coulomb fields of the nuclei in the target material, resulting in production of electron-positron pairs. These processes continue in turn, until the remaining particles have energy too low for further pair production. Electrons and photons then lose energy via scattering until they are eventually absorbed by atoms. The energy lost by collision is deposited in the target as heat. The energy deposition and heating is a major concern in the use of conventional positron sources. Another concern is the emittance of the positron beam since in the process of propagation through the material of the target, there will be multiple scattering, resulting in a large angular distribution for the positrons. There are several designs that have been used in previous accelerators, such as classical thick amorphous disk targets. In order to limit the transverse size increase caused by multiple scattering, and also to allow the low energy positrons to leave the target instead of being absorbed, a design based on a wire target has been proposed. Another popular idea is to use separate targets for photon production and electron-positron pair production. Basically, there are two targets: the first one will be used as a radiator to produce the photons and the other target will be used as a converter for the materialization of the photons into electron and positron pairs. The advantage of using separate targets is that it is possible to avoid excessive thermal heating using a crystal in channelling conditions to deliver an intense photon beam to a thin converter.

The conventional positron source is a classic design that has been used in many accelerators. The advantages of this design are that:

1. it is a mature and reliable, proven concept;
2. it operates independently of the main electron source;
3. high rates of positron production can be achieved.

However, at the same time this scheme also has some limitations that need to be considered:

1. multiple scattering will affect the positron angular distribution which leads to a large emittance;

2. high energy electrons and ionization in the target cause energy deposition and heating problems;

3. it is very difficult to produce polarised positron beams.

1.4.2 Undulator-Based Positron Source

The idea behind an undulator-based positron source is that instead of letting high energy electron beams strike a target directly, the main electron beam first goes through a helical undulator [17] to produce high energy, high intensity photons, which are then used to strike a thin target. By pair production, electron and positron pairs will be created. One of the advantages of using an undulator is that it is possible to avoid using a thick target in an intense electron beam. Even better, using a helical undulator could provide circularly polarised photons to produce polarised positrons in a thin target. In this system, the key component is the undulator, which could be made of two superconducting wires wound around each other like a double helix in DNA. The current flow in one wire is in the opposite direction to the current flow in the other wire. The longitudinal field is cancelled on the axis, and the resultant field from the two conductors is a transverse field that rotates as a function of distance along the axis. The rotating magnetic field will lead to the electron beam following a helical trajectory. The electron orbital period will be the same as the undulator period. The motion will generate synchrotron radiation, with the electrons emitting a stream of photons into a conical angle of $\frac{1}{\gamma}$ (where γ is the relativistic factor of the electrons) around the instantaneous electron direction of motion. The emitted photon beam is incident on an alloy target wheel which has a thickness of about 0.4 radiation lengths. By pair production, positrons will be generated and will escape from the target. The positrons will be focused by a matching device (see Section 2.4) that provides a magnetic field to control the motion of the positrons; finally, the positron beam is captured and accelerated by a section of linear accelerator.

The undulator-based positron source is the baseline design for the International Linear Collider. The advantages of an undulator-based positron source are that:

1. a prototype has been built and tested;
2. it is possible to produce a sufficiently intense positron beam;
3. a helical undulator can be used to generate polarised positrons;
4. a thin target can be used, which results in lower energy deposition compared with a conventional source.

As always, this scheme is not perfect, there are disadvantages as well:

1. the source is dependent on the electron beam, which complicates the timing scheme of a linear collider;
2. large amounts of specialised infrastructure are needed, which limits the application;
3. the main electron beam will gain additional energy spread as it passes through the undulator;
4. if collision energies are needed that are below the energy at which the electron beam must pass through the undulator, then the electron beam must be decelerated before collision.

1.4.3 Compton Source

The Compton scheme is designed to produce polarised positrons from polarised gamma rays created by Compton scattering [18]. Regarding Compton scattering, a high energy (few GeV) electron beam collides with a laser: in this process, photons from the laser gain energy and their wavelengths decrease. And then, as in the undulator scheme, the beam of gamma rays will strike the thin target to produce positrons. In the whole process, the electron and (laser) photon interaction is one of the most important steps, and is mainly governed by two factors: the density and energy of the laser photons. The electron beam is stored in a storage ring, while the (laser) photon beam is stored in an optical cavity. The numbers of electrons and photons are high but the interaction time between electrons and photons is short; hence, the total number of gamma rays

produced is very small, which means that the number of positrons generated will be very small. The solution is that for this scheme, the positrons are produced slowly and must be accumulated in a damping ring, which is one of the biggest challenges. However, a lot of scientists worldwide are working on this scheme, trying to solve existing problems such as:

1. production of high-intensity laser beam;
2. achieving the necessary collision efficiency and duration;
3. re-use of electron and photon beams;
4. design of a damping ring with sufficient acceptance to allow injection of newly-produced positrons without loss of stored positrons.

But it is worth tackling the challenges, since the mature Compton scheme will be very beneficial for several reasons:

1. it will be possible to generate polarised positrons;
2. the system is completely independent of the main electron beam;
3. a relatively low energy electron beam is required;
4. the scheme could be used in a wide range of potential applications.

1.4.4 Other Positron Source Schemes

Other than those mentioned above, there are different types of positron source based mainly on the conventional target scheme. For example, an enhancement of bremsstrahlung radiation can be achieved using a crystalline target [19] at an appropriate orientation: when the incident electron penetrates the crystal at glancing incidence to the planes, the electron becomes trapped in the potential. The radiation becomes much more intense than usual. So the channelled electrons could be a powerful source of photons. Furthermore, there are also designs that propose to use different targets instead of solid thin or thick ones. Liquid or powder targets have been proposed, since by using such targets, problems with energy deposition can be avoided. But all these proposals are still in the development stage, and although they have certain advantages, they also have at the same time, certain disadvantages. It is possible that more variants on the

positron sources described above will appear in the near future, with applications to particular projects that will maximise particular advantages.

1.5 Linear Collider Projects and Their Positron Sources

The International Linear Collider (ILC) is a proposed high energy electron-positron linear collider with a baseline centre-of-mass energy of 500 GeV, supporting a later upgrade to 1 TeV, and a baseline luminosity of $2 \times 10^{34}\,\mathrm{cm}^{-2}\mathrm{s}^{-1}$ [20]. The ILC is important for future precision physics measurements, complementary to experiments at LHC. It will allow the acceleration of electrons and positrons, which have no observed sub-structure and no interaction through the strong nuclear force; so it will be easier to analyse accurately the collision data at ILC than at the LHC, which is more of a discovery machine and will (we hope) find the Higgs bosons if it exists. Another feature of the proposed ILC is the use of polarised beams. This is important because polarised electron and positron beams lead to a much higher precision for probing the properties of new particles. Furthermore, suitable combinations of the electron and positron polarisation can be used to enhance signal rates of interesting processes and suppress unwanted background. Hence an increase in the ratio of signal/background combined with high luminosity will allow promising future research.

The Compact Linear Collider (CLIC) is an advanced future electron-positron collider to exploit the LHC's discoveries in a new high energy frontier, which is beyond the capabilities of today's accelerators [21]. CLIC is an electron-positron machine aiming to operate at a centre-of-mass energy range from 0.5 TeV to 3 TeV. Both ILC and CLIC are electron-positron linear colliders designed for precision physics measurements. Although the two machines are based on very different acceleration technologies, there are sufficient similarities that it is worth considering whether some of the features of the more mature ILC design can be adapted and re-optimised for use in CLIC.

For their operation, both ILC and CLIC need of order 10^{14} positrons per second to fulfil the luminosity requirements; for some of the proposed studies, the positron beam will need to be polarised. The required rate of positron production is a factor $\sim$60 greater than any previous positron source, such as the SLC at SLAC. In the remaining sections of the present chapter, we will present a general introduction to ILC and CLIC, focusing on their positron sources. In the following chapters, we will go through

the ILC undulator-based scheme to discuss the key components, such as the helical undulator, photon collimator, target, and matching device. After the ILC chapter, we will consider the possibility of implementing an undulator-based positron source for CLIC. The optimisation in different scenarios of operating energy and upgrade options will be discussed. Finally, there will be a conclusion about the possibility of using an undulator-based positron source in CLIC, and its advantages and weaknesses compared to the present baseline scheme.

1.5.1 International Linear Collider

The ILC is a high-energy collider designed for precision studies of the Higgs boson and other phenomena yet to be observed, such as super-symmetry. Fig. 1.4 depicts schematically the layout of the ILC baseline configuration [20]. The ILC is approximately 31 km long. Electrons and positrons will be collided at centre-of-mass energies of 500 GeV (with the possibility to upgrade to 1 TeV). Electrons and positrons are accelerated in separate linacs. At the interaction point, particle bunches containing of order 10^{10} particles are focused to a width of 650 nm and a height of 5 nm, and collide at a rate of 14,000 times per second. The global parameters of the ILC are given in Table 1.3.

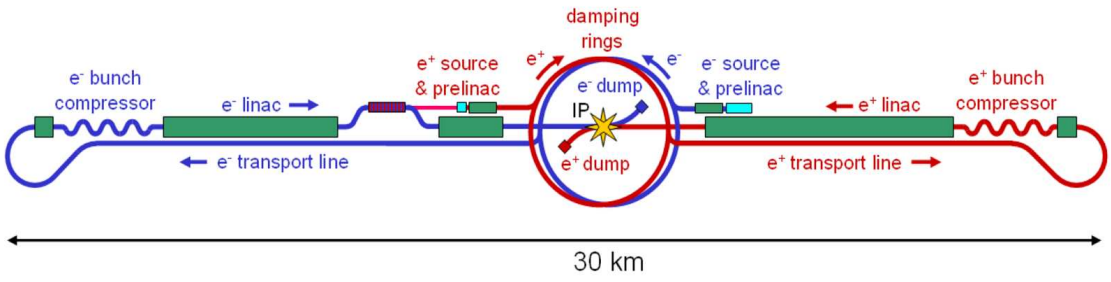

Figure 1.4: Schematic view of the International Linear Collider baseline configuration.

The ILC linacs use superconducting RF cavities at 1.3 GHz frequency, and average accelerating gradient of 31.5 MV/m. There are several advantages of using superconducting technology. First, the power transfer is high efficiency, because the low surface resistance leads to low power losses. The greatest benefit of the low surface losses is realised if the cavities work as standing wave structures: however, this leads to a long

Table 1.3: Global accelerator paramters for ILC.

Centre-of-mass energy	500 GeV
Peak luminosity	$2 \times 10^{34}\,\mathrm{cm}^{-2}\mathrm{s}^{-1}$
Repetition rate	5 Hz
Linac cavity gradient	31.5 MV/m
Beam pulse length	1.0 ms
Beam current in pulse	9.0 mA
Beam size at IP	640 nm×5.7 nm

fill time, which can itself reduce the power efficiency. To maintain efficient operation, the RF pulse length should be long compared to the fill time: in ILC, the beam pulse has a total length of 1 ms. The long fill time also limits the average beam current. If the beam current is too high, then the beam will draw energy from the cavities more quickly than it can be replaced. In ILC, the average beam current is 9 mA. The ILC parameters have been chosen to maximise operational performance while minimising construction and operating costs. However, the RF parameters are still ambitious for a machine on the scale of ILC. There are several test facilities all over the world, including at Fermilab in the USA and at KEK in Japan. There has been a significant improvement in the technology over the past few years, but there are still challenges to achieve the desired results. In particular, it is difficult to produce on a large scale cavities that can reliably achieve the accelerating gradient required in ILC. Reducing the gradient specification would mean that a longer linac would be required for the same collision energy, and this would increase the cost of the machine.

The electron beam is generated from a DC photocathode gun. Each pulse is 1 ms long, consisting of 2625 bunches of 10^{10} electrons per bunch, and minimum 80% polarization. Pulses are generated at 5 Hz. The electron beam is delivered to a normal conducting (NC) accelerating section to increase the beam energy to 76 MeV. Immediately downstream of the NC pre-accelerator, a vertical chicane provides energy collimation before particle bunches are injected into the superconducting booster linac. The booster consists of 21 'ILC standard' superconducting (SC) RF cryomodules that accelerate the beam to 5 GeV. Typical FODO cells integrated into the cryomodules provide transverse focusing for the beam. After the booster, the Linac-to-Ring (LTR) beam line transports the beam to the electron damping ring, performing spin rotation

and energy compression on the way. The LTR will bend the 5 GeV polarized electron beam through an arc. If the first bend of the LTR is turned off, the 5 GeV beam is sent to a beam dump which can be used for machine protection or for tuning.

Following the LTR is a Damping Ring with a circumference of 6.7 km. The Damping Ring performs several critical functions, principally accepting electron and positron beams with large transverse and longitudinal emittances and producing the low-emittance beams required for luminosity production. Furthermore, it damps incoming beam jitter to provide stable beams for later use. After being ejected from the Damping Ring, the bunch train will go through the Ring-to-Main Linac (RTML) beam line. The electron beam will be accelerated to 15.0 GeV before injection into the main linac. Also short bunches are required for collision, so the RTML will compress the beam from 9 mm in the Damping Ring bunch length to 0.3 mm, required at the Interaction Point (IP) to minimise the hour-glass effect. At the same time, the RTML can collimate any beam halo generated in the Damping Ring and rotate the spin polarisation vector from the vertical to any arbitrary angle required at the IP. In the 11 km linac, the electron beam is accelerated to a final energy of 250 GeV.

The luminosity of a linear collider is given by:

$$L = \frac{n_b N^2 f_{rep}}{4\pi\sigma_x\sigma_y} \cdot H_D, \tag{1.3}$$

where n_b is the number of bunches in a bunch train, N is the number of particles in a single bunch, f_{rep} is the machine pulse repetition rate, σ_x and σ_y are the horizontal and vertical beam sizes at the IP, and H_D is the 'enhancement factor' ($\sim$1.5) that accounts for the mutual focusing effects of the colliding bunches. The number of bunches, particles per bunch, and pulse repetition frequency are all limited by the RF technology in the linacs. Therefore, to maximise the luminosity, the transverse beam sizes must be made as small as possible. To meet the luminosity goal, the Beam Delivery System (BDS) focuses the beam to a spot size of 640 nm horizontally and 5 nm vertically at the interaction point. The BDS also protects the beam line and detectors, minimises background in the detectors by collimating the large amplitude particles, and measures and monitors the beam before and after collisions. Finally, after collision each beam will go through an extraction line to a beam dump.

The ILC baseline configuration specifies an 'undulator-based' positron source. The electron beam at an energy of order 100 GeV goes through a long helical undulator to

emit multi-MeV photons. The generated gamma rays will be collimated by a photon collimator which can help to protect the target station and improve polarisation. The collimated photons will then be converted to electron-positron pairs in a target. Fig. 1.5 shows the major elements of the positron source [22].

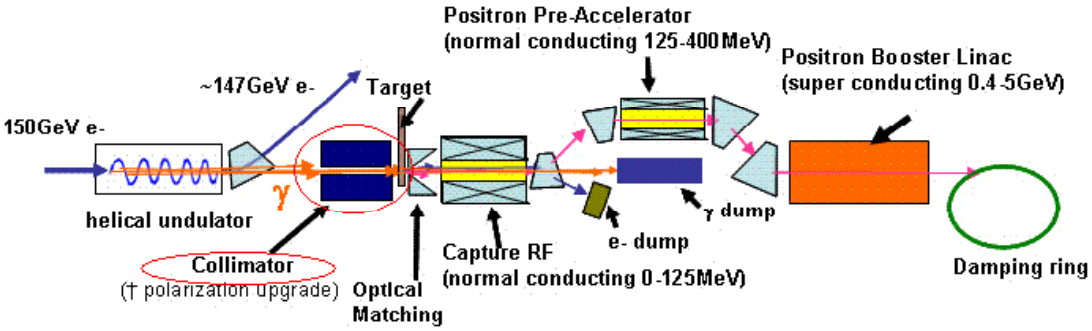

Figure 1.5: Schematic view of the ILC undulator-based positron source.

Longitudinally polarised positron beams can be produced from a beam of circularly polarised photons, which are themselves produced by passing the main high-energy electron beam through a helical undulator. A helical undulator is a device that has a 'rotating' magnetic field (as a function of distance along the undulator) in which electrons will move in a spiral trajectory. The motion of the electrons in the magnetic field of the undulator causes them to emit a stream of photons. Circularly polarised photons are used to generate longitudinally polarised positrons in a conversion target. The principle of the device is shown in the Fig.1.6 [23].

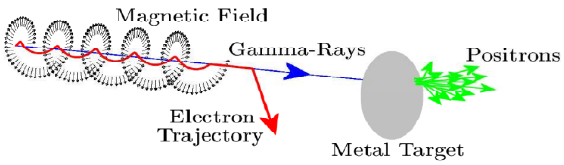

Figure 1.6: Principle of polarised positron production from high-energy electrons in a helical undulator.

A simple way to generate the required magnetic field is to use two conductors wound in a double helix with opposite current, as shown in Fig. 1.7 [22]. The longitudinal field is cancelled on the axis, and the resultant field from the two conductors is a transverse field that rotates as a function of distance along the axis. A proof of principle

experiment (E166, performed at SLAC [24]) has demonstrated the successful production of polarised positrons using this technique. A prototype for a helical undulator for the ILC undulator-based positron source is shown in Fig. 1.7.

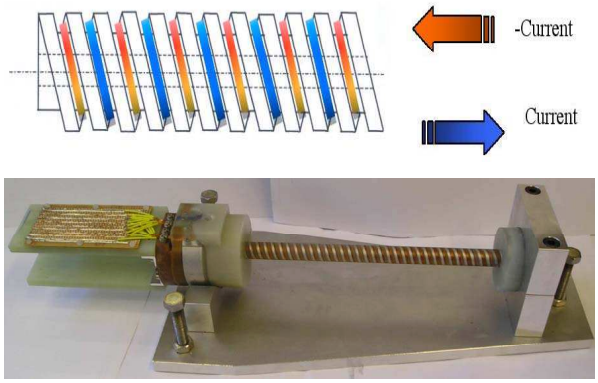

Figure 1.7: Top: Double helix winding with opposite currents generate a rotating magnetic field as a function of longitudinal distance along the undulator axis. Bottom: Prototype of a helical undulator for the ILC positron source.

In the ILC, it is planned to use superconducting undulator technology to achieve a high field with a short period. Because a helical undulator provides a more efficient way of generating photons than a planar undulator, the overall length can be shorter for the same quantity of photons. One additional advantage of the undulator-based source is that the heat load on the target is less than that of the conventional source, so it is suitable for production of high intensity beams. The parameters of the baseline ILC helical undulator are shown in Table 1.4.

At the end of the undulator, electrons will be injected back into the electron linac ultimately to collide with positrons at the interaction point. The photon beam will be collimated by a photon collimator before the beam strikes a rotating target. The photon collimator is a cylindrical device consisting of an inner spoiler and an outer absorber. There are two purposes for the photon collimator [25]: the first is to scrape the photon beam to limit the extraneous halo, and the second is to adjust the polarisation. The photon beam has the highest polarisation in the centre of the beam. The further the photon is from the axis, the lower the polarisation. Hence we need to use a collimator as a filter to remove photons far from the axis if we want to achieve 60% positron polarisation. However, removing positrons to improve polarisation also re-

Table 1.4: Undulator parameters for ILC.

Undulator period	11.5 mm
Deflection parameter	0.92
Undulator type	Helical
Undulator length	200 m
Field on-axis	0.86 T
Beam aperture	5.85 mm
Electron beam energy	150 GeV
Electron current	9.0 mA
Photon energy(1^{st} harmonic cutoff)	10.06 MeV
Photon beam power	131 kW

duces the beam intensity. So we cannot just use the first harmonic of the photon beam, which has the highest polarisation. All in all, there must be some compromise between polarisation and quantity of positrons. The photon collimator provides the means to adjust the balance between polarisation and beam intensity. There are different design concepts for the photon collimator already proposed by DESY and Cornell. In the next chapter we will discuss further the photon collimator, including various geometries and performance simulations.

After collimation, the photons hit a thin target producing an electromagnetic shower to generate electron and positron pairs. The target will be discussed in more detail in the following chapters. The distance from the centre of the undulator to the target is about 500 meters. The photon beam has a transverse size of ∼1 mm rms and deposits ∼10.5 kW of power in the target. There are up to 8 harmonics contributing to the positron generation. The target consists of an annular rim of titanium alloy (Ti-6% Al-4% V) supported by five equally-spaced struts. The diameter of the wheel is 1 m and the thickness is 0.4 radiation lengths. The most severe engineering challenge is to cope with the energy deposition from the shower. Therefore, in the ILC a rotating target is used to relax the thermal loading problem. The rim spins at 100 m per second. Since the repetition rate of the ILC is 5 Hz, successive bunch trains can be separated on the target. The relatively low repetition rate provides time for the target to cool down between successive pulses, but the target also contains an internal water-cooling channel, which removes heat from the rim. In addition, the size of the wheel (1 m

diameter) offsets radiation damage.

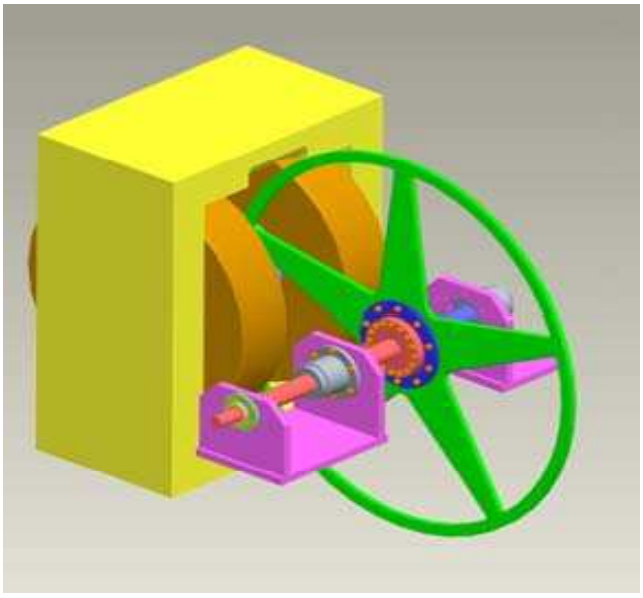

Figure 1.8: Design for the rotating target for the ILC positron source.

The energies of particles coming out of the target are in the range 3–55 MeV. The target is followed by an Optical Matching Device (OMD) which is used to match the beam phase space from the target into the capture L-band RF. The capture RF raises the beam energy to 125 MeV; RF cavities are located inside 0.5 T solenoids that focus the beam. Because the target and associated equipment become highly activated during operation, there is a remote-handling system to replace the target in the case of target failure. Following the capture section, the positron beam will be accelerated from 125 MeV to 400 MeV in a normal-conduction L-Band RF, again embedded in a solenoid field of 0.5 T. From this point, the positron beam will pass through systems identical to those used for the electron beam, including the LTR, the Damping Ring, the RTML, the main linac and the BDS.

1.5.2 Compact Linear Collider

ILC will provide centre-of-mass collision energy of 500 GeV with a possible future upgrade to 1 TeV. The RF systems for accelerating the beams in the main linacs are based on superconducting cavities. These provide efficient power transfer to the beam using technology that today is close to achieving the specified performance. However, the

accelerating gradient that can be achieved using a superconducting cavity is limited by the fact that the strong magnetic fields generated inside the cavities will quench the superconducting material if the gradient gets too high. A higher energy can be achieved by using longer linacs, but this will increase the cost of the machine. Therefore, an alternative accelerating technology is required to achieve centre-of-mass collision energies of more than 1 TeV.

CLIC has been proposed as a linear collider capable of achieving centre-of-mass collision energies of 3 TeV, with linacs kept to a realistic length by operating with an accelerating gradient in the cavities of 100 MV/m. The luminosity will be at least $10^{34}\text{cm}^{-2}\text{s}^{-1}$, to allow precision studies of the Higgs boson and other new physics phenomena. A conventional linac design uses klystrons to produce pulsed RF power to accelerate beam; however, CLIC would require tens of thousands of klystrons along the entire accelerating section. CLIC in that case would be extremely long and expensive. Instead of the conventional design, therefore, an innovative design has been proposed for CLIC, which is the "two-beam acceleration" method [26]. The main linac RF power will be extracted from a secondary, parallel, low-energy and high-intensity electron beam line. The bunch frequency structure in the secondary beam line allows the production of RF power at the desired frequency by decelerating the beam through "power extraction and transfer" structures (PETS). By this method, electron and positron beams will be accelerated to energies at the TeV scale within a relatively short distance. As shown in Fig. 1.9, the electron and positron beams will be generated from the injector sections and go through pre-damping rings and damping rings to minimise the emittance. Bunch compressors will reduce the bunch length and inject the beams into booster linacs to accelerate the beams to 6.14 GeV. After second bunch compressors, electron and positron beams will be injected into the main linacs which are 21 km long, and operate at 12 GHz frequency and 100 MV/m accelerating gradient. After the main linacs, the full-energy beams pass through the 2.75 km beam delivery systems to collide at the interaction point. Overall, CLIC will cover a total length of approximately 48 km. For such a huge machine, the positron source is a major challenge, since in order to achieve the specified luminosity, CLIC will need of order 10^{14} positrons per second; for some of the proposed studies, the positron beam will need to be polarised. The required rate of positron production is a factor ∼60 greater than any previous source, such as the SLC at SLAC. So far, three schemes have been considered for the positron source:

a conventional source, a source based on Compton back-scattering, and an undulator scheme. Some characteristics that must be taken into consideration for the choice of the source include the achievable production rate and polarisation. In later sections, the undulator scheme will be considered in detail, as an option for the CLIC positron source.

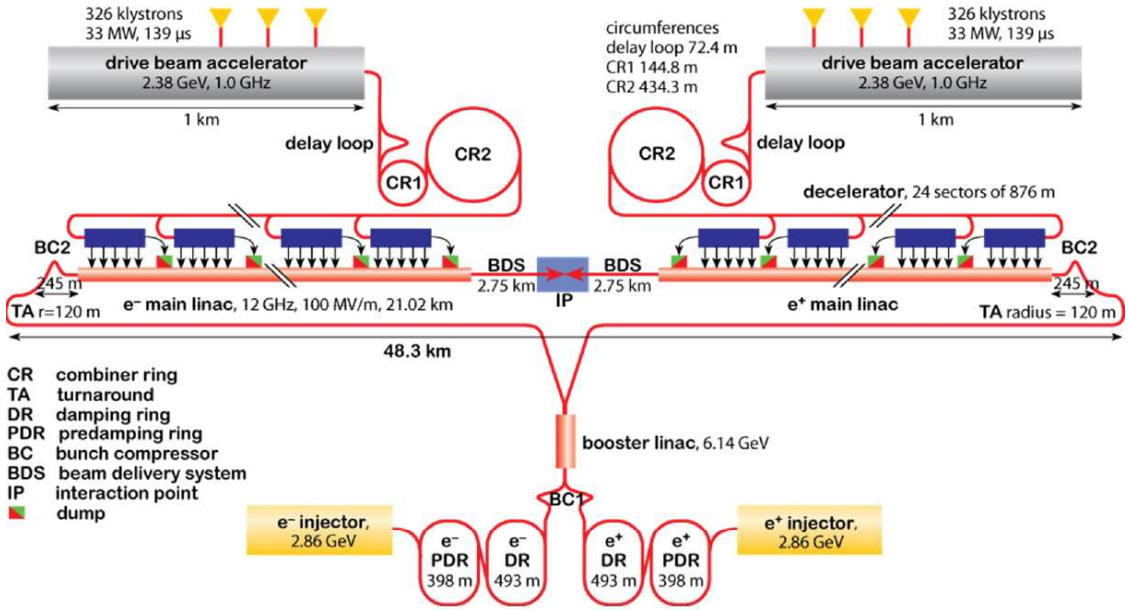

Figure 1.9: Schematic view of the Compact Linear Collider (CLIC).

Table 1.5 shows some of the main parameters of ILC and two operational stages of CLIC. Although the machines have a number of things in common, the different RF technology used to accelerate the beam in CLIC compared to ILC makes each machine unique. ILC uses a long RF pulse, with relatively low average beam current in the linacs. CLIC uses a short pulse with high current. By focusing the beams more strongly at the IP, CLIC achieves a similar luminosity to ILC with a smaller number of particles. ILC will require 2.7×10^{14} positrons per second, while CLIC will require 1.2×10^{14} (stage 1, 0.5 TeV c.o.m.) or 0.58×10^{14} (stage 2, 3 TeV c.o.m.). Although CLIC requires a lower positron production rate than ILC, the shorter pulse and higher repetition rate means that the positron source will not necessarily be any easier.

One of the main issues for the CLIC positron source, in common with ILC, is the power deposition in the target. The luminosity goals in both machines drive the need

Table 1.5: ILC and CLIC main parameters.

	ILC	CLIC stage 1	CLIC stage 2
Centre-of-mass energy (TeV)	0.5	0.5	3.0
Total luminosity ($10^{34}\,\mathrm{cm}^{-2}\mathrm{s}^{-1}$)	2.0	2.3	5.9
Accelerating gradient (MV/m)	31.5	80	100
Total site length (km)	31	13.0	48.3
Total power consuption (MW)	216	130	415
Horizontal/vertical IP beam size (nm)	640/5.7	202/2.3	40/1.0
Repetition rate (Hz)	5	50	50
Bunch charge (10^9)	20	6.8	3.72
Bunch separation (ns)	369	0.5	0.5
Beam pulse duration (μs)	1000	0.177	0.156
Positron production rate (10^{14}/s)	2.7	1.2	0.58

for large numbers of positrons. This puts stress in particular on the conversion target, and design options need to be studied carefully, to make sure that the target can survive both the peak and the average power deposition.

The baseline option for the CLIC positron source is the Compton scheme. Although this design should be able to produce enough positrons, it is still a new scheme that needs a lot of research. Other designs that have been proposed include a modified conventional design using a hybrid target, and an undulator-based scheme similar to ILC. Each option has its own advantages and disadvantages [27], which we will now consider briefly.

The conventional source using a hybrid target, shown in Fig. 1.10, is a possible choice for an unpolarised positron source [19]. Unlike a normal conventional source, which in general uses high energy electrons striking a thick target to create electromagnetic showers, a hybrid target scheme will have two targets. A 5 GeV primary electron beam will strike the first thin (1.4 mm thickness) tungsten crystal target to create photons. Before the particles generated from the crystal reach the second target, which is 3 m away, electrons and positrons will be dumped leaving only high energy photons in the beam. These photons will strike the second 10 mm thick tungsten amorphous target to generate further electron and positron pairs. The positrons will be collected and

accelerated. There are several disadvantages in this design. Although this type of positron source is relatively simple, low cost and independent from the electron source, there is no polarisation at all, and the thermal load on target is difficult to handle.

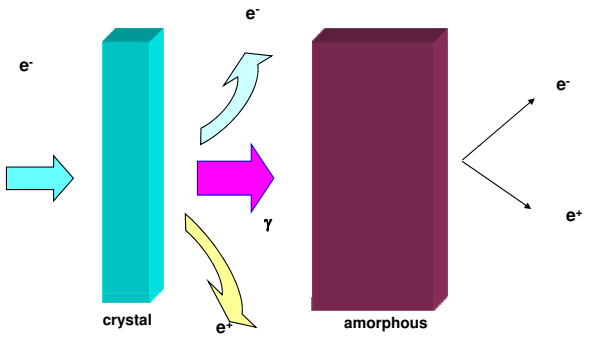

Figure 1.10: Schematic view of the hybrid target positron source.

Another more advanced proposal is the Compton source [18]. A laser beam collides with a high energy electron beam, from which the laser photons will gain energy. The back-scattered photon beam (now with short wavelength and higher energy) will strike a target to produce electron and positron pairs. This technology is not sufficiently mature for immediate implementation, although there is much research activity on its development. The advantages of the Compton source are that it is independent from the electron source, and it has the capability for producing a polarised positron beam.

Finally, there is the undulator-based positron source, which we have already introduced, and will consider in more detail in the following chapters. An undulator-based source for CLIC can be adapted from the ILC, so the layout and the design principles will be similar. However, ILC and CLIC have significant differences in the time structure and the ultimate beam energy; in that case, an optimised undulator-based positron source for CLIC will likely not be exactly the same as for ILC. For example, CLIC is a much higher energy machine, which gives a wider choice for the driving electron beam energy, but at the same time brings more challenges when all factors are considered, in particular the energy deposition. The system needs to be optimised for the CLIC beam properties and parameters. By using an undulator scheme, a polarised positron beam of sufficient intensity can be generated, and the technology is relatively mature (compared to the Compton source). A prototype (E166 experiment at SLAC) has been built and tested, and has proved feasibility of the concept. However, a disadvantage

of an undulator-based positron source is that the source uses the main electron beam as the driving beam, which means that a high energy electron beam is needed before positrons can be produced, and also leads to complications for the timing scheme.

1.6 Thesis Layout

In Chapter 2 the theoretical background on synchrotron radiation is reviewed. The relevant details of undulator radiation regarding the photon spectrum and angular distribution will be discussed. The theoretical results will be compared with simulation results. Also in this chapter, the components of the undulator-based positron source will be described. In addition, the timing issues (related, for example, to the damping rings) will briefly be discussed. This chapter will provide an understanding of the detailed properties of undulator radiation, and how an undulator-based positron source will work.

Chapter 3 will consider the ILC in more detail. The theory of the undulator-based positron source will be applied, using ILC parameters. Most components of the ILC positron source have previously been studied in some detail. However, although some proposals have been made for the ILC photon collimator design, these have not so far been thoroughly considered and compared. Therefore, the photon collimator will be discussed in detail in this chapter. By using realistic distributions for the photons generated by the undulator, the energy deposition and thermal issues for the photon collimator will be investigated. How the collimator affects the photon beam, and the positron production and polarisation, will be explained. The activation and secondary particle generation from the collimator will also be discussed. This chapter will provide a more detailed understanding of the ILC positron source, and of the photon collimator in particular. By comparing two of the proposed designs for the photon collimator, we can identify the right collimator to be used for the ILC baseline.

In Chapter 4, the possibility of using an undulator-based positron source for CLIC will be discussed. A model has been created in Geant4 to simulate the key elements of an undulator-based positron source for CLIC: the goal is to consider such a source as an alternative to the present baseline concept (Compton source). The parameters of the different components need to be adjusted to cover a range of operating scenarios. We report the results of calculations for specific operating scenarios, for the rate of

positron production, positron polarisation, and capture efficiency.

A key issue for the positron source is the energy deposition in the target. In Chapter 5, we will discuss the target wheel experiment which has been carried out at STFC Daresbury Laboratory. We will introduce the mechanical design of the prototype. Positron capture efficiency can be improved if the target is immersed in the magnetic field of the matching device. However, to handle the energy deposition, the target wheel must spin with a rim velocity of 100 m/s, and if this rotation takes place in the magnetic field, then large eddy currents can be induced. The goal of the target wheel experiment at Daresbury is to measure the effects of the eddy currents, and validate the models that predict their effects. In order to understand the eddy currents, we will approach the problem by developing a theoretical model. Since the problem is very complicated, we also run simulations using OPERA. The results from the theoretical models and simulations will be analysed and compared with experimental data.

Finally, a conclusion and plan for the future work will be presented. This thesis presents theory, simulations and experiments in support of undulator-based positron sources for ILC and CLIC. But there is lot work still needed to complete the designs for both machines.

2

Components of an Undulator-Based Positron Source

In this chapter, we introduce each of the main components of an undulator-based positron source. Section 2.1 describes the principles of the helical undulator, and the properties of the radiation that it produces. Section 2.2 introduces the photon collimator, discussing issues such as energy deposition and activation. Section 2.3 describes the pair production target. Finally, Section 2.4 introduces the capture device that is used to match the phase space of the positrons from the target, to the entrance of the first accelerating section seen by the positron beam.

Our aims in this chapter are to outline the physical principles behind each of the components of an undulator-based positron source, and to understand general features and properties. We will give examples based on parameters relevant for ILC and CLIC where such examples are helpful; but detailed discussion of undulator-based positron sources for these machines will be left to later chapters.

2.1 Undulator

The first component in an undulator-based positron source for a linear collider is the undulator itself. The undulator consists of a magnetic field that varies periodically. In a planar undulator, the field remains parallel to a given direction while the strength varies sinusoidally with distance along the undulator. The positron beam produced by a source using a planar undulator will be unpolarised. In a helical undulator,

the strength of the field remains constant, while the direction "rotates" with distance along the undulator [17]. Helical undulators can be used to produce polarised beams of positrons. The degree of polarisation depends not just on the undulator, but also on the components downstream of the undulator.

As high energy (tens of GeV) electrons pass through an undulator, they emit synchrotron radiation. The synchrotron radiation can be collimated (if necessary) before impacting the pair production target. In this section, we focus on the properties of the radiation produced by the undulator, beginning with a general description of synchrotron radiation.

2.1.1 Synchrotron Radiation

Synchrotron radiation is the electromagnetic radiation emitted by relativistic charged particles when they undergo acceleration. Such radiation was first observed from a General Electric synchrotron in 1947 [28]. Synchrotron radiation is produced whenever a relativistic charged particle is bent in a magnetic field, and can cover a range of the electromagnetic spectrum from infrared, through visible light and ultraviolet light to x-rays.

As a consequence of synchrotron radiation, relativistic charged particles in a magnetic field will lose energy. As accelerator technology has developed, the ability to add energy to charged particles has improved. Synchrotron radiation can be a severe limitation for high energy electron accelerators [29]. The power lost through synchrotron radiation varies as:

$$\Delta E \propto \frac{1}{\rho^2 m_0^4}, \tag{2.1}$$

where m_0 is the rest mass of the particle, and ρ is the radius of curvature of the path of the particle in the magnetic field. For a circular machine accelerating electrons, large amounts of energy are radiated and wasted by hitting the beam pipe; this energy needs to be restored to the particles in order to maintain the beam energy. However, with the help of insertion devices such as wigglers and undulators, electron storage rings can be used to produce intense beams of synchrotron radiation that can be used widely in many fields of science, including chemistry and medicine. Since the mass of the proton is much larger than that of the electron, the synchrotron radiation produced by protons is generally negligible.

To understand synchrotron radiation, two key effects are Lorentz contraction and relativistic Doppler shift [30]. For example, consider an electron that travels through an undulator (period λ_u) at (close to) the speed of light. In the moving frame, the period of the undulator will be contracted by a factor of γ, and so the electron will emit the radiation with wavelength $\frac{\lambda_u}{\gamma}$. For the relativistic Doppler shift, in the case of the particle travelling with the speed of light towards the observer, the frequency will change to:

$$f = \gamma f'(1 + \beta), \tag{2.2}$$

where the observer will see radiation at a frequency f, the source (electron) emits radiation at frequency f' in its own rest frame, and $\beta = \frac{v}{c}$ where v is the velocity of the electron. If we convert the frequency of the radiation to the wavelength, we get:

$$\lambda = \frac{\lambda'}{\gamma(1 + \beta)} \approx \frac{\lambda'}{2\gamma}. \tag{2.3}$$

We see that the wavelength of radiation observed in the rest frame of the undulator is $\lambda_u/2\gamma^2$. Modern accelerators readily achieve energies of a few GeV; for electrons, the relativistic factor γ can be a few thousands. For an undulator with a period of order 0.1 m, the synchrotron radiation can have a wavelength of a few nanometres. A further important property of synchrotron radiation, is that the radiation is emitted into a narrow cone of opening angle $1/\gamma$ around the instantaneous direction of motion of the particle. For an undulator, interference effects lead to a further narrowing of the cone by a factor $\sqrt{N}$, where N is the number of periods in the undulator. This means that undulators can be used in high energy accelerators to produce beams of very intense radiation with wavelengths of a few nanometres.

Understanding the properties of undulator radiation is essential for optimising the design of an undulator-based positron source. In the following sections, we will consider the properties of synchrotron radiation from an undulator in more detail. Starting from the motion of a charged particle in a magnetic field, we will use Maxwell's equations to find the fields produced, and we will then derive equations for the power emitted and the polarisation. The power spectrum and angular distribution of the radiation are also important properties that we will derive.

2.1.2 Electric and Magnetic Fields Around a Relativistic Charged Particle

The electromagnetic potentials ϕ and $\vec{A}$ around a charged, point-like particle are given by the Liénard-Wiechert potentials [31]:

$$\phi(t) = \frac{e}{4\pi\epsilon_0}\left[\frac{1}{r(1-\vec{n}\cdot\vec{\beta})}\right]_{\text{ret}}, \tag{2.4}$$

$$\vec{A}(t) = \frac{e}{4\pi\epsilon_0 c}\left[\frac{\vec{\beta}}{r(1-\vec{n}\cdot\vec{\beta})}\right]_{\text{ret}}, \tag{2.5}$$

where e is the charge on the particle, r is the distance from the position of the particle to the observation point, $\vec{n}$ is a unit vector from the position of the particle to the observation point, and $\vec{\beta}$ is the velocity of the particle divided by the speed of light. Note that the quantities inside the brackets $[\cdot]_{\text{ret}}$ must be evaluated at a time t', where:

$$t = t' + \frac{r(t')}{c}, \tag{2.6}$$

in order to find the correct values for the potentials at time t. For a relativistic particle moving directly towards the observer ($\vec{n}\cdot\vec{\beta} \approx 1$), there is an enhancement of the electromagnetic potentials; while the potentials are reduced for a particle moving away from the observer.

The electric and magnetic fields may be obtained from the potentials using the usual relations:

$$\vec{B} = \nabla\times\vec{A}, \tag{2.7}$$

$$\vec{E} = -\nabla\phi - \frac{\partial\vec{A}}{\partial t}. \tag{2.8}$$

For a particle on an arbitrary trajectory, application of the derivatives to Eqs. (2.4) and (2.5) is complicated, because r, $\vec{n}$ and $\vec{\beta}$ are all functions of time; and r and $\vec{n}$ are additionally functions of position (of the observer). However, it is possible to perform the derivatives. The result for the electric field is [17]:

$$\vec{E} = \frac{e}{4\pi\epsilon_0}\left[\frac{(1-\beta^2)(\vec{n}-\vec{\beta})}{r^2(1-\vec{n}\cdot\vec{\beta})^3} + \frac{\vec{n}\times((\vec{n}-\vec{\beta})\times\dot{\vec{\beta}})}{cr(1-\vec{n}\cdot\vec{\beta})^3}\right]_{\text{ret}}, \tag{2.9}$$

and for the magnetic field:

$$\vec{B} = \frac{1}{c}\vec{n}\times\vec{E}. \tag{2.10}$$

Note that the second term on the right hand side of Eq. (2.9) depends on the acceleration of the particle $\dot{\vec{\beta}}$. Also, this term varies with distance from the source as $\sim 1/r$, whereas the first term varies as $\sim r^2$. This means that for an accelerating particle, at a sufficient distance from the particle, the fields are dominated by the second term in Eq. (2.9). The region where this second term does dominate the fields is known as the *far field* or *radiation* region, and is the region we shall be concerned with.

It turns out to be convenient to work with the frequency spectrum of the fields, rather than the fields expressed as functions of time. The frequency spectrum of the electric field is given by the Fourier transform of $\vec{E}(t)$:

$$\tilde{E}(\omega) = \frac{1}{\sqrt{2\pi}} \int_{-\infty}^{\infty} \vec{E}(t) e^{i\omega t}\, dt. \tag{2.11}$$

Working in the radiation region, we can substitute for $\vec{E}(t)$ from Eq. (2.9), and at the same time change the variable of integration from t to t' using Eq. (2.6). This gives:

$$\tilde{E}(\omega) = \frac{e}{4\pi\sqrt{2\pi}\epsilon_0} \int_{-\infty}^{\infty} \frac{\vec{n} \times ((\vec{n} - \vec{\beta}) \times \dot{\vec{\beta}})}{cr(1 - \vec{n} \cdot \vec{\beta})^2} e^{i\omega(t' + \frac{r}{c})}\, dt'. \tag{2.12}$$

Let us assume that the observer is sufficiently far from the particle that $\vec{n}$ is constant: this is consistent with working in the radiation region. Then, we can integrate Eq. (2.12) by parts to give:

$$\tilde{E}(\omega) = \frac{i\omega e}{4\pi\sqrt{2\pi}\epsilon_0 cr} \int_{-\infty}^{\infty} (\vec{n} \times (\vec{n} \times \vec{\beta}))\, e^{i\omega(t' + \frac{r}{c})}\, dt'. \tag{2.13}$$

2.1.3 Electromagnetic Radiation from a Relativistic Charged Particle

The energy flux (energy crossing unit area per unit time) in an electromagnetic field is given by the Poynting vector $\vec{S}$ [32]:

$$\vec{S} = \vec{E} \times \vec{H} = \frac{1}{\mu_0} \vec{E} \times \vec{B}. \tag{2.14}$$

Using Eq. (2.10) this becomes:

$$\vec{S}(t) = \frac{\vec{n}}{\mu_0 c} \left| \vec{E}(t) \right|^2. \tag{2.15}$$

The total energy per unit area crossing the observation point is given by:

$$\int_{-\infty}^{\infty} \left| \vec{S}(t) \right| dt = \frac{1}{\mu_0 c} \int_{-\infty}^{\infty} \left| \vec{E}(t) \right|^2 dt. \tag{2.16}$$

Using Parseval's theorem [33], this becomes:

$$\int_{-\infty}^{\infty} \left|\vec{S}(t)\right| \, dt = \frac{1}{\mu_0 c} \int_{-\infty}^{\infty} \left|\tilde{E}(\omega)\right|^2 \, d\omega. \tag{2.17}$$

From Eq. (2.15), we see that the energy flow is in the direction of $\vec{n}$, the unit vector from the source to the observer. Therefore, using $dA = r^2 \, d\Omega$ (where dA is an area element corresponding to solid angle element $d\Omega$ centred on the particle), we can write the spectral energy distribution (energy crossing unit area per unit frequency) as:

$$\frac{d^2W}{d\omega \, d\Omega} = \frac{2r^2}{\mu_0 c} \left|\tilde{E}(\omega)\right|^2. \tag{2.18}$$

Note the factor of 2, that comes from the fact that the electric field $\vec{E}(t)$ is real, so $\tilde{E}(-\omega) = \tilde{E}(\omega)$. Including the factor 2 allows us to consider only positive frequencies in the spectral energy distribution. Finally, substituting from Eq. (2.13), we have:

$$\frac{d^2W}{d\omega \, d\Omega} = \frac{\omega^2 e^2}{16\pi^3 \epsilon_0 c} \left| \int_{-\infty}^{\infty} (\vec{n} \times (\vec{n} \times \vec{\beta})) \, e^{i\omega(t' + \frac{r}{c})} \, dt' \right|^2. \tag{2.19}$$

Eq. (2.19) is a general expression for the spectral energy distribution (energy per unit frequency range per unit solid angle) emitted by a relativistic charged particle in a magnetic field. $\vec{n}$ is a (constant) unit vector from the magnetic field to the observer. Note that the velocity $\vec{\beta}$ of the particle is a function of the retarded time t'. Therefore, the spectral energy distribution depends on the Fourier transform of the particle's velocity as a function of time.

2.1.4 Undulator Radiation

The spectral energy distribution of synchrotron radiation from a particle with a given trajectory can be calculated from Eq. (2.19). There are a number of 'standard' systems (e.g. a dipole magnet) for which the integral in Eq. (2.19) can be performed. We are interested in the case of a helical undulator. In this case, the trajectory of an electron is a helix, with period equal to the period of the undulator, and amplitude depending on the strength of the magnetic field and the energy of the electron. The integral in Eq. (2.19) is quite complicated in this case, but it has been performed [34]. The result is:

$$\frac{d^2W}{d\omega \, d\Omega} = \frac{\omega^2 e^2 K^2}{4\pi^3 \epsilon_0 c \omega_0^2 \gamma^2} \sum_{n=1}^{\infty} \left[J_n'^2(x) + \left(\frac{\gamma\theta}{K} - \frac{n}{x} \right)^2 J_n^2(x) \right] \frac{\sin^2\left[N\pi \left(\frac{\omega}{\omega_1} - n \right) \right]}{\left(\frac{\omega}{\omega_1} - n \right)^2}. \tag{2.20}$$

Here, γ is the relativistic factor for a particle in the undulator, θ is the angle between the undulator axis and the observation point, and N is the number of periods in the undulator. Other quantities appearing in this expression are as follows:

$$K = \frac{\lambda_u e B}{2\pi m_e c^2}, \tag{2.21}$$

$$x = \frac{K\theta}{\gamma}\frac{\omega}{\omega_0}, \tag{2.22}$$

$$\omega_0 = \frac{2\pi\beta^* c}{\lambda_u}, \tag{2.23}$$

$$\omega_1 = \frac{\omega_0}{1-\beta^*\cos\theta}. \tag{2.24}$$

λ_u is the undulator period, and B is the field strength. β^* is the average velocity of a particle in the longitudinal direction, divided by the speed of light. It is given by [34]:

$$\beta^* = \beta\left[1-\left(\frac{\lambda_u}{2\pi\rho}\right)^2\right]^{\frac{1}{2}} = \beta\left[1-\left(\frac{K}{\gamma}\right)^2\right]^{\frac{1}{2}}, \tag{2.25}$$

where ρ is the radius of the helical motion of a particle in the undulator. Note that ω_0 is the circular frequency of the electron's helical orbit. The physical significance of ω_1 will become clear shortly. For now, we note that for ultrarelativistic particles ($\beta \approx 1$) and for small angles θ, ω_1 can be approximated by:

$$\omega_1 \approx \frac{2\gamma^2\omega_0}{1+K^2+\gamma^2\theta^2}. \tag{2.26}$$

Some interesting properties of the radiation spectrum can be seen by looking at the radiation on the undulator axis. That is, we take the limit $\theta \to 0$. In that case, Eq. (2.20) becomes:

$$\left.\frac{d^2W}{d\omega\, d\Omega}\right|_{\theta=0} = \frac{\omega^2 e^2 K^2}{16\pi^3\epsilon_0 c\omega_0^2\gamma^2}\frac{\sin^2\left[N\pi\left(\frac{\omega}{\omega_1}-1\right)\right]}{\left(\frac{\omega}{\omega_1}-1\right)^2}. \tag{2.27}$$

If the number of undulator periods N is large, then the radiation spectrum has a single sharp peak at $\omega = \omega_1$. For ultrarelativistic particles (i.e. $\beta \approx 1$):

$$\frac{1}{1-\beta^*} \approx \frac{2\gamma^2}{1+K^2}. \tag{2.28}$$

So we can write (for $\theta = 0$):

$$\omega_1 \approx \frac{2\gamma^2}{1+K^2}\omega_0. \tag{2.29}$$

If K is small, then the radiation spectrum on-axis is sharply peaked at $2\gamma^2\omega_0$, as expected from the discussion in Section 2.1.1. As K increases, the frequency of the peak in the spectrum falls. For the undulators we will discuss for positron sources in linear colliders, K is of order 1. K is known as the "deflection parameter".

Let us now consider how the intensity of the radiation varies with the angle θ from the undulator axis. At the peak in the spectrum, $\omega = \omega_1$. Then:

$$\left.\frac{d^2W}{d\omega\, d\Omega}\right|_{\omega=\omega_1} = \frac{e^2K^2N^2}{16\pi\epsilon_0 c\gamma^2}\frac{\omega_1^2}{\omega_0^2}\left[J_1'^2(x) + \left(\frac{\gamma\theta}{K} - \frac{1}{x}\right)^2 J_1^2(x)\right]. \tag{2.30}$$

If $\gamma\theta < 1$, then for $\omega = \omega_1$, $x < 1$. For small x, Eq.(2.20) becomes:

$$\left.\frac{d^2W}{d\omega\, d\Omega}\right|_{\omega=\omega_1} \approx \frac{e^2K^2N^2}{64\pi\epsilon_0 c\gamma^2}\frac{\omega_1^2}{\omega_0^2}. \tag{2.31}$$

Then, using the approximation (again for small θ):

$$\frac{\omega_1}{\omega_0} \approx \frac{2\gamma^2}{1 + K^2 + \gamma^2\theta^2}, \tag{2.32}$$

we find:

$$\left.\frac{d^2W}{d\omega\, d\Omega}\right|_{\omega=\omega_1} \approx \frac{e^2\gamma^2N^2}{16\pi\epsilon_0 c}\frac{K^2}{(1 + K^2 + \gamma^2\theta^2)^2}. \tag{2.33}$$

The intensity of the radiation falls off rapidly for $\gamma\theta > 1 + K^2$. This is consistent with our expectation that the synchrotron radiation from a single particle is emitted in a cone with opening angle $\sim 1/\gamma$ around the instantaneous direction in which the particle is moving. For large K, the radiation from the undulator appears in a larger cone about the axis of the undulator, because of the larger deflection of the particle's trajectory.

Note that the intensity of the radiation scales with the square of the number of periods in the undulator. This fact, and the fact that the radiation spectrum (for large N) consists of a number of sharp peaks, can be understood in terms of interference of the radiation from each period. If the undulator is perfectly periodic, then there will be a fixed phase relationship between the radiation emitted by the particle in each period of the undulator. At frequencies corresponding to integer multiples of the undulator period, there is constructive interference. This enhances the electric field at the observation point by a factor N, so the intensity is increased by a factor N^2. At other frequencies, there is destructive interference, and the intensity is very small. The

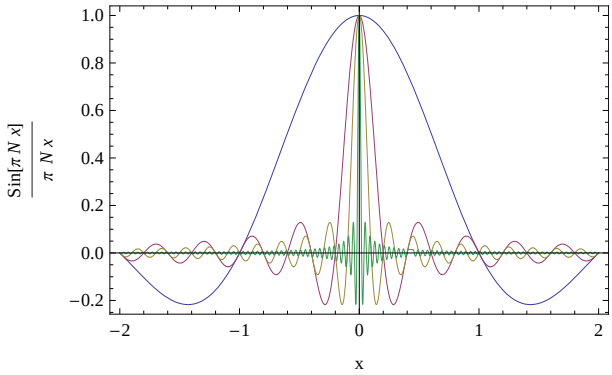

Figure 2.1: Comparison of linewidth of radiation with different number of periods N of a helical undulator.

effect of increasing the number of periods on the width of the peak in the intensity spectrum is illustrated in Fig. 2.1.

For an undulator-based positron source, the undulator may need to be very long, perhaps tens or hundreds of metres. In practice, the undulator would be made from many short sections. Within each section, we expect there to be interference between different periods. But between different sections, there will not be any interference. Therefore, the total intensity from the undulator would vary with the square of the number of periods in one section, and linearly with the number of sections. In practice, each undulator section will have of order 100 periods. Therefore, we can assume that N is large.

For large N, the radiation spectrum has sharp peaks at frequencies ω_n, given by:

$$\omega_n = n\omega_1 \approx \frac{2\gamma^2}{1 + K^2 + \gamma^2\theta^2} n\omega_0. \tag{2.34}$$

γ is the relativistic factor of the particles in the undulator, which we assume is fixed. K and ω_0 are then determined by the undulator period and field strength. Then, the frequencies at which peaks in the spectrum occur have a one-to-one relationship with the angle θ between the axis of the undulator and the observation point. This is illustrated in Fig. 2.2.

The total energy radiated by particles in the undulator can be found by integrating Eq. (2.20). Integrating over all angles produces the energy spectra shown in Fig. 2.3. The peaks in the spectrum correspond to different harmonics. The peaks are "smoothed out" towards lower energies, because the positions of the peaks depend on the angle of

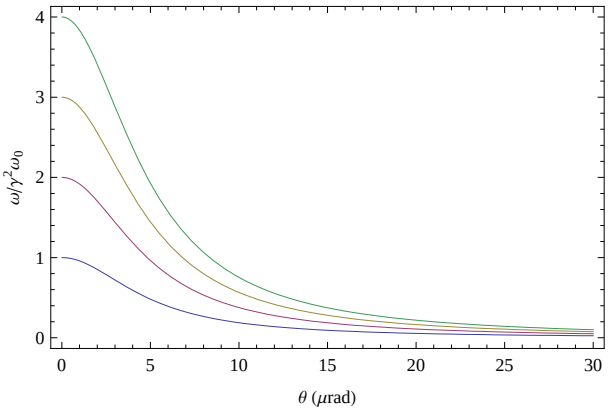

Figure 2.2: Frequency of undulator radiation as a function of angle θ for the first four harmonics.

observation.

Fig. 2.3 shows the energy spectrum of undulator radiation for a large number N of periods. Taking the limit of large N makes it easier to calculate the shape of the spectrum, because the final factor in Eq. (2.20) can be approximated by a Dirac delta function:

$$\lim_{N\to\infty} \frac{\sin^2\left[N\pi\left(\frac{\omega}{\omega_1}-n\right)\right]}{\left(\frac{\omega}{\omega_1}-n\right)^2} = N^2\pi^2\delta\left(\frac{\omega}{\omega_1}-n\right). \tag{2.35}$$

The effect of interference between different undulator periods can be seen in Fig. 2.4. The spectrum converges quite quickly. Between $N = 100$ and the large N limit, the change in the height of the peak at the first harmonic is only 4.3%.

2.1.5 Photon Number Spectrum

The discussion of undulator radiation in the previous section used a purely classical model. However, for a positron source, it is not the intensity of radiation at a given frequency that matters, but the number of photons at that frequency. For example, even if the intensity is very high, if the photon energy is below the threshold for pair production, no positrons will be created.

Using the relationship between the radiation frequency ω and photon energy E_γ:

$$E_\gamma = \hbar\omega, \tag{2.36}$$

we can calculate the photon number spectrum very easily from Eq. (2.20). We simply

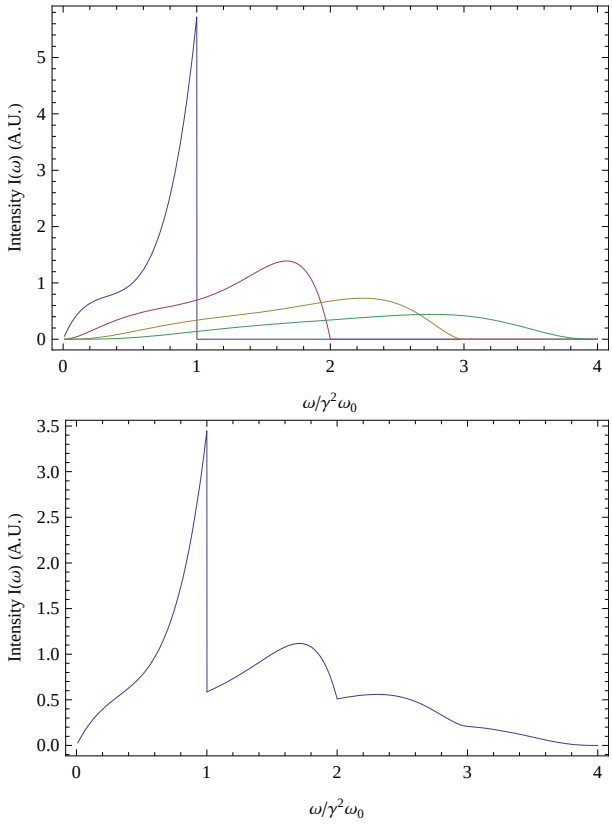

Figure 2.3: Intensity spectrum for radiation from a helical undulator with a large number of periods, N. The top plot shows the intensity of different harmonics. The bottom plot shows the total (sum of all harmonics). Note that for an undulator with a large number of periods, there is a strong correlation between the frequency of the radiation and the angle of propagation of the radiation with respect to the undulator axis. For each harmonic, the frequency and intensity of the radiation increases towards the axis of the undulator. Thus, the sharp peak at $\omega/\gamma^2\omega_0$ is associated with radiation from the first harmonic emitted directly along the undulator axis.

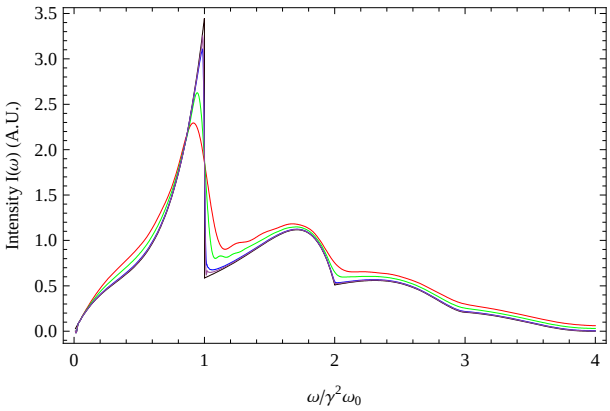

Figure 2.4: Intensity spectrum for radiation from a helical undulator with different numbers of periods, N. Red: $N = 5$. Green: $N = 10$. Blue: $N = 50$. Black: $N = 100$.

need to divide by $\hbar\omega$. The number of photons per unit energy range from a helical undulator is shown in Fig. 2.5.

2.1.6 Polarisation

The polarisation of the positron beam produced from an undulator-based source depends on the polarisation of the photons hitting the target. A circularly polarised wave can be written as the superposition of two linearly polarised waves, with a phase difference between them. In complex notation, the electric field is:

$$\vec{E} = E_x\hat{x} + E_y\hat{y} = E_{x0}e^{-i\omega t}\hat{x} + E_{y0}e^{-i\omega t}\hat{y}, \tag{2.37}$$

where $\hat{x}$ and $\hat{y}$ are unit vectors in the x and y directions, and E_{x0} and E_{y0} are complex wave amplitudes. The rate of circular polarisation can be expressed:

$$P_3 = \frac{\mathrm{Im}\left(E_x E_y^* - E_x^* E_y\right)}{|E_x|^2 + |E_y|^2}. \tag{2.38}$$

Note that $|P_3| \leq 1$; $P_3 = 0$ if E_{x0} and E_{y0} are in phase (linearly polarised wave); and $P_3 = \pm 1$ if $E_{x0} = \pm iE_{y0}$ (circularly polarised wave).

Now, in Eq. (2.20), the first term in square brackets is associated with one component of the electric field, while the second term is associated with the perpendicular component. This allows us to write down an expression for the polarisation of the radiation from a helical undulator, as a function of frequency, and angle with respect

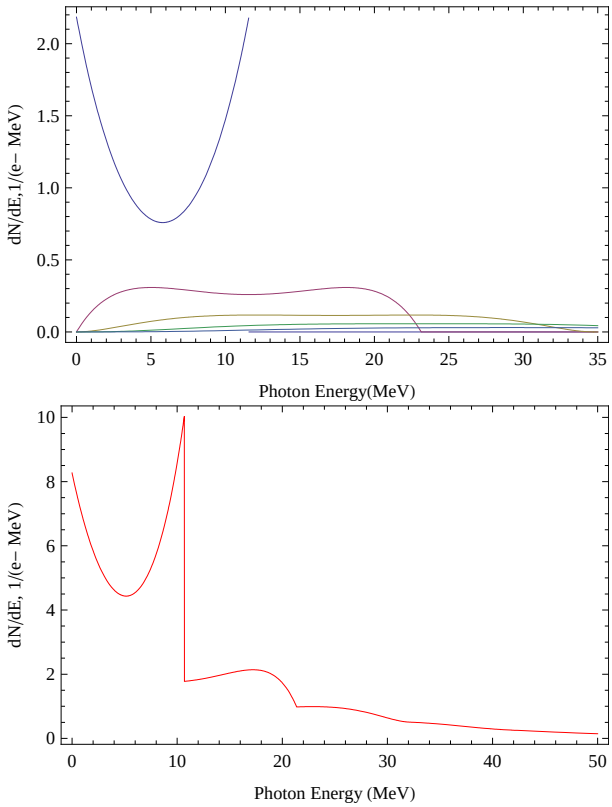

Figure 2.5: Number of photons per unit energy range from a helical undulator. Top: photons from each undulator harmonic. Bottom: total number of photons (sum over harmonics).

to the undulator axis:

$$P_3 = \frac{S_3}{S_0}, \tag{2.39}$$

where:

$$S_3 = -2\sum_{n=1}^{\infty}\left[J_n'(x)\left(\frac{\gamma\theta}{K}-\frac{n}{x}\right)J_n(x)\right]\frac{\sin^2\left[N\pi\left(\frac{\omega}{\omega_1}-n\right)\right]}{\left(\frac{\omega}{\omega_1}-n\right)^2}, \tag{2.40}$$

and:

$$S_0 = \sum_{n=1}^{\infty}\left[J_n'^2(x)+\left(\frac{\gamma\theta}{K}-\frac{n}{x}\right)^2 J_n^2(x)\right]\frac{\sin^2\left[N\pi\left(\frac{\omega}{\omega_1}-n\right)\right]}{\left(\frac{\omega}{\omega_1}-n\right)^2}. \tag{2.41}$$

Fig. 2.6 shows the rate of circular polarisation as a function of frequency (integrated over all angles) of radiation from helical undulators with different numbers of periods. The polarisation of a positron beam produced by the radiation hitting a target will

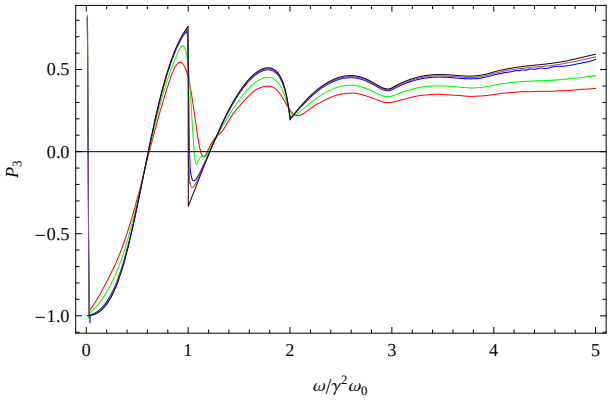

Figure 2.6: Polarisation as a function of normalised frequency. Different colours show different numbers of periods in the undulator, $N = 5$ (red), 10 (green), 50 (blue), 100 (purple), ∞ (black).

depend on the integral over frequency of the photon flux convolved with the polarisation of the radiation and the pair production cross section. If the undulator has a large number of periods, then there is a strong correlation between the frequency of the radiation and the angle at which it is emitted. We see from Fig. 2.6 that it may be possible to control the overall polarisation of the radiation by collimating the beam to remove low energy (large angle) photons for which the polarisation varies over a wide range. The photon collimator will be discussed in more detail in Section 2.2.

2.1.7 Photon Generator in FLUKA

The figures in the previous sections showing the radiation intensity and polarisation as functions of frequency were produced by implementing the analytical expressions in Mathematica. For modelling the undulator-based positron source, it is convenient to include the generation of a photon beam with the appropriate properties in a simulation code that can be used for tracking the photons through the parts of the system downstream from the undulator. This includes the photon collimator and the target. Issues for the photon collimator include energy deposition and activation. A suitable code for modelling this component is FLUKA [35]. Therefore, we have developed code for generating a photon beam with the correct properties within FLUKA.

FLUKA is a Monte Carlo code for simulating and calculating particle transport and interactions with matter with high accuracy [36]. In our simulations, a realistic primary

photon beam will be generated with certain energy and angle distributions, and degree of polarisation (P_3). A special "collision tape" will be written to record the activity of each primary photon. From the tape file, we can obtain useful information, such as the photon number spectrum and polarisation before and after the photon collimator. However, before we show the results for the photon collimator, we show the results of the photon generator from FLUKA.

Fig. 2.7 shows the photon number spectrum from FLUKA, and Fig. 2.8 shows the polarisation. These plots should be compared with Figs. 2.5 and 2.6 respectively. The FLUKA simulations are in good agreement with the analytical expressions. Therefore, we feel confident in using the photon beam generated in FLUKA for the simulations of the photon collimator. Producing the correct polarisation properties is important, as it allows us to investigate the use of the collimator for improving the polarisation of the positron beam, as well as its use for protecting downstream systems from stray photons.

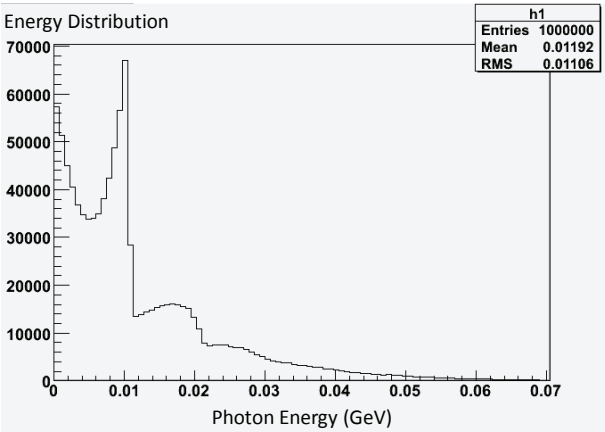

Figure 2.7: Photon number spectrum from FLUKA simulation.

2.2 Photon Collimator

A positron source based on a helical undulator provides the capability of producing a beam of polarised positrons. In this process, the main electron beam will go through a helical undulator to produce high energy photons, which will then strike a thin rotating target to generate positrons by pair production. There is an extra component located

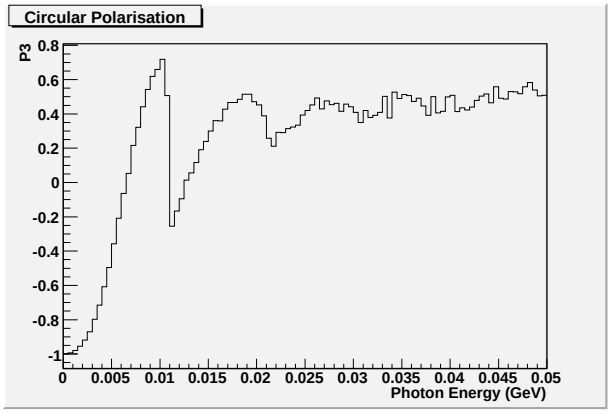

Figure 2.8: Photon polarisation rate P_3 as function of energy, from FLUKA simulation.

downstream of the undulator but before the target: this is the photon collimator. The collimator may help to protect downstream components from a photon beam with some angle or intensity error. Also, by adjusting the aperture of the photon collimator, it will help to stop the halo of the photon beam, by removing the particles that are further away from the axis. We know from the previous section that there is a strong correlation between photon energy and angle, with low energy photons having larger angles. The low energy photons will not contribute much to the positron production; however, they will increase the energy deposition (and hence the temperature rise and activation) in the target. Therefore, it may provide some advantages to use a photon collimator to increase the positron production efficiency without increasing the energy deposition, by cutting off the wider angle photons. Furthermore, the photon collimator may also improve the polarisation of the photons, and hence of the positrons. This is because the degree of polarisation of the positrons depends upon the polarisation of the photons produced from the undulator; and the polarisation of the photons in turn depends on the photon energy which is correlated with the angle. To investigate the function of the collimator in removing large-angle photons and improving the polarisation, we have carried out simulations in FLUKA, using the photon energy spectrum and polarisation for one design of the helical undulator. The results are presented in detail in later chapters. In the remaining parts of this section, we present the results of some simple benchmark tests of FLUKA, looking at the energy deposition in a block of titanium from different initial photon energies.

2.2.1 Electromagnetic Showers

When high energy photons pass through a material, pair production is the dominant process by which they lose energy. The secondary particles produced in the electromagnetic processes are mainly positrons, electrons and photons. These particles again lose energy on their way through the material via collision and radiation processes. The collisions account for the majority of heat deposititon in the material, while photons are generated by radiation processes. The cascade shower develops through repeated similar interactions. As the shower develops, the number of cascade particles will increase exponentially (so the mean energy will decrease) until the energy of the shower particles is low enough to stop further multiplication. From this point the shower decays slowly through ionization losses for electrons, or by Compton scattering and the photoelectric effect for photons. This change is characterized by the critical energy ϵ which is approximated by [37]:

$$\epsilon \approx \frac{800\,\mathrm{MeV}}{Z + 1.2} \tag{2.42}$$

where Z is the atomic number.

A useful quantity when describing the interaction of high energy electrons and photons with matter is the radiation length, X_0. The radiation length is distance in a material over which a high energy electron loses (by bremsstrahlung) all but a fraction $1/e$ of its initial energy. The radiation length is also equal to 7/9 of the mean free path for pair production by a high energy photon. To a good approximation, the radiation length (in units of distance) is given by:

$$X_0 = \frac{A}{Z(Z+1)\ln\left(\frac{287}{\sqrt{Z}}\right)} \times \frac{716.4\,\mathrm{g/cm^2}}{\rho}. \tag{2.43}$$

A typical photon collimator consists of a spoiler and an absorber. The primary photon beam with energy E_0, when it hits the spoiler, develops a cascade. This process is dominated by pair production. This cascade propagates in the material and is then absorbed by the absorber. The cascade spreads inside the matter until the energy of the particles falls below the critical energy ϵ. The maximum transverse size of the cascade is of the order of the Moliere radius which is given approximately by:

$$R_M \approx 0.0265 X_0 (Z + 1.2), \tag{2.44}$$

where X_0 is the radiation length.

Reference [37] suggests that the cascade will reach a maximum depth of:

$$t_{max} \approx \ln\left(\frac{E_0}{\epsilon}\right) - a, \tag{2.45}$$

in units of the radiation length. Here $a = 0.5$ for photons, E_0 is the energy of incident particles, and ϵ is the critical energy of the material. In general, the incident particle energy should be higher than the critical energy. In later section, we will run the test by using 20 MeV, 40 MeV and 80 MeV, in which two of them are lower than the critical energy. The results will be negative. We will take the absolute value as an approximation for this first benchmark test. The shower depth for 95% of longitudinal containment is given approximately by:

$$t_{95\%} \approx t_{max} + 0.08Z + 9.6. \tag{2.46}$$

The transverse shower dimension with 95% containment is given approximately by:

$$R_{95\%} \approx 14\frac{A}{Z}. \tag{2.47}$$

Both $t_{95\%}$ and $R_{95\%}$ are given in units of the radiation length.

2.2.2 FLUKA Benchmarking

We can compare the results of simulations with these simple theoretical formulae. Since the average photon energy from the ILC helical undulator is ~10 MeV, which is lower than the predicted critical energy of the titanium found from the equation, we have also run the simulations with photon energies of 40 MeV and 80 MeV. In these benchmark tests, we have used a solid cylinder made of titanium with length of 90 cm and radius of 50 cm. Titanium has atomic weight $A = 47.867$, atomic number $Z = 22$, density $\rho = 4.5\,\mathrm{g/cm^3}$ and radiation length $X_0 = 3.59\,\mathrm{cm}$.

Based on Eqs. (2.44) – (2.47), we can calculate the shape of the cascade shower. Table 2.1 shows the theoretical cascade shower longitudinal and transverse containment in titanium for different initial photon energies.

In order to compare these approximations with the FLUKA simulations, we first of all look at the longitudinal direction. The titanium cylinder body will be divided into two sections, where the length of the first region is given by the value for the

Table 2.1: Theoretical cascade shower longitudinal and transverse containment in titanium.

Photon Energy (MeV)	95% longitudinal (cm)	95% transverse (cm)
10	34.8	6.7
40	39.5	6.7
80	42.0	6.7

Photon energy E_0 (MeV)	Energy deposited			% energy deposited in Region 1
	Total (MeV)	Region 1 (MeV)	Region 2 (MeV)	
10	9.936	9.67	0.266	97.3%
40	39.87	39.3	0.56	98.6%
80	79.83	78.77	1.06	98.7%

Table 2.2: FLUKA results of energy deposition in Region 1 and Region 2 in the longitudinal direction.

95% longitudinal containment from Table 2.1. This region is referred to as Region 1. The remaining section of the cylinder body is referred to as Region 2. In principle, the energy deposition in Region 1 will be approximately equal to 95% of the total energy deposition. The simulation results are presented in Table 2.2. We see that at all three initial photon energies, there is slightly more energy deposited in Region 1 than expected from the approximate formulae, but the agreement is reasonable.

Next, we look at the energy deposition in the transverse direction. The titanium cylinder will be redefined. This time, the cylinder is separated into two concentric cylinders. The inner cylinder with radius of $R = 6.7\,\text{cm}$ (based on the expected radius containing 95% of the energy deposition) is referred to as Region 3, and the outer cylinder is Referred to as Region 4. The results from tracking in FLUKA are shown in Table 2.3. Again, the results from FLUKA are in reasonable agreement with the predictions of the approximate formula.

Table 2.3: FLUKA results of energy deposition in Region 3 and Region 4 in the transverse direction.

Photon energy E_0 (MeV)	Energy deposited			% energy deposited in Region 3
	Total (MeV)	Region 3 (MeV)	Region 4 (MeV)	
10	9.935	9.54	0.395	96.01%
40	39.865	37.8	2.065	94.8%
80	79.876	75.02	4.756	94.1%

2.3 Positron Production Target

The target is located downstream of the photon collimator. Positrons are generated by pair production when high energy photons from the undulator hit the target. The production rate will be high if there is a high average photon energy, of 10-30 MeV. There are two main factors affecting the choice of photon energy. First, the pair production cross section is approximately constant for high photon energy. At low energy, the pair production cross section decreases rapidly. Secondly, at high photon energy, the positrons produced also have high energy, and are more likely to escape from the target without significant energy losses from ionization and other processes. Ideally, the positron energy should be above 2 MeV.

In a conventional undulator source, electrons impacting the target produce high energy photons by bremsstrahlung. The high energy photons are then converted into electron-positron pairs by interaction with the atoms in the material. The overall process is not very efficient, so a conventional target needs to be quite thick, about 4 - 6 radiation lengths. In an undulator-based source, the primary beam on the target consists already of high energy photons. This makes the production of positrons more efficient, so the target needs to have a thickness of only about 0.4 radiation lengths. Compared to a target in a conventional positron source, the target in an undulator-based source can either be physically thinner, using a smaller amount of material; or, it can be made of a material with a longer radiation length. From point of view of energy deposition in the target, it is better to make the target from a material with a large radiation length. This leads to a large heat capacity of the volume within which the energy is deposited, and reduces the thermal stresses on the target. Broadly

speaking, materials with a high nuclear charge Z have short radiation lengths, while low Z materials have longer radiation lengths. The ideal material for a positron production target should have a high specific heat capacity, and good mechanical properties such as a low coefficient of thermal expansion. At the same time, we need the Z value to be not too low, since the cross section of pair production is a rapidly increasing function of the atomic number of the material. By combining all these consideration, and taking into account energy deposition, pair production cross section, conductivity, thermal conditions and mechanical strength, titanium alloy provides a good choice of material for the target.

The present design for the ILC positron source target is based on a wheel constructed from Ti-6%A-l4%V, about 1 m in diameter, and rotating to provide a rim velocity of about 100 m/s. The rim is connected to a central drive shaft using five struts. The target will need to be water cooled through internal channels. After some period of operation, the target will become activated, so a remote handling system will be needed [38].

The positrons generated from the target have a large transverse spread and divergence. To capture the beam efficiently, a strong magnetic field must be used. A good capture efficiency means that the number of initial photons can be reduced, so that the undulator can be shorter and the target energy deposition will be smaller as well. However, the highest capture efficiency is achieved when the target is immersed in a strong magnetic field, which could be up to 6 T. A rotating target in such a high magnetic field will generate large eddy currents. One of the most important factors that will affect the eddy current is the speed of rotation, which depends on the beam structure. Rotating the target rapidly will allow a long pulse of beam to be distributed over a larger area in target, in which case, the energy deposition per unit volume will be reduced. Because of the different time structure of the beams in CLIC and ILC, the issues are somewhat different for the two machines, and will be discussed in more detail in later chapters.

In order to investigate and understand the mechanical properties of the target wheel and the eddy current effects, a target wheel prototype has been built at the Cockcroft Institute. The experiment will be described in detail, and data analysis will be presented, in Chapter 5.

2.4 Matching Device

Positrons from the target are accelerated by a linac, in which transverse focusing is provided by a uniform solenoid field of strength 0.5 T. To minimise losses, the beam at the entrance to the RF section should have a transverse phase space correctly matched to the solenoid field, which means that the distribution will simply rotate as the beam moves along the solenoid, without any variation in transverse size. A beam will be correctly matched to a solenoid of field strength B_s if, at the entrance to the solenoid, the beam distribution is characterised by a beta function with value:

$$\beta = 2\frac{B\rho}{B_s} \tag{2.48}$$

where $B\rho$ is the beam rigidity. For the case of the positron source, it is difficult to specify the beam rigidity, since the energy spread is very large. However, taking an average value using a typical distribution, it is found that the transverse phase space distribution would generally be matched to a solenoid field much larger than 0.5 T. Therefore, an optical component is needed to transform the phase space at the exit of the target, to the phase space matched to the 0.5 T solenoid in the first accelerating section. This optical component is generally known as a matching device. Different types of matching device could be used, including a quarter wave transformer, and an adiabatic matching device. A quarter wave transformer simply consists of a solenoid with high uniform field strength. The field strength and length are determined by the matching condition. An adiabatic matching device consists of a solenoid in which the field strength varies smoothly from a high value at the entrance to a lower value at the exit. Again, the parameters are determined by the matching condition.

Phase space matching with a solenoid can be understood by use of the transfer matrix M for (the transverse variables in) a solenoid [39]:

$$M = \begin{pmatrix} \cos^2(\omega L) & \frac{\sin(2\omega L)}{2\omega} & \frac{\sin(2\omega L)}{2} & \frac{\sin^2(\omega L)}{\omega} \\ -\frac{\omega\sin(2\omega L)}{2} & \cos^2(\omega L) & -\omega\sin^2(\omega L) & \frac{\sin(2\omega L)}{2} \\ -\frac{\sin(2\omega L)}{2} & -\frac{\sin^2(\omega L)}{\omega} & \cos^2(\omega L) & \frac{\sin(2\omega L)}{2\omega} \\ \omega\sin^2(\omega L) & -\frac{\sin(2\omega L)}{2} & -\frac{\omega\sin(2\omega L)}{2} & \cos^2(\omega L) \end{pmatrix} \tag{2.49}$$

where L is the length of the solenoid field, and ω is given by:

$$\omega = \frac{eB_s}{2P_0}. \tag{2.50}$$

Note that Eq. (2.49) gives the transfer matrix for a solenoid in terms of canonical variables, in which the transverse momenta are defined by:

$$p_x = \frac{1}{P_0}\left(\gamma m v_x + eA_x\right), \tag{2.51}$$

$$p_y = \frac{1}{P_0}\left(\gamma m v_y + eA_y\right), \tag{2.52}$$

where v_x and v_y are the transverse velocities, A_x and A_y are the transverse components of the electromagnetic vector potential, and P_0 is the reference momentum. Note that P_0 is a normalisation factor used in the definition of the normalised momenta and normalised field strengths; as long as a consistent value is used, the value of P_0 can be chosen arbitrarily for these definitions. However, it is conventional to choose the reference momentum to be as close as possible to the nominal momentum of the beam. In that case, the energy deviation of a particle, defined by:

$$\delta = \frac{E - E_0}{E_0} \tag{2.53}$$

where E is the particle energy and E_0 is the energy of a particle with the reference momentum, will generally be a small quantity ($|\delta| \ll 1$). This makes it possible to use a number of convenient approximations when tracking particles through a beam line.

The solenoid transfer matrix given in (2.49) can be written as:

$$M = R \cdot \tilde{M}, \tag{2.54}$$

where R is a rotation in coordinate space:

$$R = \begin{pmatrix} \cos(\omega L) & 0 & \sin(\omega L) & 0 \\ 0 & \cos(\omega L) & 0 & \sin(\omega L) \\ -\sin(\omega L) & 0 & \cos(\omega L) & 0 \\ 0 & -\sin(\omega L) & 0 & \cos(\omega L) \end{pmatrix}, \tag{2.55}$$

and $\tilde{M}$ is given by:

$$\tilde{M} = \begin{pmatrix} \cos(\omega L) & \frac{\sin(\omega L)}{\omega} & 0 & 0 \\ -\omega \sin(\omega L) & \cos(\omega L) & 0 & 0 \\ 0 & 0 & \cos(\omega L) & \frac{\sin(\omega L)}{\omega} \\ 0 & 0 & -\omega \sin(\omega L) & \cos(\omega L) \end{pmatrix}. \tag{2.56}$$

Note that $\tilde{M}$ is in the form of a transfer matrix for an element with constant equal horizontal and vertical focusing strength ω. A phase space distribution with Twiss beta

and alpha functions (horizontal and vertical) given by:

$$\beta = \frac{1}{\omega}, \qquad \text{and} \qquad \alpha = 0, \tag{2.57}$$

remains invariant under a transformation defined by $\tilde{M}$. That is:

$$\Sigma \mapsto \tilde{M} \cdot \Sigma \cdot \tilde{M}^{\mathrm{T}} = \Sigma, \tag{2.58}$$

where Σ is the matrix of second-order moments of the beam distribution, given in this case by:

$$\Sigma = \begin{pmatrix} \frac{\varepsilon_x}{\omega} & 0 & 0 & 0 \\ 0 & \omega\varepsilon_x & 0 & 0 \\ 0 & 0 & \frac{\varepsilon_y}{\omega} & 0 \\ 0 & 0 & 0 & \omega\varepsilon_y \end{pmatrix}, \tag{2.59}$$

where ε_x and ε_y are the beam emittances.

Eqs. (2.54) and (2.58) show that a beam distribution given by Eq. (2.59) will, if the emittances are equal, remain invariant as the beam moves along the solenoid. Such a distribution is said to be correctly matched to the solenoid. Alternatively, for a given distribution, one can say that the solenoid is correctly matched to the distribution. The motion of an individual particle can be described as a rotation in phase space (through angle ωL), where the coordinate system itself is also rotating (again through angle ωL). If a distribution is not correctly matched to a solenoid, then the beam size will oscillate as the beam moves through the solenoid. This increases the chances of losing particles at points where the transverse extent of the distribution is largest. Generally, one expects to minimise particle losses if the distribution and the solenoid are correctly matched to each other.

There are two kinds of matching devices commonly proposed for use in an undulator-based positron source: a quarter wave transformer and an adiabatic matching device. In both cases, the intention is to control the phase space distribution of the positrons from the source, so that when the positrons reach the capture RF, the distibution is correctly matched to the focusing solenoid in this section. In the capture RF, transverse focusing is provided by a solenoid of field strength 0.5 T. The strength of the solenoid defines the shape of the matched distribution. The size of the distribution, given by the emittances, is not determined by the strength of the solenoid.

Note that the focusing strength of the solenoid, ω depends on the reference momentum P_0. This implies that the focusing strength depends on the particle energy.

This is indeed the case, and means that the matched distribution will be a function not only of the transverse variables, but also of the longitudinal variables. In a positron source, there is limited control over the shape of the distribution of the positrons coming directly from the target. In particular, there is usually an extremely wide energy spread. This means it will not be possible, in general, to design the optics to match perfectly the disribution of the positrons from the source. The optimum parameters for the matching device to minimise positron losses must be determined by simulation.

2.4.1 Quarter Wave Transformer

A quarter wave transformer consists of a short section of constant high magnetic (solenoid) field, dropping abruptly in strength to the value of magnetic field used for focusing in the linac. The length and strength of the high field solenoid are chosen so that $\omega L = \pi/2$. In this case, the transfer matrix for the solenoid becomes [40]:

$$M = \begin{pmatrix} 0 & 0 & 0 & \frac{1}{\omega} \\ 0 & 0 & -\omega & 0 \\ 0 & -\frac{1}{\omega} & 0 & 0 \\ \omega & 0 & 0 & 0 \end{pmatrix}. \tag{2.60}$$

If the initial positron distribution (immediately after the target) is given by:

$$\Sigma_0 = \begin{pmatrix} \beta_0\varepsilon_x & 0 & 0 & 0 \\ 0 & \frac{\varepsilon_x}{\beta_0} & 0 & 0 \\ 0 & 0 & \beta_0\varepsilon_y & 0 \\ 0 & 0 & 0 & \frac{\varepsilon_y}{\beta_0} \end{pmatrix}, \tag{2.61}$$

then the distribution at the exit of the quarter wave transformer is given by:

$$\Sigma_1 = \begin{pmatrix} \frac{\varepsilon_y}{\beta_0\omega^2} & 0 & 0 & 0 \\ 0 & \beta_0\omega^2\varepsilon_y & 0 & 0 \\ 0 & 0 & \frac{\varepsilon_x}{\beta_0\omega^2} & 0 \\ 0 & 0 & 0 & \beta_0\omega^2\varepsilon_x \end{pmatrix}. \tag{2.62}$$

If the strength of the solenoid field is chosen so that:

$$\omega^2 = \frac{1}{\beta_0\beta_1}, \tag{2.63}$$

then the distribution at the exit of the quarter wave transformer becomes:

$$\Sigma_1 = \begin{pmatrix} \beta_1\varepsilon_y & 0 & 0 & 0 \\ 0 & \frac{\varepsilon_y}{\beta_1} & 0 & 0 \\ 0 & 0 & \beta_1\varepsilon_x & 0 \\ 0 & 0 & 0 & \frac{\varepsilon_x}{\beta_1} \end{pmatrix}. \tag{2.64}$$

Finally, if $\beta_1 = \omega_1$, where ω_1 is the focusing strength of the solenoid in the capture RF (at the exit of the quarter wave transformer), then we see that the quarter wave transformer provides a way of transforming the known distribution at the exit of the target, to the matched distribution at the entrance of the capture RF. The strength of the quarter wave transformer is determined by the beta function of the positron distribution at the exit of the target, and the strength of the solenoid that provides the focusing in the capture RF. The length L of the quarter wave transformer is determined by the condition $\omega L = \pi/2$, where ω is the focusing strength of the solenoid field in the quarter wave transformer.

As mentioned above, "perfect" matching can only be achieved for a beam with zero energy spread. This is certainly not the case with the positron beam from the target. The parameters of the quarter wave transformer can be estimated from the theoretical conditions, but must be optimised (to minimise positron losses) by carrying out simulations.

2.4.2 Adiabatic Matching Device

An adiabatic matching device consists of a solenoid field with a strength that varies along its length. At a distance z from the entrance of the adiabatic matching device, the longitudinal field is given by [41]:

$$B_z(z) = \frac{B_0}{1+gz}, \tag{2.65}$$

where B_0 is the magnetic field at the entrance ($z = 0$), and g is a constant known as the "taper parameter". The taper parameter describes the rate of variation of the field along the length of the adiabatic matching device.

An approximation to the transfer matrix in an adiabatic matching device has been derived by Helm [42]:

$$M = \begin{pmatrix} A\cos^2(\mu) & \frac{B}{2}\sin(2\mu) & \frac{A}{2}\sin(2\mu) & B\sin^2(\mu) \\ -\frac{1}{2B}\sin(2\mu) & \frac{1}{A}\cos^2(\mu) & -\frac{1}{B}\sin^2(\mu) & \frac{1}{2A}\sin(2\mu) \\ -\frac{A}{2}\sin(2\mu) & -B\sin^2(\mu) & A\cos^2(\mu) & \frac{B}{2}\sin(2\mu) \\ \frac{1}{B}\sin^2(\mu) & -\frac{1}{2A}\sin(2\mu) & -\frac{1}{2B}\sin(2\mu) & \frac{1}{A}\cos^2(\mu) \end{pmatrix}, \tag{2.66}$$

where:

$$\mu = \frac{e}{P_0}\frac{B_0}{2}\int_0^{z_{\max}} \frac{1}{1+gz}\,dz, \tag{2.67}$$

$$A = \sqrt{\frac{B_0}{B_1}}, \tag{2.68}$$

$$B = \frac{2P_0}{e\sqrt{B_0 B_1}}. \tag{2.69}$$

B_1 is the field at the exit of the adiabatic matching device ($z = z_{\max}$).

Note that if $g = 0$, the solenoid field is constant; then, $B_1 = B_0$, and we find that the transfer matrix is the same as that for a solenoid, as we would expect.

If $\mu = \pi/2$, then the transfer matrix becomes:

$$M = \begin{pmatrix} 0 & 0 & 0 & B \\ 0 & 0 & -\frac{1}{B} & 0 \\ 0 & -B & 0 & 0 \\ \frac{1}{B} & 0 & 0 & 0 \end{pmatrix}. \tag{2.70}$$

This should be compared with the transfer matrix for a quarter wave transformer, given in Eq. (2.60): we see that if $B = 1/\omega$, i.e.:

$$B = \sqrt{\beta_0 \beta_1}, \tag{2.71}$$

then they are the same. Thus, an adiabatic matching device can be used to match the positron distribution at the exit of the target to the focusing solenoid in the RF section, if the strength and taper parameter are chosen correctly. Using Eqs. (2.50) – (2.57), the field strength at the end of the adiabatic matching device should be equal to the field strength of the focusing solenoid in the capture RF. This field strength is related to the beta function of the positron distribution by:

$$B_1 = \frac{2P_0}{e\beta_1}. \tag{2.72}$$

Then, using Eqs. (2.69) and (2.71), the field strength at the entrance of the adiabatic matching device must be chosen to match the beta function of the positron distribution at the exit of the target:

$$B_0 = \frac{2P_0}{e\beta_0}. \tag{2.73}$$

Finally, the taper parameter should be chosen so that:

$$\mu = \frac{e}{P_0}\frac{B_0}{2}\int_0^{z_{\max}} \frac{1}{1+gz}\, dz = \frac{\pi}{2}. \tag{2.74}$$

As was the case for the quarter wave transformer, the matching condition can only be achieved properly for a positron bunch with zero energy spread. Optimisation of the

parameters of the matching device for a realistic distribution (with large energy spread) must be achieved using simulations. Such simulations will be presented in chapters 3 and 4.

2.4.3 Fringe Fields

Solenoids have fringe fields that can, in some situations, have a significant effect on particle dynamics. In a simple model of the fringe field at the entrance of a solenoid, in which the fields are compressed into a plane perpendicular to the solenoid field B_z, the field has components:

$$\int B_x \, dz = -\frac{1}{2} B_z x, \tag{2.75}$$

$$\int B_y \, dz = -\frac{1}{2} B_z y, \tag{2.76}$$

where the integral extends over the (infinitesimal) length of the fringe field. In this model, the field satisfies the equation:

$$\int \nabla \times \vec{B} \, dz = 0. \tag{2.77}$$

An ultrarelativistic particle with charge e travelling parallel to the solenoid field will receive transverse "kicks" as it crosses the fringe field:

$$\Delta \tilde{P}_x = -e \int B_y \, dz = \frac{1}{2} e B_z y, \tag{2.78}$$

$$\Delta \tilde{P}_y = e \int B_x \, dz = -\frac{1}{2} e B_z x, \tag{2.79}$$

where $\tilde{P}_x = \gamma m v_x$ and $\tilde{P}_y = \gamma m v_y$ are the mechanical momenta.

The canonical momenta are defined by:

$$P_x = \tilde{P}_x + e A_x, \tag{2.80}$$

and similarly for P_y, where A_x is the horizontal component of the electromagnetic vector potential. The magnetic field is derived from the vector potential using:

$$\vec{B} = \nabla \times \vec{A}. \tag{2.81}$$

Therefore, in an appropriate gauge, the field in the body of the solenoid can be derived from the vector potential:

$$A_x = -\frac{1}{2} B_z y, \tag{2.82}$$

$$A_y = \frac{1}{2} B_z x. \tag{2.83}$$

Taking into account the change in mechanical momentum and the change in vector potential as a particle crosses the fringe field, the total change in canonical momentum is:

$$\Delta P_x = 0, \tag{2.84}$$

$$\Delta P_y = 0. \tag{2.85}$$

That is, the canonical momenta are conserved as a particle crosses the fringe field. The change in the vector potential cancels the change in the mechanical momentum. The transfer matrices for the fringe fields (at the entrance and the exit of the solenoid) are equal to the identity. However, this is only the case if canonical variables are used. When modelling the capture optics in a positron source (as with any dynamical system) it is important to be clear and consistent in the variables that are used. For our simulations, we used canonical variables: this means that no explicit map for the fringe field in the matching device needs to be applied, assuming that the "thin fringe" field model can be used.

2.5 Example: Positron Production without Photon Collimator

In this section we consider the production of positrons in an undulator-based source without a photon collimator. The primary photon beam on the target comes directly from the undulator. The parameters of the helical undulator are based on the ILC baseline. The main driving electron beam energy is 150 GeV. The helical undulator has a period of 11.5 mm and the deflection parameter K is equal to 0.92. In the simulation, we use 10^5 primary photon strikes on the target. The average energy of the photons is 10.68 MeV. By pair production, the conversion rate is about 0.023 positrons per photon with a polarisation rate of 26.6%, taking figures directly after the target. The generated positrons will be focused by a matching device. We will use an adiabatic matching device (AMD) with a 6 T peak field and taper parameter of 0.03 mm^{-1}, linking the target with a 0.5 T solenoid and capture RF section. The number of positrons that go through all these devices and are also within the damping ring acceptance is about 0.008 positrons per photon, with a polarisation rate of 29%. If we calculate the yield of the number of positrons per electron per 100 meters of undulator, we find that the

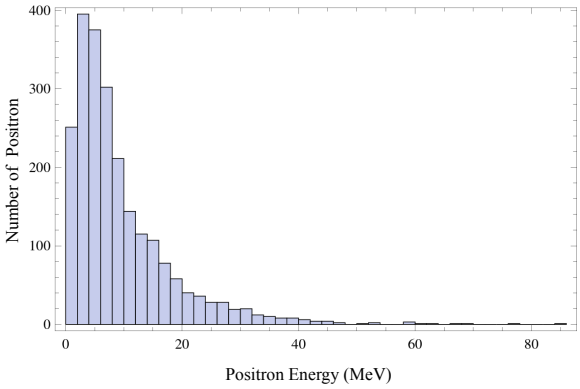

Figure 2.9: Positron energy distribution after target.

yield of positrons is about 1.5, without any collimation.

Fig. 2.9 shows a histogram of the energy distribution of the positrons after the target. As stated in the previous section, the average photon energy is about 10 MeV. From the figure, we can see that there is a peak in the positron energy distribution at about 5 MeV: this is because in pair production, the energy of the photon is divided roughly equally between the electron and the positron. The maximum positron energy is about 80 MeV, though the number of positrons with energy of this order is very small. The average positron energy is about 9.5 MeV. The energy deposited in the target is about 0.8 MeV per primary photon.

Fig. 2.10 shows the positron polarisation rate after the target. The polarisation of the photon beam incident on the target is about 30%, and the average positron polarisation at the exit of the target is about 27%. In order to calculate the average polarisation, we take mean value of S_z, where S_z is the longitudinal component of the spin vector. This means that photon polarisation is transferred to the positron beam, but it is still the case that a more highly polarised photon beam will produce a more highly polarised positron beam.

The transverse coordinate distribution of the positrons is shown in Fig. 2.11, and the transverse momentum distribution is shown in Fig. 2.12. The coordinate distribution is cut at ± 10 mm, corresponding to the aperture of the matching device. The spot size has an rms value of 2 mm; however, there is a large divergence, with the angular spread of the positrons reaching even up to 1 rad. Fig. 2.13 shows the transverse phase space distribution of the positrons after the target. The normalised emittance is about

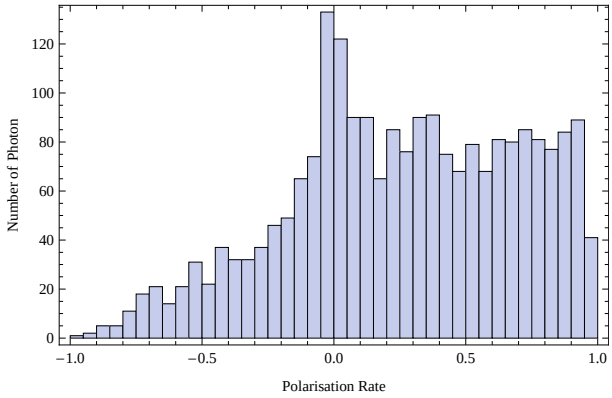

Figure 2.10: Positron polarisation after target.

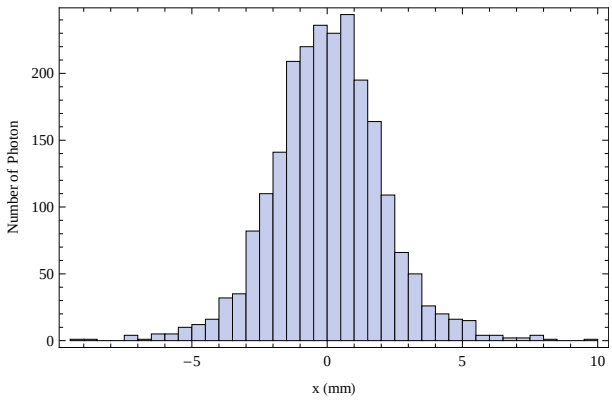

Figure 2.11: Positron transverse position x after target.

25 mm rad. It can be difficult to capture and transport such a large beam without significant losses: the matching device and focusing solenoid in the capture RF play important roles. In Chapters 3 and 4, we discuss the optimisation of the matching device parameters for ILC and CLIC, respectively.

Our simulation studies end after the first RF section: however, we can estimate the overall positron yield by imposing a cut on the distribution at this point, corresponding to the acceptance of the RF, transport line, and damping ring. The transverse acceptance of the damping ring is specified in terms of the largest betatron amplitude of any particle that can be stored after injection into the damping ring. The betatron amplitude is defined as:

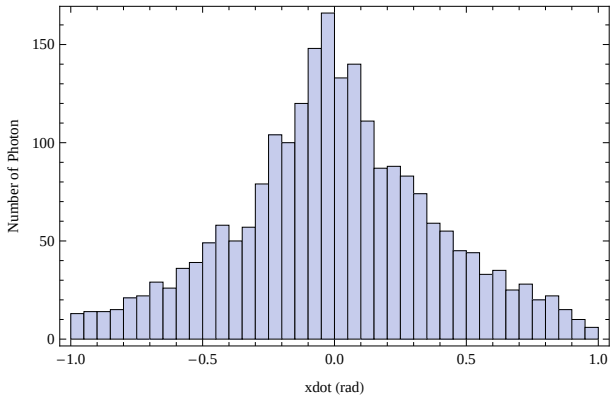

Figure 2.12: Positron divergent direction angle after target. xdot is the positron angle in unit of radian

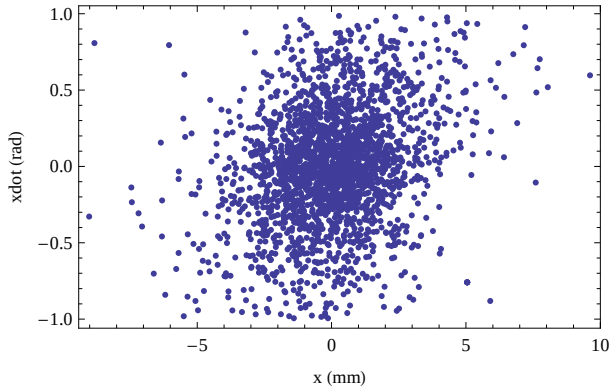

Figure 2.13: Positron transverse phase space distribution after target. xdot is the positron angle in unit of radian

$$A_x = \gamma \left(\gamma_x x^2 + 2\alpha_x x p_x + \beta_x p_x^2 \right), \tag{2.86}$$

where γ is the relativistic factor, x and p_x are the particle coordinate and normalised momentum, and α_x, β_x and γ_x are the Twiss parameters. Note that, neglecting radiation and interactions between particles, the betatron amplitude is conserved during linear transport. The betatron action is also conserved during acceleration, for the following reasons. As a particle is accelerated, the relativistic factor γ increases; however, the reference momentum should also be increased, so that the reference momentum remains close to the nominal momentum of the beam. But because the reference momentum is used to normalise the transverse momentum, an increase in the reference momentum implies a decrease in the normalised momentum p_x, even though the absolute transverse momentum is not changed. This will change the distribution of a beam of particles: the divergence of the beam decreases, which implies a reduction in the Twiss parameter γ_x, and an increase in β_x. If the energy is increased by a factor γ_1/γ_0, so that:

$$\gamma \mapsto \frac{\gamma_1}{\gamma_0}\gamma \tag{2.87}$$

then

$$p_x \mapsto \frac{\gamma_0}{\gamma_1} p_x \tag{2.88}$$

$$\gamma_x \mapsto \frac{\gamma_0}{\gamma_1}\gamma_x \tag{2.89}$$

The coordinate x is unchanged, and the relation $\beta_x\gamma_x - \alpha_x^2 = 1$ implies that the Twiss parameter α_x is also unchanged. Substituting these transformations into Eq. (2.86), we see that the betatron action is invariant during acceleration, if the reference momentum is scaled in proportion to the beam energy. For ILC, the transverse acceptance specification is $A_x + A_y < 90$ mmrad.

A longitudinal spread in particle position is converted into an energy spread in the RF section, because of the limited RF wavelength: if the centre of the bunch sees the peak RF voltage in the linac, then particles at the head and the tail will see slightly lower RF voltages. Over the entire linac, the positron energy is increased to 5 GeV: the energy spread is then dominated by the "RF curvature", rather than by the initial

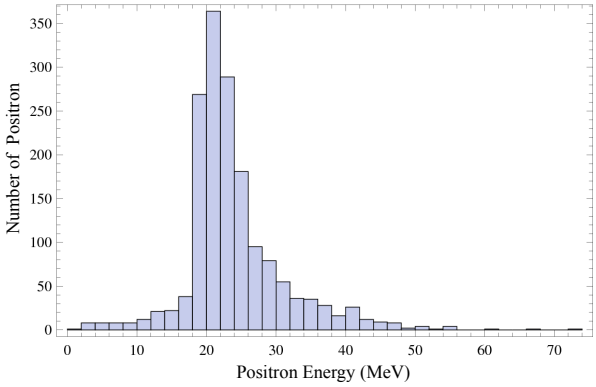

Figure 2.14: Positron energy distribution after capture RF.

energy spread of the positrons. The relative energy spread at the end of the linac depends on the bunch length and the RF frequency. The energy spread is important because the damping ring has a limited energy acceptance: in the ILC this will be about 1%, and in CLIC it will be somewhat larger. For ILC, the RF frequency is about 1.3 GHz, so a particle 5 mm from the centre of the bunch will arrive at the end of the linac with an energy deviation of -1%, relative to the energy of a particle at the centre of the bunch.

Figs. 2.15, 2.16 and 2.17 show the transverse distribution of the positrons at the end of the first RF section. Note that compared to the distribution immediately after the target, there is a large spread in coordinate (about 7.5 mm rms spot size), and a relatively small divergence (less than 0.2 rad, full width). The lattice functions in the RF section are different from those characterising the beam at the exit of the target: in particular, the size of the beta function increases between the target and the capture RF. The purpose of the matching device is to allow this change to happen with minimal beam losses. But because particles with very large amplitudes or angles are lost from the beam in the matching device and RF section, the emittance at the end of the first RF section is smaller than it is at the exit of the target, reducing from 25 mm rad to about 21 mm rad.

Out of the positrons that survive to the end of the first RF section, only about half will be within the damping ring acceptance. After imposing a cut corresponding to the damping ring acceptance, the overall yield from the positron source is about 1.7 positrons per electron per 100 m of undulator. The polarisation rate is about 29%,

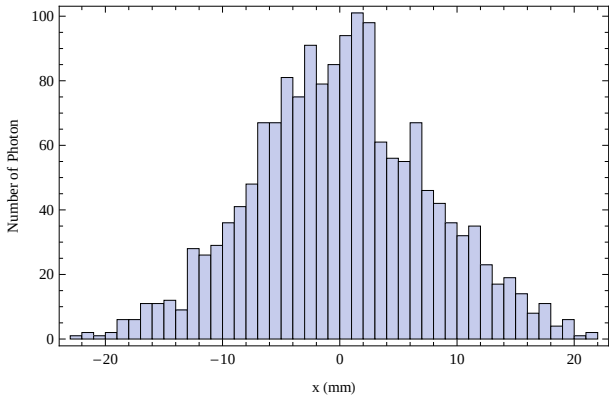

Figure 2.15: After capture RF positron transverse position x distribution.

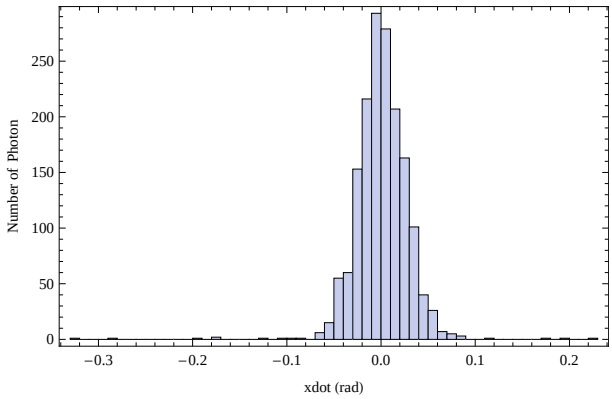

Figure 2.16: After capture RF positron divergent transverse direction angle distribution. xdot is the positron angle in unit of radian

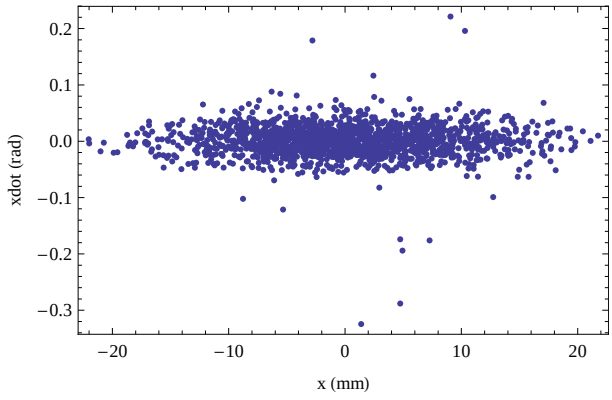

Figure 2.17: Positron transverse phase space distribution after capture RF. xdot is the positron angle in unit of radian

which is larger than the polarisation immediately after the target: the increase is due to the fact that the positrons outside the damping ring acceptance tend to have large betatron amplitudes and poor polarisation. The yield and polarisation are sufficient, but the polarisation in particular can be improved by use of a photon collimator to improve the polarisation of the photons striking the target. This will be discussed further in Chapter 3.

3

Undulator-Based Positron Source for ILC

An undulator-based positron source has long been the choice for the ILC baseline, which is described in the ILC Reference Design Report [20]. An undulator-based positron source has the benefits of producing a beam with emittance smaller than could be obtained from a conventional source achieving the same production rate, whilst limiting thermal load and activation of the production target; and also allows for the possibility of producing a polarised positron beam by using a helical undulator.

In this chapter, we discuss the present design of the ILC baseline positron source [43]. The baseline does not include a photon collimator. However, as discussed previously, a collimator between the undulator and the target provides some protection for components downstream of the undulator, and also allows for some possibility of improving the rate of polarisation, by removing photons that are at large angles with respect to the undulator axis. Photons at large angles tend to have different polarisation than photons that are close to the axis. Although a photon collimator for ILC has been proposed, and different designs considered, a detailed study of the system, including effects such as heat deposition, activation, and effect on polarisation, have not previously been considered.

Table 3.1: ILC helical undulator parameters.

Undulator period	11.5 mm
Field on-axis	0.86 T
Deflection parameter	0.92
Total length	147 m
Electron beam energy	150 GeV
Electron current	9.0 mA
Average photon energy	10.5 MeV
Photon beam power	131 kW

3.1 Helical Undulator

3.1.1 Baseline Undulator Parameters

The present baseline parameters are given in Table 3.1. For the ILC design, a 150 GeV main electron beam from the electron linac will pass through a helical undulator, which is 147 m long with a period of 11.5 mm [44]. The undulator length has been determined assuming that the target is not immersed in the field of the optical matching device (the "flux concentrator"). This avoids the problems of eddy currents [45] generated by the rotation of the target in a magnetic field; however, the capture efficiency of positrons from the target is expected to be lower. The overall yield of the positron source in the baseline design is expected to be 1.5 positrons per electron [46]. Although in principle, a yield of just one positron per electron in the undulator is sufficient; a higher yield is needed in practice because of losses between the positron source and the interaction point.

The magnetic field of the undulator on-axis is about 0.86 T. The electron beam will follow a spiral trajectory along the axis, and emit high energy photons with an average energy of 10.5 MeV. The main electron beam will have 2620 bunches per pulse, and 5 pulses per second. Each bunch contains about 2×10^{10} electrons. When the electron beam goes through a 147 m undulator, it will generate 7.8×10^{16} photons per second. The average integrated power of the photon beam generated by the ILC undulator is about 131 kW.

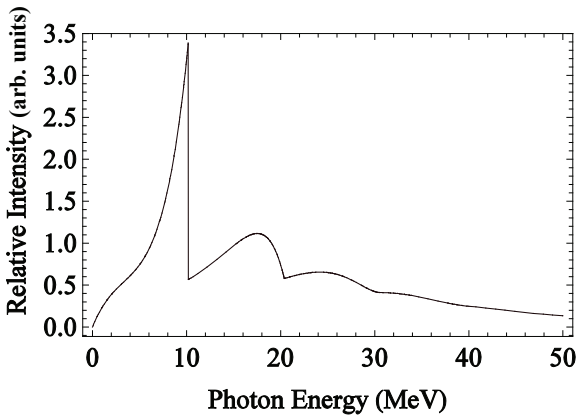

Figure 3.1: Radiation beam power spectrum from the ILC baseline helical undulator.

3.1.2 Radiation Power Spectrum and Distribution

The power spectrum and angular distribution of the radiation from the undulator are important characteristics [47]. Ideally, there will be a single narrow spike in the power spectrum at a frequency corresponding to photon energy significantly above the pair production threshold. This would lead to efficient production of positrons, with a relatively narrow energy spread. Fig. 3.1 shows the radiation power spectrum from the ILC undulator. There is indeed a sharp peak at an energy significantly above the pair production threshold; however, there is significant power at energies above and below the peak. Since there is a strong correlation between photon energy and angle (within a given harmonic, higher angle photons have lower energy), it is possible that a photon collimator will have some effect on the spectrum.

The angular distribution is important for the photon collimator, and also for understanding the power density on the target. Since the polarisation and photon energy are correlated with the angle, optimising the aperture of the collimator could help to improve the polarisation and reduce the power load on the target, while maintaining the total positron yield at a good level. Fig. 3.2 shows the angular distribution of radiation power from the ILC undulator, with the parameters shown in Table 3.1. The impact of the photon collimator will be considered in Section 3.2 below.

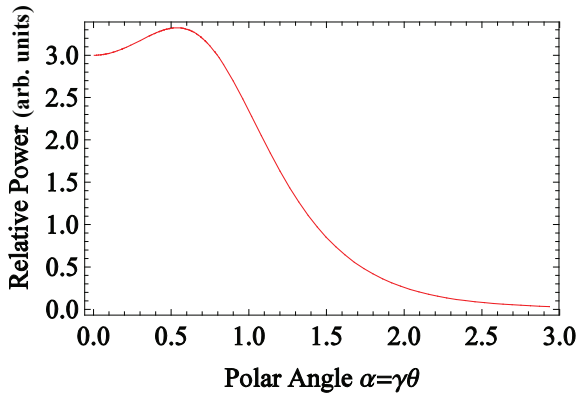

Figure 3.2: Radiation power distribution as a function of angle with the undulator axis.

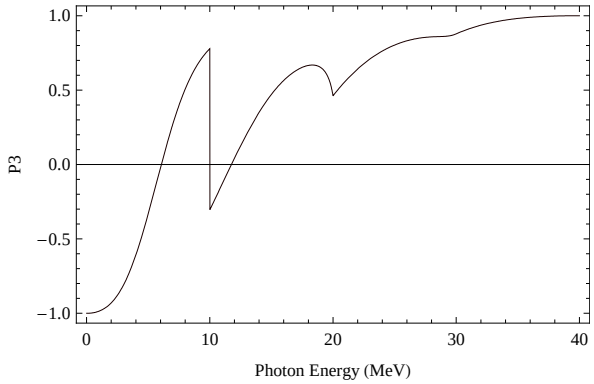

Figure 3.3: ILC undulator generated photon beam polarisation.

3.1.3 Photon Beam Polarisation

The degree of polarisation of the positron beam produced by the source depends on the degree of polarisation of the photon beam hitting the target. Fig. 3.3 shows the polarisation as a function of photon energy, for the beam produced by the ILC undulator using the baseline parameters [20].

3.2 Photon Collimator

In chapter 2 we introduced the functions of the photon collimator. For the ILC, although different designs [48] have been produced based on general principles, detailed

studies have not previously been carried out. In this section, we will review two different collimator designs, and present results from simulations of the energy deposition, thermal loading and activation. We shall also consider the impact of collimation on the polarisation of the photon beam.

3.2.1 Photon Collimator Designs

We shall discuss two different designs for a photon collimator for ILC, which we shall refer to as Model 1 and Model 2. Photon collimator Model 1 [49] is shown in Fig. 3.4. The collimator has a cylindrical geometry, and consists of an inner spoiler, and an outer absorber. The collimator is 90 cm long and has a radius of 6 cm. Copper is used as an absorber (inner radius 2 cm and outer radius 6 cm): the choice of copper is based on its high thermal conductivity ($\sim$401 W/m/K) and high melting point ($\sim$1357.77 K). The spoiler needs a high Z material, but not too high since such materials typically have poor thermal conductivities. In the case of Model 1, the spoiler material is titanium. Again, its high melting point ($\sim$1941 K) makes it a suitable candidate to survive the temperature increases generated by the impact of one or more bunches. The special feature of the Model 1 design is that the spoiler is separated into different cylindrical fragments with an axial hole of $\sim$4 mm; the aperture can be adjusted in the design to optimise the performance of the collimator.

Model 2 [50] consists of a graphite spoiler and tungsten absorber, in thermal contact with an enclosing cylinder of copper, as shown in Fig. 3.5. The reason for choosing these materials is again based on their thermal conductivity and melting points. The spoiler needs to be made from a material that can enhance the shower without absorbing too much energy. A good material for the absorber will absorb the shower and have relatively good conductivity to allow efficient cooling. The length of the Model 2 collimator is about 18 cm and the outer radius is 4 cm. The inner radius of both collimators can be chosen to optimise the properties of the photon beam.

Both collimators, Model 1 and Model 2 are based on the same principle: the halo of the beam will be scraped by the spoiler, then there will be some secondary particles generated, which will be stopped and absorbed by absorber. Both models can, in principle, be optimised (for example, by adjusting the aperture) for the desired properties of the photon beam. However, because of the different geometries and materials used in each model, we can expect to see some differences in terms of temperature rise, activa-

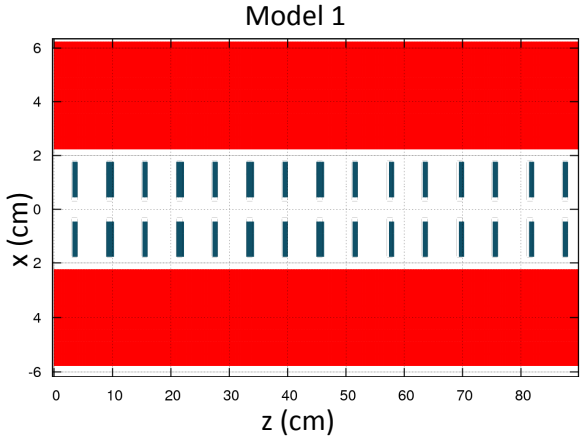

Figure 3.4: Photon collimator Model 1.

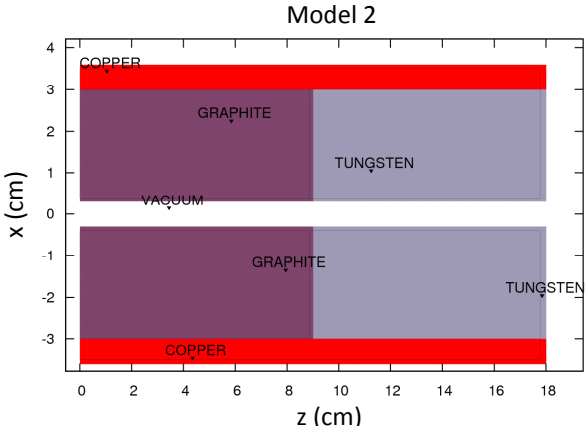

Figure 3.5: Photon collimator Model 2.

tion, and flux of secondary particles that escape from the collimator towards the target station. In the remaining parts of this section, we present the results of simulations aimed at evaluating the performance of the two models.

3.2.2 Collimator Effect on Photon Beam

One of the motivations for using a photon collimator before the target is to scrape the photon beam to help limit the extraneous halo. At the same time, since the polarisation of photons in the beam depends on the angle of the photons with respect to the undulator axis, the collimator may also, in principle, be used to control the polarisation. Of course, a smaller collimation aperture gives a higher degree of polarization, but will also limit the intensity of the photon beam. We have to compromise between polarisation and quantity of positrons. The photon collimator provides the means to adjust the balance between polarisation and beam intensity [51].

In order to understand the relationship between the polarisation and the photon beam intensity, we need to implement the photon beam spectrum in a simulation code [52]. This will enable us to investiagte how the overall positron source system performance changes as the photon collimator aperture varies. We can also implement the relevant formulae into Mathematica to get analytical results, if we make certain approximations. For example, in calculating the number of photons and the polarisation, we can simply cut all photons with an angle larger than a certain value, corresponding to the aperture of the collimator. If the distance of the collimator from the undulator is large compared with its length, this should be a good approximation. However, a simulation allows us to use a more accurate model. Comparing the simulation and the analytical results will provide a cross-check, and also indicate the validity of the approximations in the analytical calculations.

The variation of transmitted intensity and polarisation with spoiler aperture are shown in Fig. 3.6. Note that this figure shows the results of an analytical calculation using the formulae presented in Chapter 2, together with the results of a simulation using FLUKA; the analytical results and the simulation results are in good agreement. There is no significant difference between Model 1 and Model 2 in their effect on the photon transmission and polarisation [53] as a function of aperture.

The choice of aperture depends on the relative weight given to the polarisation and the intensity. Although a high polarisation can be achieved by collimating to very small

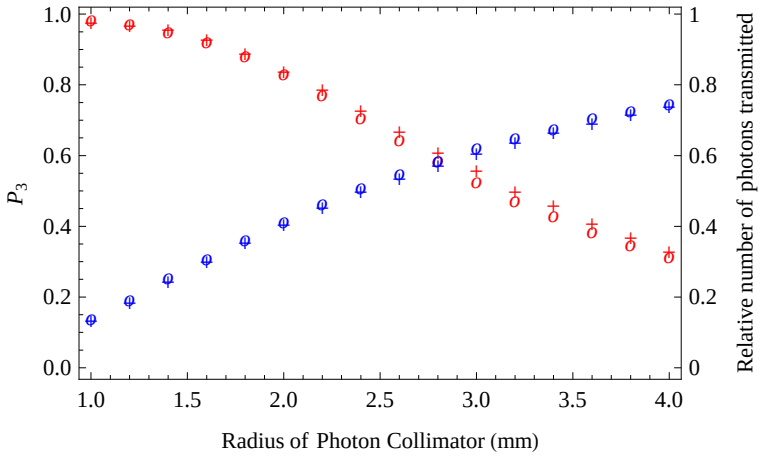

Figure 3.6: Polarisation (red) and number of photons transmitted (blue) as a function of collimator aperture. The number of photons transmitted is normalised to the uncollimated beam. Analytical results (circles) are compared with Fluka simulation (crosses).

angles, the drop in photon intensity could make it difficult to meet the specifications for positron intensity. More detailed studies are required to determine the optimum balance between intensity and polarisation (which will depend on the physics studies to be performed). Also, processes in the target and optical matching device will lead to the positron beam having a lower polarisation than the photon beam. A full simulation, including the target and optical matching device is needed in order to determine the optimum aperture for the photon collimator.

The analytical calculations allow us to study in more detail the effect of the photon collimator on the power spectrum and polarisation. As an example, let us choose a collimator aperture of 2.8 mm. This gives a photon transmission (in terms of number of photons, relative to the uncollimated beam) of about 60%, and a polarisation of just less than 60%. In this case, the power spectrum is shown in Fig. 3.7, and the polarisation spectrum is shown in Fig. 3.8. The sharp cuts as a function of frequency are a consequence of the strong correlation between frequency and the angle of the radiation. Overall, the radiation power is reduced by about 27%. The polarisation is improved, because the radiation at large angles, which has a different polarisation to the radiation close to the axis, is removed.

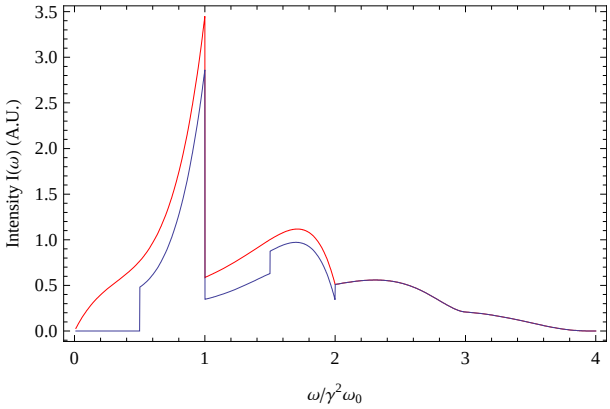

Figure 3.7: Intensity of radiation from the ILC helical undulator, as a function of normalised frequency. Red: uncollimated. Blue: collimated.

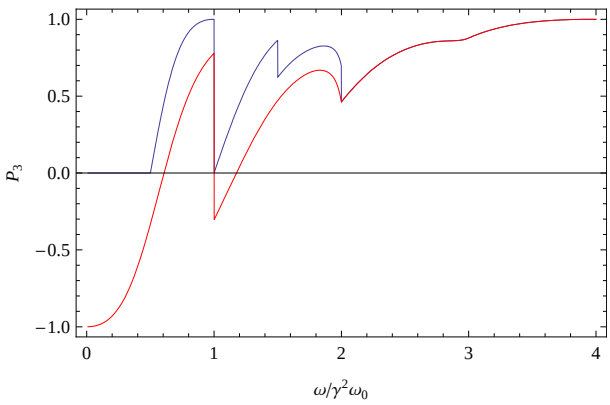

Figure 3.8: Polarisation of radiation from the ILC helical undulator, as a function of normalised frequency. Red: uncollimated. Blue: collimated.

3.2.3 Collimator Effect on Positron Production

Understanding the spectrum and polarisation of the radiation from the undulator is an intermediate step towards understanding the properties of the positron beam. We now turn our attention to the effect of the collimator on the production of positrons. Here, the two main issues are the intensity and the polarisation. Reducing the collimator aperture can improve the polarisation, but at the cost of reducing the intensity. However, a reduction in positron intensity resulting from collimation of the photon beam can, in principle, be compensated by increasing the length of the undulator. In practice, this is not desirable, because of the increase in costs, and potential impact of the undulator on the electron beam.

To understand the effect of the collimator on the positron production, we perform a simulation using several different codes. First, we compute the properties of the photon beam striking the target. This can be done using FLUKA, or using an analytical calculation (the results are very similar). The propagation of the photons through the target and production of electron-positron pairs is carried out using Geant4. Then, positrons are tracked through the optical matching device using SAMM. At this point, the positron beam is at the entrance to the capture RF. We do not model this system in detail; however, we expect some positrons to be lost between the capture RF and the damping ring, mainly because of limitations in the damping ring acceptance. Therefore, we apply a cut to the positron distribution at the exit of the optical matching device, representing the damping ring acceptance. We can estimate the intensity, phase space distribution, and polarisation of the positron beam from the positrons in the model, after applying the cut for the damping ring acceptance.

Since we wish to focus at this stage on the photon collimator, we assume nominal parameters for the other components. This includes the undulator, whose parameters are given in Table 3.1, the target, and the optical matching device. The target is titanium alloy (Ti-6%Al-4%V), with a thickness of 0.4 radiation lengths. The optical matching device is a tapered solenoid (adiabatic matching device) with initial field strength 6 T, final field strength 0.5 T, and taper parameter $30\,\mathrm{m}^{-1}$.

We repeat the simulations for a range of apertures of the photon collimator, from 1 mm to 4 mm. Some of the key results are shown in Table 3.2. The effect of 1 mm aperture collimation on the positron energy distribution is shown in Fig. 3.9, and on the

Table 3.2: Effect of collimation on photon and positron beams, with fixed undulator, target and matching device parameters. Note that the positron yield is defined as the number of positrons produced per electron in the undulator.

Collimator aperture	No collimation	4 mm	2 mm	1 mm
Average photon energy	10.5 MeV	13.5 MeV	15.0 MeV	12.3 MeV
Photon polarisation	29%	28%	51%	66%
Positron yield	1.50	1.51	1.05	0.26
Positron emittance	0.75 mm rad	0.68 mm rad	0.59 mm rad	0.53 mm rad
Positron polarisation	27%	32%	47%	67%

polarisation distribution in Fig. 3.10. Note that the positron energy distribution peaks at about 5 MeV in both cases (without collimation, and with 1 mm collimation). This is a consequence of the fact that the peak in the photon energy spectrum occurs at about 10 MeV, and this energy is shared equally between the electrons and the positrons in pair production.

After the positron energy and polarisation results, we present the transverse distribution of the positron beam after the target. Fig. 3.11 shows the distribution as a function of horizontal position. When the photon collimator is applied, the positron beam spot size is reduced from 2 mm rms (without photon collimator) to 1.4 mm rms (with collimator). Fig. 3.12 shows the distribution of angles of the positron trajectories. The collimator reduces the angular range; but even with 1 mm collimator aperture, positrons will be emitted in a range of angles of $\pm 60°$.

The damping ring has a limited acceptance in transverse and longitudinal phase space. The transverse acceptance is specified in terms of the maximum normalised betatron amplitude of a particle that remains in the ring for at least one damping time following injection. The normalised (horizontal) betatron amplitude is given by $2\gamma J_x$, where γ is the relativistic factor, and J_x is the horizontal action:

$$2J_x = \gamma_x x^2 + 2\alpha_x x p_x + \beta_x p_x^2, \tag{3.1}$$

where α_x, β_x and γ_x are the Twiss parameters. The normalised betatron action of a particle is conserved under transport and acceleration in a beam line, neglecting radiation, space charge and wake field effects. The range of transverse amplitudes of

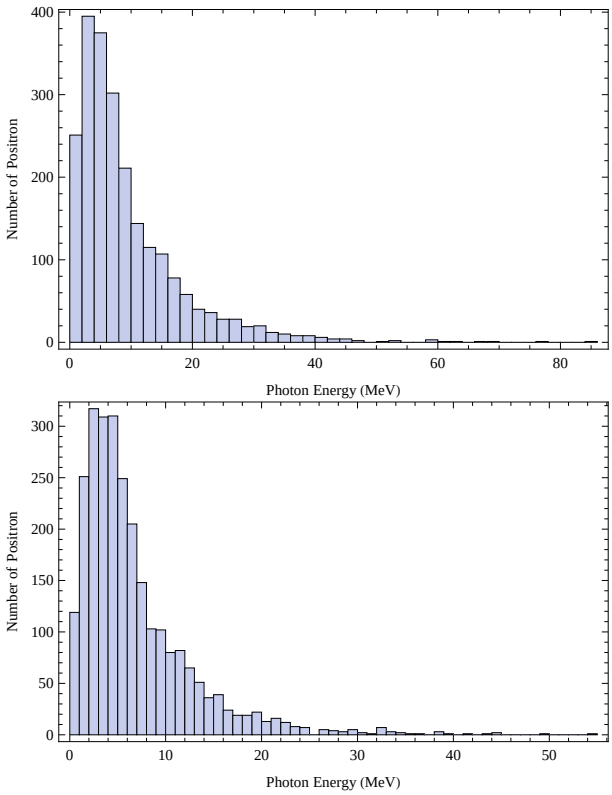

Figure 3.9: Positron energy distribution after target. Top: no photon collimation. Bottom: 1 mm radius photon collimation.

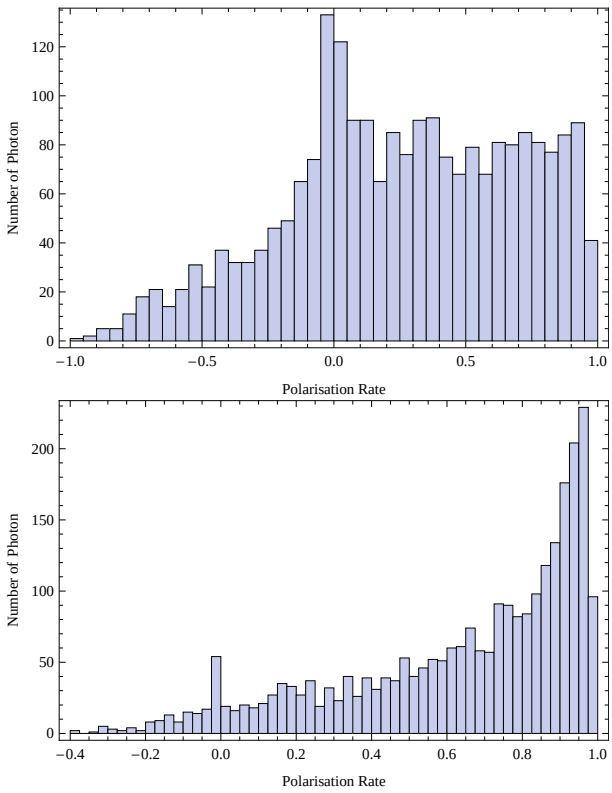

Figure 3.10: Positron polarisation distribution after target. Top: no photon collimation. Bottom: 1 mm radius photon collimation.

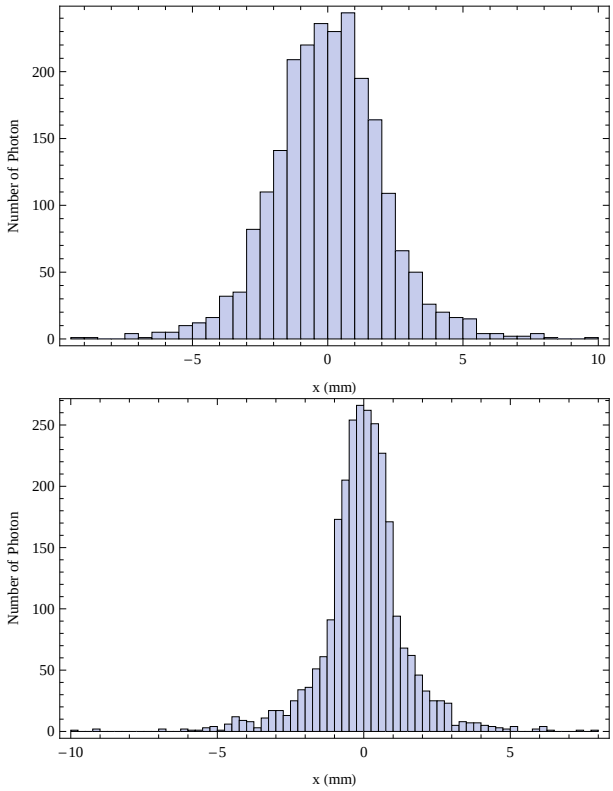

Figure 3.11: Positron distribution as a function of horizontal position. Top: no photon collimation. Bottom: 1 mm radius photon collimation.

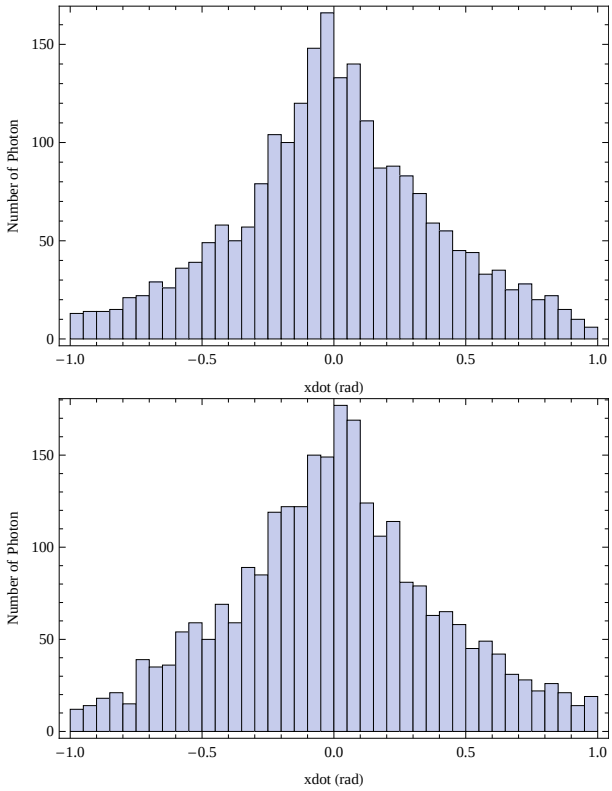

Figure 3.12: Positron distribution as a function of angle with respect to the undulator axis. Top: no photon collimation. Bottom: 1 mm radius photon collimation.

particles in a beam is measured by the emittance, ε_x:

$$\varepsilon_x = \langle J_x \rangle. \tag{3.2}$$

In the absence of coupling between planes, the emittance can be calculated by:

$$\varepsilon_x = \sqrt{\langle x^2 \rangle \langle p_x^2 \rangle - \langle x p_x \rangle^2}. \tag{3.3}$$

Then, the Twiss parameters are related to the beam distribution by the following relations:

$$\langle x^2 \rangle = \beta_x \varepsilon_x, \tag{3.4}$$

$$\langle x p_x \rangle = -\alpha_x \varepsilon_x, \tag{3.5}$$

$$\langle p_x^2 \rangle = \gamma_x \varepsilon_x. \tag{3.6}$$

Since the normalised betatron amplitude is conserved under linear transport and acceleration, the damping ring transverse acceptance can be applied by removing from the beam any particle with a normalised betatron amplitude larger than a specified acceptance value. For the ILC damping rings, the specified acceptance is 90 mm rad.

Fig. 3.13 shows the horizontal phase space distribution of the positrons after the target. In the case of no collimation, the emittance is 0.75 mm rad. Taking $\gamma \approx 10$, the normalised emittance is approximately 7.5 mm rad; since $\gamma\varepsilon_x = \langle \gamma J_x \rangle$, the number of positrons with betatron amplitude larger than the damping ring transverse acceptance of 90 mm rad is quite small. Therefore, we do not expect the damping ring transverse acceptance to have a significant effect on the positron yield, even without a photon collimator. If a photon collimator with aperture 1 mm is used, the normalised emittance is reduced to about 0.53 mm rad. The percentage of positrons surviving the damping ring transverse acceptance may be a little higher, but the difference is not likely to be very significant in terms of the yield.

The damping ring longitudinal acceptance is specified in terms of the energy spread and bunch length. Particles within $\pm 1\%$ of the nominal injection energy, and ± 5 mm of the nominal injection longitudinal position will be within the acceptance of the damping ring. Because of the large energy spread on the positron beam, it is likely that more particles will be lost because of the longitudinal acceptance limitations of the damping ring, than because of the transverse acceptance limitations. However, here it is unlikely

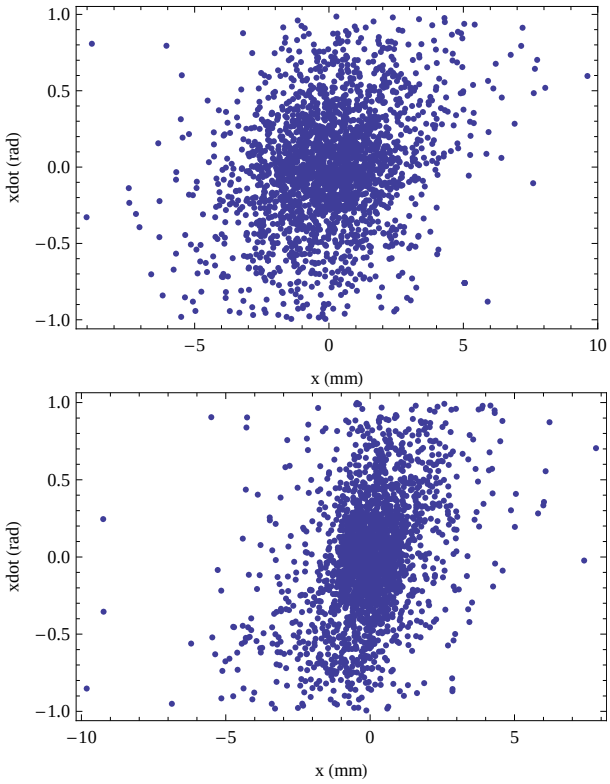

Figure 3.13: Positron phase space distribution after the target. Top: no photon collimation. Bottom: 1 mm radius photon collimation.

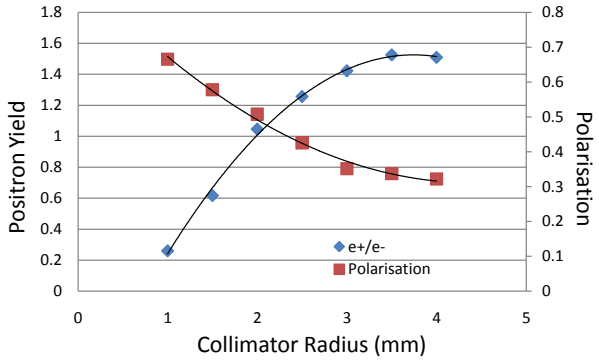

Figure 3.14: Positron yield (blue curve, left axis) and polarization (red curve, right axis) as functions of collimator aperture.

that the photon collimator will make much difference, because its main effect on the positron distribution is in the transverse planes.

In fact, taking into account both the transverse and longitudinal acceptance of the damping ring, the fraction of positrons within the damping ring acceptance is only 3% lower with a 1 mm photon collimator, compared to the case without any photon collimation.

Finally, Fig. 3.14 shows the positron yield and polarisation as functions of the collimator aperture. We see that although it is possible to achieve a very good level of polarisation (more than 65%), this requires very hard collimation, using a photon collimator aperture of 1 mm. This will reduce the positron intensity by a significant amount. To restore the yield to 1 positron per electron, an undulator length of 500 m would be required, which is much longer than desirable. A collimator aperture of around 1.7 mm would give a yield of around 1.5 positrons per electron, and a polarisation of about 55%. This may be a good compromise.

3.2.4 Energy Deposition in the Photon Collimator

When high energy photons pass through a material, ionization losses in the photon collimator will result in energy deposition and temperature rise. Secondary particles produced in the electromagnetic processes are mainly positrons, electrons and photons. These particles again lose energy on their way through the material via collision and radiation processes. The collisions account for the majority of heat deposition in the material, while photons are generated by radiation processes. The cascade shower

Table 3.3: Transfer efficiency, photon polarisation and energy deposition in different sections of the two collimator models, for different collimator apertures. The percentage in brackets following the total energy deposited gives the total energy deposited in the collimator as a percentage of the total energy in the incident photon beam.

R_{col} (mm)	Transfer efficiency (%)	Polarisation (%)	Deposited energy (MeV/primary photon)						
			Model 1			Model 2			
			Ti	Cu	Total	C	W	Cu	Total
2	41	84	1.87	2.30	4.17 (35%)	1.03	3.88	0.04	4.95 (41%)
3	61	56	0.78	0.85	1.63 (14%)	0.48	1.37	0.02	1.87 (16%)
4	74	33	0.31	0.30	0.61 (5%)	0.21	0.45	0.01	0.68 (6%)

develops through repeated similar interactions. As the shower develops, the number of cascade particles will increase exponentially (so the mean energy will decrease) until the energy of the shower particles is low enough to stop further multiplication. From this point the shower decays slowly through ionization losses for electrons, or by Compton scattering and photoelectric effect for photons. Although the collimator will remove only part of the photon beam, the rate of energy deposition could be more than 30 kW; a proper understanding of thermal effects will be important to validate and optimize the design of the collimator. The ILC will operate with pulses of 1 ms duration, and a pulse repetition rate of 5 Hz. Therefore, the temperature rise during a pulse will be essentially determined by the energy deposited during a pulse, while the actual temperature reached will depend on the cooling between pulses.

We have performed simulations using FLUKA to compare the energy deposition in the two different models proposed for the ILC photon collimator. The FLUKA simulations give the energy deposited in the material by the particles, which are then transformed into a temperature using the specific heat capacity of the material. The thermal behaviour of the collimator depends upon the photon beam intensity, and repetition rate of the ILC as well as the physical properties of the material. Figs. 3.15 and 3.16 show visualisations of the energy deposited in Model 1 and Model 2.

It is clear that for Model 1 most of the energy (red region in Fig. 3.15) is deposited in the spoiler and the edge of the absorber. This is a potential problem, since the spoiler is supposed to create a cascade shower, with most of the energy being absorbed by the absorber: the spoiler is intended only to absorb a relative small amount of energy. Whereas in our simulation, the energy deposited in the spoiler is nearly equal

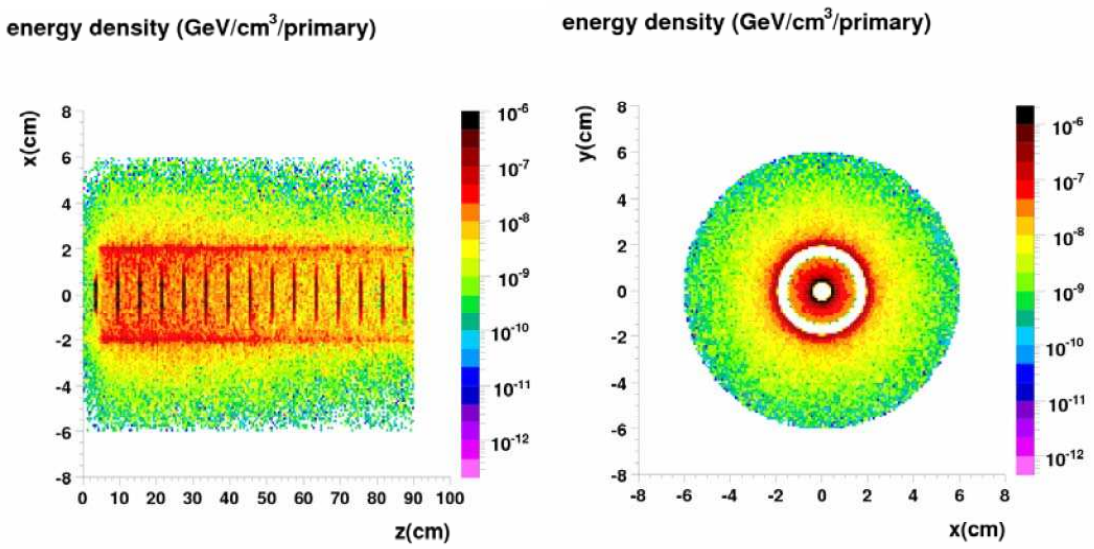

Figure 3.15: FLUKAGUI visualisation showing the energy deposititon per unit volume per primary photon in the Model 1 collimator, using a 10 MeV incident photon beam. The plot has been projected onto the $x - z$ plane (left) and $x - y$ plane (right), where z is the direction of the incident photons.

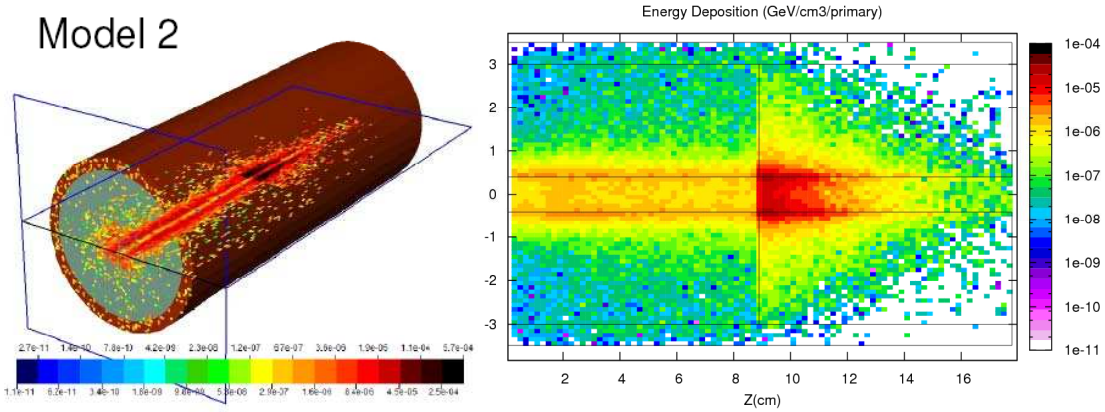

Figure 3.16: FLUKAGUI visualisation showing the energy deposititon per unit volume per primary photon in the Model 2 collimator, using a 10 MeV incident photon beam.

to the energy deposited in the absorber. In Model 2, the front section of the collimator enhances the shower; part of the energy is distributed roughly evenly through the front spoiler section; then, more of the energy will be absorbed by the following absorber section. We can see from Fig. 3.16 that by the end of the collimator, the secondary particles die out, and the absorber performs its function to take most of the energy.

Table 3.3 shows the transfer efficiency, photon polarisation and energy deposition in different sections of the two collimator models, for different collimator apertures. The overall transfer rate of the radiation increases as a function of aperture radius from 41% at 2 mm, to 74% at 4 mm; and at the same time the photon polarisation falls from 84% to 33%. As already mentioned, it is necessary to make a compromise between the intensity of the photon beam and its polarisation. From the results of the FLUKA simulation, the transfer efficiency and polarisation are quite similar in both models: the difference between them is less than 1%, which is negligible.

In Model 1, with an aperture of 2 mm, the total energy deposition for each primary photon is 4.17 MeV, which is about 34.7% of the total energy. Of the energy deposited, 1.87 MeV is in the titanium spoiler section and 2.3 MeV is in the copper absorber section. When the aperture gets larger, fewer photons will be collimated, so there will be less energy deposited. For example, when the radius is increased to 3 mm, the energy deposition will fall to 1.63 MeV, which is about 13.6% of the total energy. The energy deposited in the spoiler and in the absorber start to become very similar, with values of 0.78 MeV and 0.85 MeV respectively. The change becomes clearer with aperture 4 mm. Only 5.1% (0.61 MeV) of the total energy is deposited, but now the energy in the spoiler and the absorber are 0.31 MeV and 0.30 MeV, respectively. Although the energy deposited in the absorber increases more rapidly than the energy deposited in the spoiler as the aperture is reduced, the energy deposited in the spoiler is still high. The geometry of the collimator will make it difficult to provide sufficient cooling for the spoiler, which is likely to reach very high temperatures during operation.

Model 2 is a more compact design than Model 1; however, the collimation efficiencies are quite similar for both designs. The difference between the two appears in the energy deposition. First of all, we can see from Table 3.3 that the spoiler carries much less energy than the absorber, and that the particles are distributed in the spoiler more evenly than in Model 1. The absorber works well for absorbing the energy, although the front part of absorber will see a greater energy deposition from the cascade shower.

We also see that compared with Model 1, there is a greater total energy deposited in Model 2 for each different aperture. Furthermore, the amount of energy deposited in the absorber is more than twice the energy deposited in the spoiler (more than three times, for aperture 2 mm). This suggests that it should be easier to provide cooling for Model 2 than for Model 1, to keep the different parts of the collimator at reasonable temperatures.

3.2.5 Temperature Rise and Cooling Methods

As already mentioned, although the photon collimator will intercept only part of the beam, the power load could be as much as 30 kW. The ILC will operate with pulses of 1 ms, pulsed at 5 Hz. The temperature reached by the collimator will depend on the balance between the energy deposited by the photon beam, and the amount of cooling provided.

In the simplest case, cooling could be purely by thermal radiation. However, this is most effective only at very high temperatures: by Stefan's Law, the total power radiated per unit surface area varies as the fourth power of the absolute temperature.

Fig. 3.17 shows the temperature rise in the spoilers and absorbers in collimator Model 1 following a single machine pulse. Also shown, for comparison, is the fraction of photons transmitted. The temperature rise is calculated from the energy deposition obtained from the FLUKA simulations, and the heat capacity of the material. We assume that the absorbed energy is evenly distributed throughout the material. For Model 1, it is actually the spoilers, rather than the absorber, that experience the greatest temperature rise. With a small aperture of 1 mm, the temperature rise in the spoilers is 80 K per machine pulse. The temperature rise in the absorber is small by comparison, because the heat capacity of the absorber is much larger than the heat capacity of the spoilers. Even with a more realistic aperture of 2 mm, the temperature rise would be more than 40 K per machine pulse (every 200 ms). Cooling the spoilers will be a significant issue for Model 1.

Fig. 3.18 shows similar information to that shown in Fig. 3.17, but for collimator Model 2. Here, we see somewhat different behaviour than for Model 1. The transfer rate is the same for both models; however, the temperature rise for a given aperture is smaller in Model 2 than in Model 1, and the temperature rise in the absorber is more comparable to the temperature rise in the spoiler. In Model 2, with an aperture of

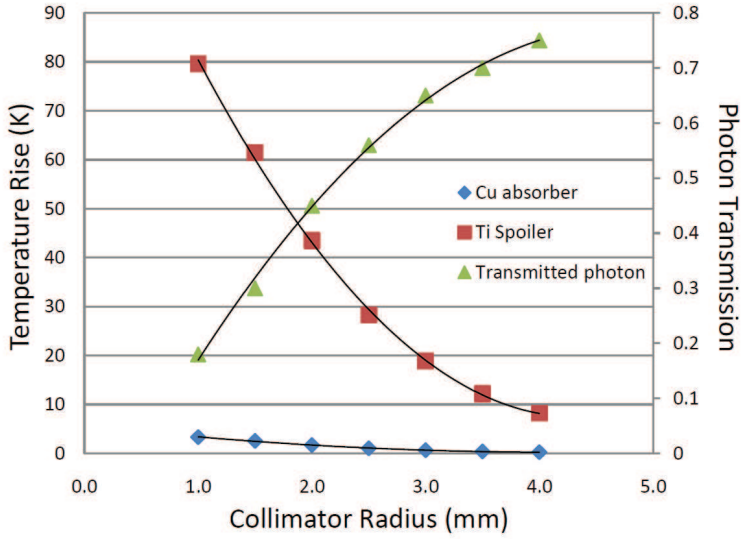

Figure 3.17: Temperature rise in spoilers and absorbers as a function of collimator aperture in Model 1. Also shown is the fraction of primary photons transmitted.

1 mm, the temperature rise would be 32 K; this falls to 15 K for an aperture of 2 mm. Also, the mechanical design of the collimator should make it easier to provide additional (convective and conductive) cooling.

3.2.6 Activation of Photon Collimator

Photons striking the collimator will lead to nuclear activation [54]. To estimate the magnitude of the activation, we calculate the equivalent dose rate and activation immediately after an operational period of 180 days. The equivalent dose rates for various photon collimator apertures for the two models are shown in Fig. 3.19. Fig. 3.20 shows the distribution of residual particles from each of the models, with an aperture of radius 3 mm, calculated using FLUKA [55]. Fig. 3.21 shows the spoiler activation in Model 1, with various collimator apertures and different cooling times. Fig. 3.22 shows the activation of the graphite and the tungsten in Model 2. We assume a photon beam intensity of 8×10^{16} photons/second.

In both models, the equivalent dose rate can reach 10^9 pSv. After one day of cooling, the dose rate falls by an order of magnitude for Model 1. For Model 2, which uses graphite and tungsten for the spoiler and absorber material (rather than titanium used for the spoiler material in Model 1) the dose rate falls much more quickly. However,

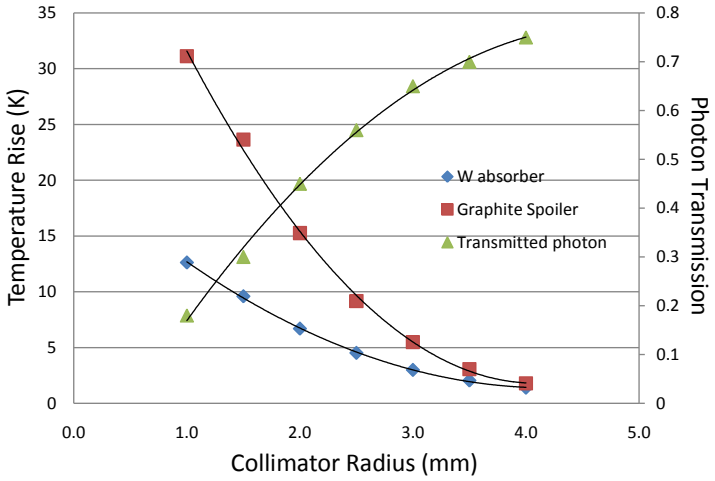

Figure 3.18: Temperature rise in spoilers and absorbers as a function of collimator aperture in Model 2. Also shown is the fraction of primary photons transmitted.

Table 3.4: Power (in watts) of secondary particles emitted from the photon collimator.

aperture	Model 1		Model 2	
(mm)	e^-	e^+	e^-	e^+
1	1090	790	120	77.6
2	582	311	83.3	43.3
3	189	86.9	63.5	9.93
4	44.7	11.3	32.2	2.11

the working environment beside the collimator will be an issue because of its proximity to the target: the photon collimator will be part of the remote-handling system.

3.2.7 Secondary Particles

Photons striking the collimator can generate secondary particles, which may reach the target station. The number of secondaries striking the target station is not expected to be very large. Table 3.4 shows the power of secondary electrons and positrons from the photon collimator, for different collimator apertures.

We see that Model 2 has significantly lower power of secondary particles; this is because tungsten is a more effective absorber. For a collimator radius of around 2 mm (giving a positron yield of more than 1.5), a secondary particle power of a few hundreds

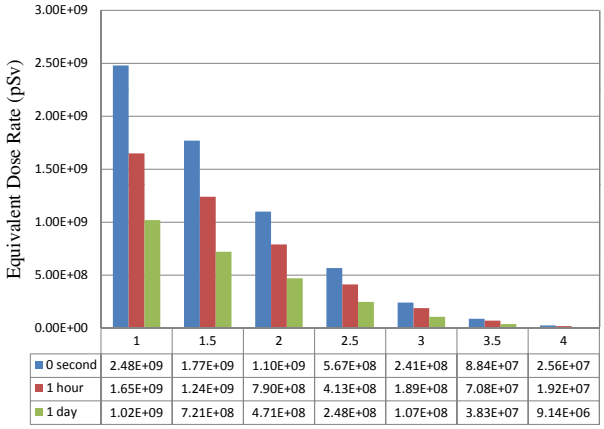

	1	1.5	2	2.5	3	3.5	4
0 second	2.48E+09	1.77E+09	1.10E+09	5.67E+08	2.41E+08	8.84E+07	2.56E+07
1 hour	1.65E+09	1.24E+09	7.90E+08	4.13E+08	1.89E+08	7.08E+07	1.92E+07
1 day	1.02E+09	7.21E+08	4.71E+08	2.48E+08	1.07E+08	3.83E+07	9.14E+06

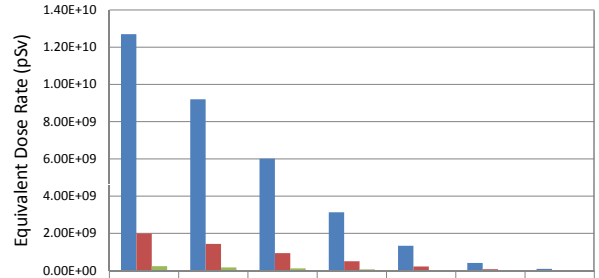

	1	1.5	2	2.5	3	3.5	4
0 seconds	1.27E+10	9.20E+09	6.01E+09	3.13E+09	1.33E+09	4.10E+08	9.20E+07
1 hour	1.99E+09	1.43E+09	9.37E+08	5.02E+08	2.19E+08	7.24E+07	1.92E+07
1 day	2.36E+08	1.65E+08	1.17E+08	6.17E+07	2.53E+07	1.05E+07	3.64E+06

Figure 3.19: Equivalent dose rate for Model 1 (top) and Model 2 (bottom) when applying various photon collimator apertures after operating for 180 days. The equivalent dose rates are shown immediately after operation (blue), after one hour of cooling (red) and after one day of cooling (green).

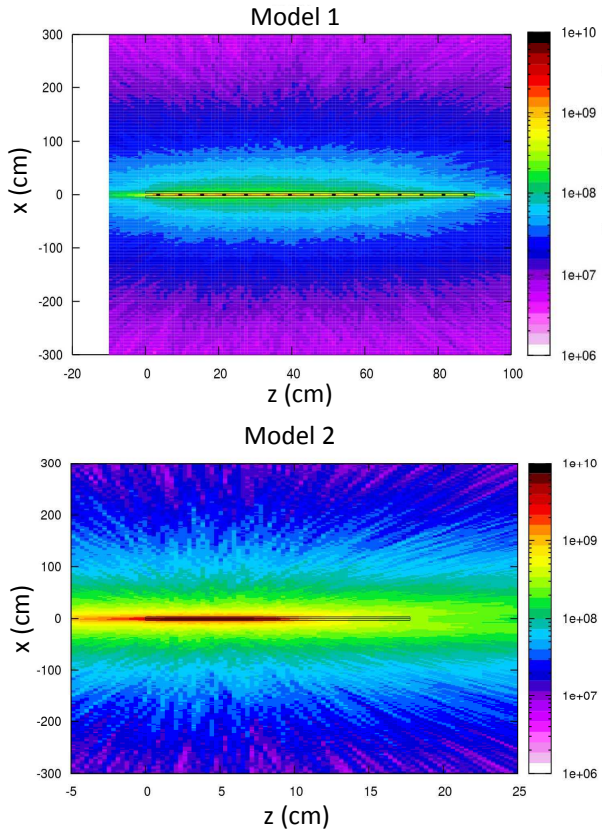

Figure 3.20: Residual particle distribution in Model 1 (top) and Model 2 (bottom) with 3 mm aperture, following an operational period of 180 days.

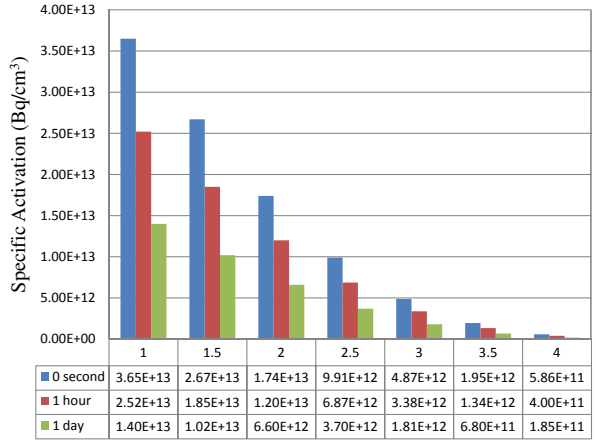

	1	1.5	2	2.5	3	3.5	4
0 second	3.65E+13	2.67E+13	1.74E+13	9.91E+12	4.87E+12	1.95E+12	5.86E+11
1 hour	2.52E+13	1.85E+13	1.20E+13	6.87E+12	3.38E+12	1.34E+12	4.00E+11
1 day	1.40E+13	1.02E+13	6.60E+12	3.70E+12	1.81E+12	6.80E+11	1.85E+11

Figure 3.21: Spoiler activation in Model 1 collimator, following an operational period of 180 days. The spoiler activation is shown immediately after operation (blue), after one hour of cooling (red) and after one day of cooling (green).

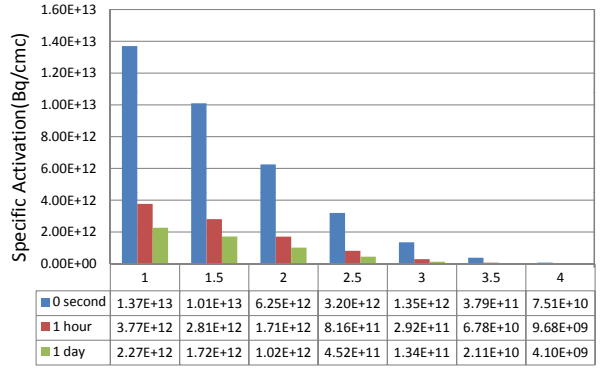

	1	1.5	2	2.5	3	3.5	4
0 second	1.37E+13	1.01E+13	6.25E+12	3.20E+12	1.35E+12	3.79E+11	7.51E+10
1 hour	3.77E+12	2.81E+12	1.71E+12	8.16E+11	2.92E+11	6.78E+10	9.68E+09
1 day	2.27E+12	1.72E+12	1.02E+12	4.52E+11	1.34E+11	2.11E+10	4.10E+09

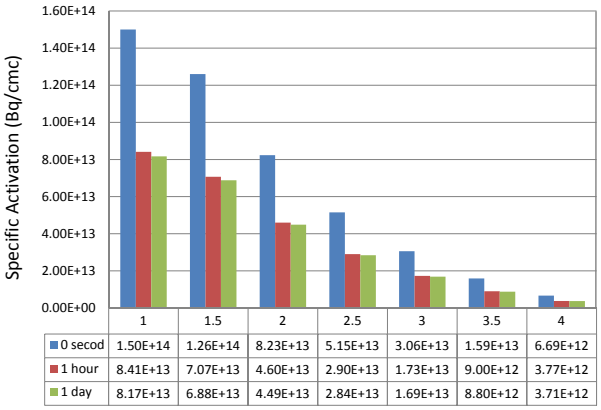

	1	1.5	2	2.5	3	3.5	4
0 secod	1.50E+14	1.26E+14	8.23E+13	5.15E+13	3.06E+13	1.59E+13	6.69E+12
1 hour	8.41E+13	7.07E+13	4.60E+13	2.90E+13	1.73E+13	9.00E+12	3.77E+12
1 day	8.17E+13	6.88E+13	4.49E+13	2.84E+13	1.69E+13	8.80E+12	3.71E+12

Figure 3.22: Model 2 activation in the graphite spoiler (top) and tungsten absorber (bottom) with various photon collimator apertures after operating for 180 days. The activation is shown immediately after operation (blue), after one hour of cooling (red) and after one day of cooling (green).

of watts will be expected for model 1, and less than 100 W for Model 2.

3.2.8 Photon Collimator: Conclusions

We have considered two proposed designs for a photon collimator for the ILC positron source. The analytical calculations of the impact of the photon collimators on the undulator radiation intensity and polarisation show good agreement with FLUKA simulations. Our results show how the intensity and polarisation of the transmitted photon beam depend on the aperture of the collimator. Without collimation, the positron polarization will be around 30%. A high degree of polarisation is possible in principle, but at the cost of a significant drop in intensity (for a fixed length of undulator). A positron polarisation of more than 50% looks achievable with a positron yield of greater than 1.5. This would require collimation of the photon beam with an aperture of around 1.7 mm. Although a positron polarisation of 70% is possible in principle (with collimator aperture of 1 mm), the positron yield would be too low for efficient operation of the ILC, without significantly increasing the length of the undulator. The results for the polarisation and yield are effectively the same for the two collimator designs we have considered. Heating from energy deposition in the collimator is a concern. If there is a reliance solely on radiative cooling, both collimator designs would reach a temperature that is above the melting point of copper. Therefore, the collimator will require additional, convective cooling. Activation is a further concern. The initial results suggest that after one day of cooling (following 180 days of operation), the equivalent dose rate in the vicinity of the collimator will still be significantly high, at least in Model 1. Further study will be needed to understand the activation and its implications more thoroughly. Overall, in comparing the two models, we conclude that Model 2 has a number of advantages over Model 1:

1. Model 2 offers a more compact design.
2. The temperature rise in Model 2 will be lower than in Model 1 for a given energy deposition.
3. The mechanical design will make it easier to provide convective cooling in Model 2.
4. Model 2 has better secondary particle absorption.

Table 3.5: ILC baseline beam and positron production target parameters.

Electrons per bunch	2×10^{10}
Number of bunches	2625
Bunch spacing	360 ns
Pulse length	1 ms
Repetition rate	5 Hz
Incident power on target	131 kW
Target material	Ti-6%Al-4%V
Target thickness	0.4 radiation lengths ($\approx$ 1.4 cm)
Target power absorption	8% ($\approx$ 10.5 kW)
Incident spot size on target	1.7 mm rms
Target diameter	1 m
Target revolution frequency	2000 rpm

5. Model 2 shows lower activation and equivalent dose rate.

3.3 Production Target

3.3.1 Target Thickness

Following the photon collimator is the positron production target. The parameters of the target in the ILC baseline design are shown in Table 3.5. A beam of high energy photons from the undulator strikes the target, generating electron and positron pairs. The properties of the positron beam coming from the target depend on the target material and thickness. The material must provide a high cross section for pair production, but also needs to have good thermal and mechanical properties, and must be able to survive long periods of intense radiation. The target thickness, as with many other parameters in the positron source, is a compromise between competing requirements.

To illustrate the issues regarding the choice of target thickness, we consider the positron yield and energy deposition, as a function of the target thickness. Other considerations include the mechanical strength, positron distribution (transverse and longitudinal), beam polarisation, and the eddy currents that are generated as the target spins at high speed in the magnetic field of the optical matching device. The polar-

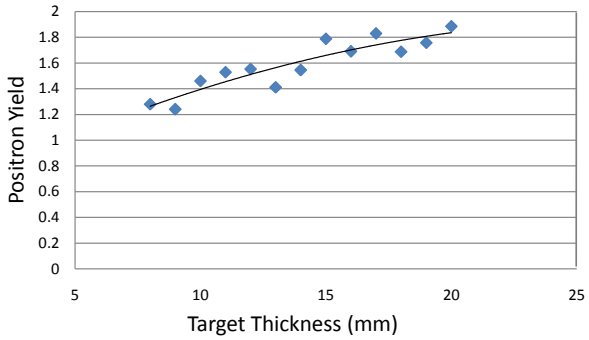

Figure 3.23: Positron yield as a function of target thickness.

isation is not sensitive to the target thickness. Eddy currents will be considered in more detail in Chapter 5. Our aim here is not to perform an optimisation of the target thickness, but to show how the positron yield and energy deposition depend on the thickness. Our results are based on Geant4 simulations. FLUKA does not model the positron polarisation, therefore Geant4 was used for these simulations. Geant4 will model the polarisation of positrons generated by pair production; the simulation does not include changes in positron polarisation from scattering in the target material, however this is expected to be a small effect. We use the ILC baseline parameters for the undulator and the adiabatic matching device. Yield calculations include a cut to represent the damping ring acceptance.

Fig. 3.23 shows how the positron yield varies as a function of target thickness. We see that if the target thickness is increased from 6 mm to 20 mm, the positron yield (positrons within the damping ring acceptance, per electron in the undulator) increases from 1.2 to 1.8. This is not a strong dependence, and indicates that any thickness of more than about 6 mm would be sufficient, considering only the yield. A thicker target has benefits in increasing the yield. Over a similar range of thicknesses, the positron polarisation varies by about 5%.

Energy deposition is another issue of concern. Changing the target thickness will change not only the energy deposited in the target, but also the energy deposited in the downstream components. Fig. 3.24 shows the energy deposition in the target, adiabatic matching device and capture RF as a function of target thickness. We see that the energy deposition in these components increases linearly with the target thickness. However, it is desirable to keep the energy deposition as low as possible to protect these

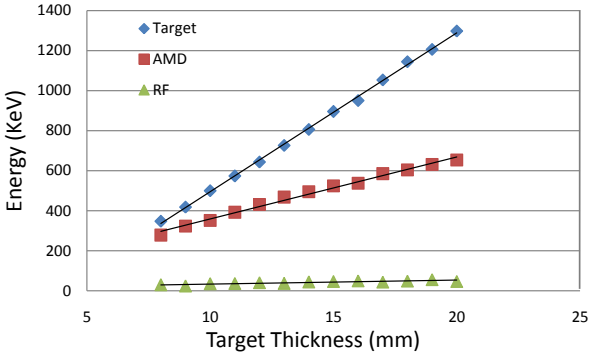

Figure 3.24: Energy deposition in target, adiabatic matching device and RF as a function of target thickness.

systems from damage. Therefore, a thinner target is beneficial.

The current baseline specification of a target thickness of 14.8 mm provides a compromise between positron yield and mechanical strength (which benefit from a thicker target), and issues such as energy deposition and positron distribution (which benefit from a thinner target).

3.3.2 Target Rotation

With the baseline ILC parameters, the average photon beam power from the undulator will be 131 kW. From FLUKA simulations, about 8% of the power, or 10 kW, will be deposited in the target. With a spot size of 1.7 mm (rms - we treat this as a radius) and thickness 14.8 mm (0.4 radiation lengths) this power in a stationary target would be deposited in a volume of about 0.13 cm^3. The density of Ti-6%Al-4%V is 4.4 g/cm^3, and the specific heat capacity is 0.53 J/g/K. Therefore, the rate of temperature rise would be about 33,000 K/s.

To keep the temperature rise within reasonable limits, we can use a rotating target, so that the beam is incident on the rim of a wheel. The axis of rotation of the wheel is parallel to the direction of the beam. If the rim is moving at 100 m/s (for example, a wheel of diameter 1 m rotating at approximately 2000 rpm), then over the length of the ILC pulse (1 ms), the rim moves a distance of 10 cm. The energy deposited in the target per machine pulse is 2 kJ, which would be deposited in a volume 5 cm^3 of the target. This would lead to a temperature rise of about 170 K per machine pulse. The melting point of Ti-6%Al-4%V is about 1600°C. Under these conditions, it is feasible

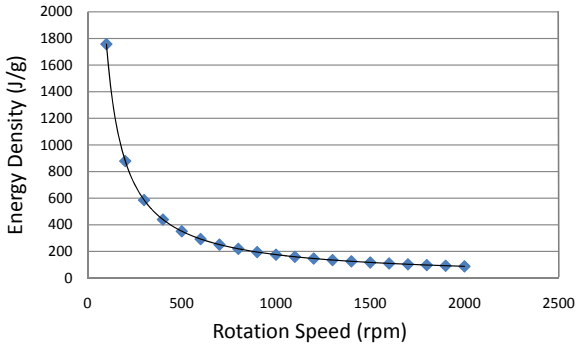

Figure 3.25: Energy deposition in an ILC positron production target, as a function of rotation speed.

to provide sufficient cooling to operate the target at a reasonable temperature.

Fig. 3.25 shows the energy deposition in the target per machine pulse, as a function of rotation speed for a wheel of diameter 1 m. The energy deposition is inversely proportional to the rotation speed. However, there are engineering limitations on how fast the target can be rotated, because of the motor, power supply and other factors. Here, we will discuss one particular issue, which is the eddy currents generated if the target wheel spins at high velocity in a strong magnetic field.

For the ILC undulator-based positron source, in order to increase the capture efficiency, an optical matching device is located after the target. The capture efficiency is increased if the target is partially immersed in the magnetic field of the matching device. However, when the target rotates in the magnetic field, eddy currents will be generated by electromagnetic induction. The eddy currents will lead to heat deposition in the target, and also to drag forces against the target rotation. Since the field of the matching device can be large (up to 6 T), the eddy current effects can be strong.

In order to investigate the effects of eddy currents [56], a target wheel prototype for the ILC positron source has been built at Daresbury Laboratory. Experiments using this target wheel, aimed at understanding the eddy currents, will be described in more detail in Chapter 5. However, the results indicate (for example) that for a target rotating at 2000 rpm in a field of 1.44 T, the eddy current power is about 21 kW. For the case of the ILC, the field could be as high as 6 T. To reduce the power dissipated in the eddy currents, the field of the optical matching device should be reduced (which would lead to lower capture efficiency), or the speed of rotation of the target wheel should

be reduced (which would lead to greater heating of the target wheel). The results of the target wheel prototype experiment and their implications will be discussed in more detail in Chapter 5.

3.4 Optical Matching Device

Positrons coming from the target have a mean energy of about 5 MeV. Before injection into the damping rings, they must be accelerated to 5 GeV. In the first stage of the accelerating RF, following the target, focusing of the beam is provided by a solenoid field of strength 0.5 T. However, the beam coming from the target has a distribution that would be matched to a much stronger field. Increasing the focusing field in the accelerating section would make the RF systems very difficult. Therefore, an optical device is used to match the positron distribution from the target, to the focusing solenoid in the RF.

As already mentioned in Section 2.4, if a distribution of particles is correctly matched to a solenoid field, then the distribution will simply rotate as the beam moves along the solenoid, without any variation in transverse size. A beam will be correctly matched to a solenoid of field strength B_s, if the beta function describing the beam distribution is:

$$\beta = 2\frac{B\rho}{B_s}, \tag{3.7}$$

where $B\rho$ is the beam rigidity. Typically, the positron distribution from the target has a very wide energy spread, and this makes it difficult to specify an exact value for the beam rigidity. However, taking a typical distribution, and using the average positron energy to determine the beam rigidity, we find that the distribution would generally be matched to a solenoid field of strength much larger than 0.5 T. Therefore, some component is needed to transform the phase space at the exit of the target to the phase space matched to the 0.5 T solenoid in the first accelerating section. For the ILC, the transformation is achieved using a adiabatic matching device (AMD). An AMD provides a solenoid field that tapers smoothly with distance from the target [57]. Such a field can be produced using a flux concentrator.

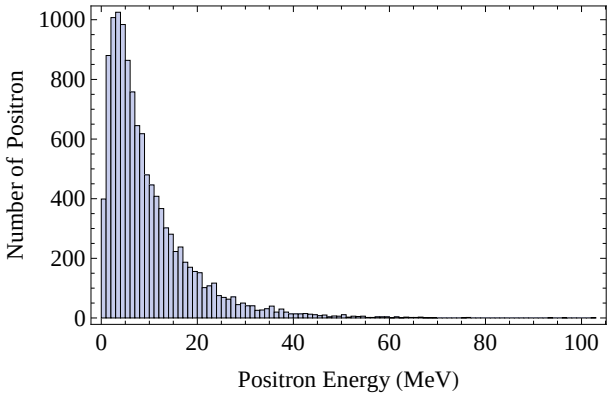

Figure 3.26: Positron energy spread immediately after the target, using ILC baseline parameters.

3.4.1 Positron Distribution After the Target

In order to study the matching device, we will perform tracking simulations, using the positron distribution after the target. Fig. 3.26 shows the energy distribution for the positrons produced from the target using the ILC baseline parameters. The large energy spread makes it impossible to achieve a perfect matching between the target and the solenoid in the linac. Hence, optimisation of the parameters of the adiabatic matching device to achieve a low rate of positron loss is best done by simulation.

Fig. 3.27 shows the horizontal phase space of the positrons immediately after the target. Positrons in different energy ranges have been marked with different colours. Higher energy positrons tend to have lower values for the transverse coordinates and momentum. In other words, particles with large divergence angles or transverse coordinates are more likely to have low energy. These positrons will be lost by hitting the beam pipe during propagation along the AMD, if the matching device is not properly optimised.

For a given distribution, we can estimate the emittance from:

$$\varepsilon_x = \sqrt{\langle x^2 \rangle \langle p_x^2 \rangle - \langle x p_x \rangle^2}, \tag{3.8}$$

and the beta function from:

$$\beta_x = \frac{\langle x^2 \rangle}{\varepsilon_x}. \tag{3.9}$$

If we take positrons with energy in the range 1 – 10 MeV from the distribution shown in Fig. 3.27, then we find $\beta_x \approx 6\,\text{mm}$. Using $B\rho = P_0/e$, with $P_0 = 5\,\text{MeV/c}$, the

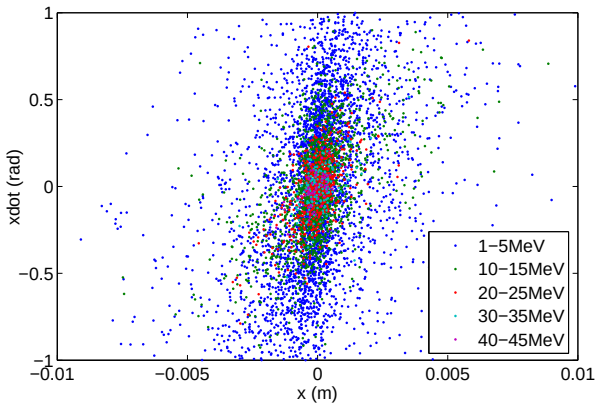

Figure 3.27: Positron transverse phase space immediately after the target, using ILC baseline parameters.

beam rigidity is approximately 0.017 Tm. This implies that the distribution would be matched to a solenoid field with strength:

$$B_s = 2\frac{B\rho}{\beta} \approx 5.7\,\mathrm{T}. \tag{3.10}$$

Let us take the initial field of the AMD to be $B_0 = 6\,\mathrm{T}$. To match the positron distribution to the focusing solenoid in the RF section, the phase advance μ over the AMD should be a half-integer$\times\pi$, where:

$$\mu = \frac{B_0}{2B\rho}\int_0^{z_{\max}} \frac{1}{1+gz}\,dz. \tag{3.11}$$

With a taper parameter $g = 28\,\mathrm{m}^{-1}$, and a field varying from 6 T to 0.5 T, the length of the AMD will be 0.39 m; and the phase advance will be $\mu \approx 2.5 \times 2\pi$. These values for the fields, taper parameter and length of the AMD are reasonable for engineering purposes. We shall take the ILC baseline parameters as nominal values in our simulations: initial field 6 T; final field 0.5 T; and taper parameter $30\,\mathrm{m}^{-1}$ (corresponding to length 0.3667 m, and phase advance 2.33×2π). It will be difficult to achieve fields above 6 T in the AMD: therefore, we shall treat this as an upper limit.

3.4.2 Single Particle Motion in the Matching Device

To begin to understand the beam dynamics in the adiabatic matching device, we shall first consider the motion of single particles as they move through the field. Let us launch a positron with energy 5 MeV as an example. We shall take as initial values for the dynamical variables $x = 0$, $y = 0$, $p_x = 0.01$ and $p_y = 0$. Note that p_x and p_y are the conjugate momenta normalised by the reference momentum P_0. This particle starts on the axis of the AMD, but with some small horizontal angle (approximately 10 mrad). We assume that the fringe field of the AMD can be modelled as a "flat" field (i.e. with zero longitudinal extent). In that case, the transfer matrix for the fringe field is the identity.

Because of its transverse momentum, the particle will make cyclotron oscillations as it moves along the AMD. The trajectory through the AMD, and through part of the constant solenoid field of the RF section, is shown in Fig. 3.28. Initially, the particle sees a strong solenoid field, which leads to rapid, low-amplitude oscillations. The amplitude of the oscillations increases, as does the period, as the field strength decreases. In the constant field of the focusing solenoid in the RF section, the amplitude and period of the cyclotron oscillations remains constant. The projection of the path of the particle onto the $x-y$ plane is shown in Fig. 3.29. In order for the positron to avoid hitting the beam pipe, the radius of the beam pipe needs to be greater than the maximum value of $\sqrt{x^2+y^2}$.

3.4.3 Initial Field and Taper Parameter

In this section, we will present the results of simulations of positron transfer efficiency, using the tracking code SAMM [58] to track positrons through an AMD linking the target to the long solenoid in the RF section. The transfer efficiency is defined as:

$$\text{transfer efficiency} = \frac{\text{number of positrons at exit of matching device}}{\text{number of positrons at exit of target}}. \tag{3.12}$$

The initial positron distribution is generated using Geant4, using the baseline ILC parameters. There is no photon collimator, and the target wheel will be the same dimensions as in the ILC Reference Design Report. The positron distribution from Geant4 will be passed to SAMM to perform the tracking through the AMD. The nominal parameters of the AMD are 6 T initial field tapering down to 0.5 T final field, in a

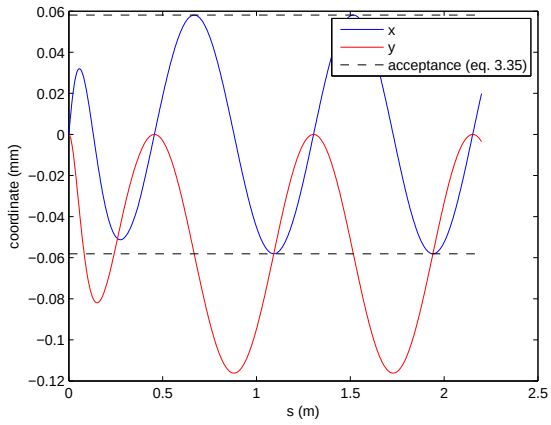

Figure 3.28: Trajectory of a particle with energy 5 MeV in the nominal AMD field and part of the constant solenoid field in the RF section.

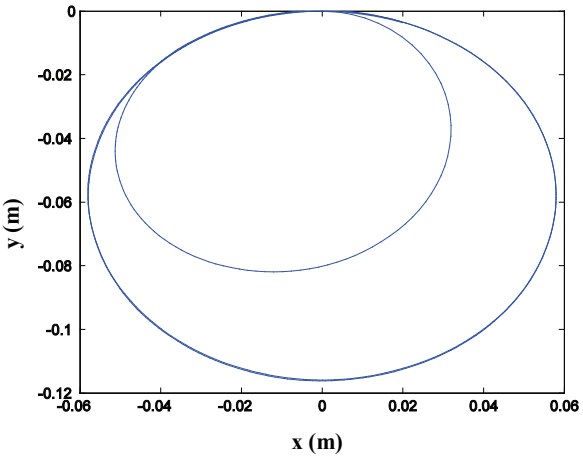

Figure 3.29: Projection of the trajectory in Fig. 3.28 onto the $x - y$ plane.

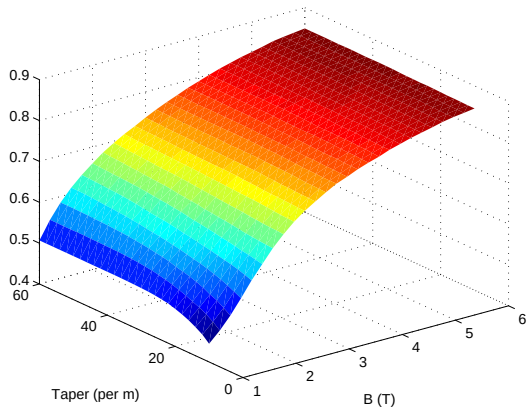

Figure 3.30: Transfer efficiency as a function of initial magnetic field and taper parameter in the AMD, using ILC baseline parameters.

distance of 366.7 mm (taper parameter $30\,\mathrm{m}^{-1}$). For the present, we shall assume that there is no gap between the target and the field of the AMD. In practice, this would mean that the target would be rotating in a 6 T field, which would lead to problems with eddy currents. We shall not consider this issue here. In Section 3.4.5 we shall consider the effect of a gap between the target and the field of the AMD: this will ease the problems with eddy currents, but, as we shall see, could lead to larger positron losses.

Fig. 3.30 shows how the transfer efficiency from the target to the RF section varies as a function of AMD initial field and taper parameter. There is a clear dependence on the initial field, with the transfer efficiency increasing with field strength. However, except for very low values of the taper parameter and field strength, the transfer efficiency has little dependence on the taper parameter. This is probably because of the large energy spread on the positron beam from the target: the phase advance of every particle is different, and covers a wide range, irrespective of the value of the taper parameter. Therefore, changing the taper parameter has little effect on the overall behaviour of the beam.

3.4.4 Initial Field and Entrance Aperture

A number of engineering issues could be simplified if a good transfer efficiency could be achieved with a reduced field in the AMD. This would reduce the field on the target

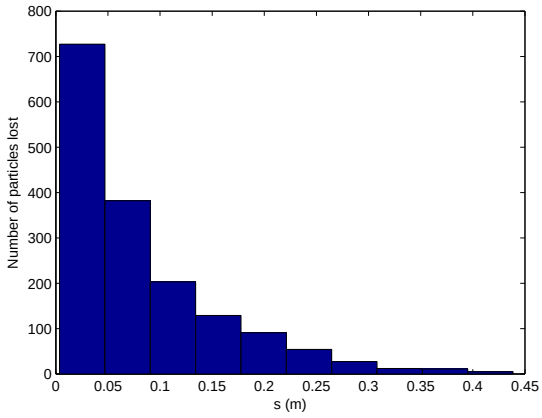

Figure 3.31: The number of positrons lost as a function as longitudinal position in the AMD, for a low field case.

itself, reducing the eddy currents; and the flux concentrator itself would become easier. The required strength of the field in the AMD is really determined by the shape of the positron distribution from the target. However, if we understand how the losses occur, we may be able to design the system to allow some mismatch between the initial positron distribution and the entrance field of the AMD, while still maintaining good transfer efficiency.

When the positron beam goes through the flux concentrator, for low initial field strengths, the positron losses could be as much as 50%. Fig. 3.31 shows the number of positrons lost as a function of longitudinal position in the AMD, for a low field case. We see that the majority of losses occur near the entrance of the AMD. This suggests that the physical aperture of the AMD is the cause of the losses, rather than poor optical matching. If poor optical matching was the cause of the losses, this would appear as an increase in beam size further down the AMD: and this is where we would then expect to see the losses occuring. Since the losses occur close to the entrance, there is little time for the distribution to evolve before the losses occur. The cause of the losses is that some positrons have large coordinates and large divergence angles (up to 1 radian). These particles perform only a fraction of a cyclotron period, before they hit the beam pipe, and are lost from the beam. If the field is small, then the cyclotron radius is large, and this makes particles more likely to hit the beam pipe.

Fig. 3.32 shows the transfer efficiency as a function of initial magnetic field and

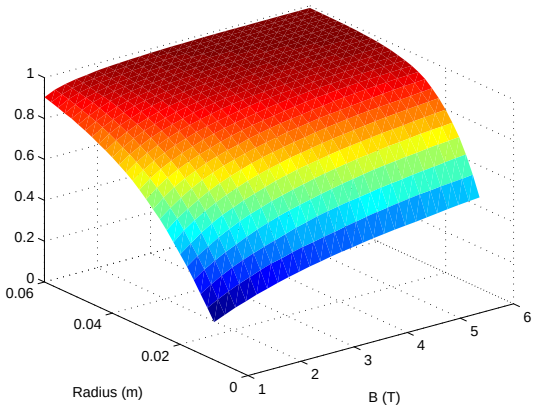

Figure 3.32: Transfer efficiency as a function of magnetic field and aperture radius in the matching device. Standard ILC undulator-based positron source parameters have been assumed.

physical aperture. As expected, the transfer efficiency improves with larger field and with large physical aperture. At the largest apertures, around 60 mm radius, the transfer efficiency is very good, about 90%, even for initial fields as low as 1 T. This suggests that it might be possible to improve the ILC design, by optimising the field strength and aperture in the AMD. Fortunately, a lower field strength should make it easier to achieve a large aperture. The present design specifies a 6 T initial field: this will cause problems with eddy currents in the target. However, the same transfer efficiency could be achieved with a lower field in the AMD, if reducing the field also allows an increase in the aperture of the AMD.

3.4.5 Gap Between Target and Matching Device

So far, all the simulations have assumed no gap between the target and the matching device. In practice, this means that the target rim will be partially immersed in the magnetic field of the matching device. However, when the target rim passes into and out of the magnetic field, current loops will be created by electromagnetic induction. These eddy currents will generate heat, and also create a drag force acting against the rotation of the target wheel. We have already seen that we can maintain the same transfer efficiency with a lower field, if it is possible at the same time to increase the physical aperture of the AMD. However, this is a technical issue for the design of the

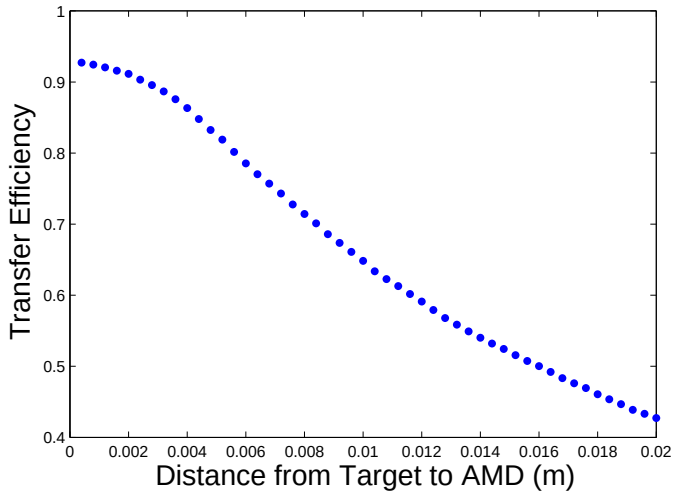

Figure 3.33: The positron transfer efficiency as a function of gap distance from target to entrance of the matching device.

AMD, and we should explore other possibilities to reduce the effects of eddy currents in the target [59].

Another way to reduce the eddy currents is to introduce a gap between the target and the matching device. If the gap is large enough, then the field will naturally decrease to a much smaller value. It may also be possible to introduce magnetic material (clamp plates) to suppress the magnetic field outside of the AMD itself.

Fig. 3.33 shows the positron transfer efficiency as a function of the gap from the target to the matching device, with the nominal ILC system parameters (and AMD initial field 6 T, and taper parameter $30\,\mathrm{m}^{-1}$.)

As we can see, when the gap increases from zero to 20 mm, the transfer efficiency will decrease from a little over 90%, to about 42%. The problem is that the positron distribution at the exit of the target has a very large divergence. This means that over a very short distance, the transverse positions of some of the positrons will increase significantly. This will make it more difficult to capture the positron distribution cleanly. To maintain good transfer efficiency, a gap of not more than 1 or 2 mm should be allowed between the target and the AMD. Unfortunately, this is unlikely to lead to any significant reduction of the field in the target.

3.5 Conclusion

In this chapter we have examined the ILC positron source. The undulator has been well optimised in previous work. Properties of the undulator radiation, including the spectral and angular distribution are well understood. Of particular significance for our investigations is the correlation between the angle of the radiation with respect to the undulator axis, and the polarisation. This raises the possibility of improving the polarisation by collimating the radiation beam.

Although some designs have been proposed for photon collimators for the ILC, detailed studies of the effect on polarisation, and of heat loads and activation, have not previously been performed. We have applied analytical calculations and simulation codes (FLUKA and Geant4) to investigate and understand the performance of two proposed designs for the photon collimator. Both designs are effective in collimating the photon beam, and our results show how it may be possible to select the collimator aperture to trade off the intensity against the polarisation. It should be possible to achieve positron beam polarisation of more than 60% with a tight collimation; but the positron yield will be very low. A more realistic figure for the polarisation is around 50%; the loss in intensity from the photon collimator could then be compensated by a realistic increase in length of the undulator. Without any collimation, the positron polarisation will be around 30%.

Although both collimator designs perform the basic function of collimation equally well, the Model 2 design has some benefits: it is more compact, has better capability for handling the heat load and shows lower activation. There could be further work to optimise the design, based on the results presented in this chapter.

The power load on the positron production target from the undulator radiation is a major issue for ILC. To keep the temperature rise within reasonable limits, the target must be rotated at high speed. If the target is within the strong field of the optical matching device, then this will lead to eddy currents that will themselves cause significant power load in the target, and also lead to forces tending to slow the rotation of the target wheel.

We have investigated the performance of the optical matching device, looking for ways to reduce the field on the target, while maintaining the capture efficiency. One possibility is to increase the physical aperture of the AMD. Although the distribution of

positrons from the target would become mismatched with the AMD when the field is reduced, an increase in the physical aperture can compensate any adverse effects. Design work on the AMD would be useful, to see how far the aperture could be increased.

Finally, we looked at the possibility of introducing a gap between the target and the AMD. Such a gap could help reduce the field from the AMD on the target. Unfortunately, because of the large divergence of the positron beam from the target, even a small gap would lead to large losses. This does not seem a promising route to reduce the effects of eddy currents in the target.

The eddy currents themselves are the focus of experiments using a prototype target wheel at Daresbury Laboratory. These experiments will be described, and results reported, in Chapter 5.

4

Undulator-Based Positron Source for CLIC

4.1 CLIC Positron Source

CLIC (the Compact LInear Collider) is a proposed high-energy linear collider designed for precision studies of the Higgs boson and other new physics phenomena [21]. Development of the collider is being carried out by a global collaboration, led by CERN. In CLIC, electrons and positrons will be collided at centre-of-mass energy up to 3 TeV. In order to achieve the specified luminosity, CLIC will need of order 10^{14} positrons per second; for some of the proposed studies, the positron beam will need to be polarised. The required rate of positron production is a factor $\sim$18 greater than any previous source, such as the SLC at SLAC. So far, three schemes have been considered for the positron source [27]: a conventional source, a source based on Compton back-scattering, and an undulator-based source. The Compton scheme is currently the preferred option for the CLIC polarised positron source.

Each of the options for the CLIC positron source has its own advantages and disadvantages. For example, a conventional source is a classic design, which is relatively simple and low cost [60]. It can be operated independently of the electron source, which could be a major advantage for machine commissioning and tuning. It uses a high energy (a few GeV) electron beam striking a thick target made from some high-Z material, to create electromagnetic showers [27]. Positrons will be selected and captured for collision. However, there are some disadvantages of using a conventional positron source.

The positrons do not have polarisation and the thermal load on the target is very high [61]. Recently, some improvements [19] have been suggested for a conventional positron source design that would help mitigate issues such as the thermal load: however, these improvements are still at the R&D stage, and we do not discuss them here.

Another option is a laser-Compton based positron source, which is currently the preferred choice for CLIC polarised positron source [61][62]. A laser beam collides with a high energy electron beam (separate from the colliding beam), from which the photons in the laser beam will gain energy. The back-scattered photon beam (now with short wavelength) will strike the target to produce positron and electron pairs. This technology requires further development before it can be implemented in a linear collider, and is the subject of an active R&D program. However, this option has the potential to provide a positron beam with the properties (intensity and polarisation) required for CLIC. Also, like the conventional source, it can be operated independently of the electron beam.

An undulator-based positron source could provide a good alternative to the present laser-Compton source for CLIC [63][64]. Although not yet demonstrated on the scale required for a linear collider, proof-of-principle experiments of an undulator-based positron source have successfully been carried out at SLAC [24]. This type of source has been extensively studied for ILC; the studies have included the construction and testing of prototype components (such as undulator sections, and the production target), as well as modelling of the whole system. The differences in parameters between ILC and CLIC (including the energy of the electron beam, and the time structure of the beam) mean that although a very similar design as exists for ILC could be adopted for CLIC [65], this may not be the optimal solution. Also, issues associated with the machine upgrade (from Stage 1, 500 GeV centre of mass collision energy, to Stage 2, 3 TeV centre of mass) mean that some modification to the positron source would be required when the upgrade is made. In this chapter, we consider modifications to the ILC design that could make an undulator-based positron source an attractive option for CLIC. We also consider how design choices could be made so that the energy upgrade, as far as the positron source is concerned, can be made as easily as possible [66].

The energy upgrade for CLIC has a major impact on the design of an undulator-based positron source. In principle, there are various ways that the energy upgrade could be achieved. For example, the length of the linac could be kept fixed, but the ac-

celerating gradient increased. In that case, if the undulator was kept at a fixed position, the energy of the electron beam in the undulator would increase by a factor of six as a result of the energy upgrade. This would have a major impact on the performance of the positron source. However, given the practical limitations on accelerating gradient in a linac, this is not a likely, or even practical, upgrade scenario.

It is more likely that the energy upgrade would be achieved by extending the linac in the opposite direction to the acceleration, but keeping the accelerating gradient fixed. In that case, if the electron beam energy in the undulator was 150 GeV before the upgrade (maximum beam energy 250 GeV), then if the undulator position was kept fixed, after the upgrade the electron beam energy in the undulator would be 1.4 TeV (maximum beam energy 1.5 TeV).

In either upgrade scenario, the electron beam energy at the original location of the linac will be significantly increased as a result of the energy upgrade [67]. The dependence of the photon beam properties on the electron beam energy means that it will not be possible to use a single undulator, in a fixed position, for both Stage 1 and Stage 2. For example, the total radiation power from an undulator scales with the square of the energy of the electron beam in the undulator. For the ILC parameters, with the electron beam at 150 GeV, the power load on the target is already an issue. Although an undulator with the ILC parameters could be used in CLIC for Stage 1, after an upgrade to Stage 2 the power from the same undulator in the same location would be increased at least 36 times. This is not a realistic scenario.

More realistic options that could be considered for the positron source when performing an energy upgrade in CLIC are as follows:

1. Locate the positron source in a new position, but keep the undulator parameters fixed.

2. Use a new undulator with different parameters, in the same location as the original undulator.

3. Use a new undulator in a new location.

In principle, the first option is very simple to consider: the undulator could be moved to a point in the new linac where the electron beam energy is the same as before, and everything (apart from the location) could remain unchanged. However,

there is a considerable amount of infrastructure included in the positron source, apart from the undulator itself. This includes: the photon transport line; photon collimator; target (and remote handling station); matching device; acceleration section; transport line to damping ring. If an undulator with different parameters would make it feasible to keep the positron source in the same location, then this could be an attractive option.

In the following sections, we discuss the parameters of various components of an undulator-based positron source for CLIC. We identify appropriate parameter choices for different operating and upgrade scenarios. Our discussion is based on the results of models that we have developed to understand the impact of various design choices on key parameters, namely the positron production rate and capture efficiency, and the polarisation.

4.2 Helical Undulator

In principle, a helical undulator with the same parameters as for ILC could be used for both Stage 1 and Stage 2 of CLIC, if it were located at the 150 GeV point in the electron linac in each case. The characteristics of the synchrotron radiation would be identical, except that the average power would be somewhat lower for CLIC than for ILC, because of the lower average current in the linac. The time structure of the radiation would be different: for CLIC the radiation would occur in shorter but more intense bursts, and this is a possible issue for the target. But assuming that the target can survive the peak power flux, the lower average power of the undulator radiation in CLIC would be an advantage.

However, it is interesting to consider whether it would be possible to maintain a fixed location for the undulator during the upgrade from 500 GeV centre of mass collision energy, to 3 TeV centre of mass collision energy. This would be useful, because it would minimise the amount of reconstruction involved for the other parts of the positron source. Since the synchrotron radiation power depends on the square of the electron beam energy, the most promising configuration would minimise the factor by which the energy of the electron beam in the linac is increased as a result of the upgrade. This would then minimise the changes needed to other parameters of the undulator.

The most likely way in which the energy upgrade would take place, is by increasing the length of the linac, while keeping the accelerating gradient the same. Therefore, if

the electron beam energy in the undulator is E_1 in Stage 1, the energy in Stage 2 will be $E_2 = E_1 + 1.25\,\text{TeV}$. We minimise the ratio E_2/E_1 if we choose E_1 to be as large as possible: therefore, we consider placing the undulator at the 250 GeV point in Stage 1, that is, at the end of the linac. This means that in Stage 2, the electron beam energy will be 1.5 TeV. This may turn out not to be feasible. Nevertheless, we take this as our starting point.

Let us now consider what modifications we should make to the undulator parameters, if we are to place the undulator at the 250 GeV location in CLIC. Initially, let us assume that we wish to keep fixed the average synchrotron radiation power, and the number of photons produced. The radiation power should not be allowed to increase, because this will cause problems for the photon collimator and the target. The total number of photons should be kept fixed, because this determines the number of positrons created in the target (by pair production). We mention at this point that there are other factors that affect the total positron yield, apart from the number of photons: these include the photon energy, and the acceptance of the systems downstream of the positron source. These factors are important, but they are not straightforward. Therefore, we put them aside for the moment, but will return to them later.

4.2.1 General Scaling Relationships

The number of photons per second $\dot{N}_\gamma$ produced by an electron beam in an undulator depends on the electron beam current I, the number of undulator periods N_u, and the deflection parameter K [68]:

$$\dot{N}_\gamma \propto I N_u K. \tag{4.1}$$

The total radiation power P_γ depends on the electron beam energy E, the electron beam current, the number of undulator periods, the deflection parameter, and the undulator period λ_u:

$$P_\gamma \propto \frac{E^2 I N_u K^2}{\lambda_u}. \tag{4.2}$$

The photon energy is also a significant quantity, because it affects the energy of the positrons that come out of the target, and this in turn affects the capture efficiency. The photon energy at the n^{th} harmonic in the undulator spectrum is given (for ultra-relativistic electrons) by:

$$E_{\gamma,n} \approx \frac{2nhc\gamma^2}{\lambda_u(1+K^2)}. \tag{4.3}$$

Note that as K increases, there is a linear increase in the photon flux. However, the total radiation power increases as the square of K, while the photon energy actually *decreases*. These three statements appear to be contradictory. However, as K increases, the proportion of photons in the higher harmonics also increases, so that the reduction in the energy of each harmonic is outweighed by the greater contribution that photons in the higher harmonics make to the total radiation power.

Let us assume for the moment that the electron beam current will remain fixed. (Again, this is not necessarily the case for the CLIC energy upgrade, but we will return to this later.) Then, to keep the photon production rate constant, we need to keep the product of the number of periods and the deflection parameter constant. Any reduction in the number of periods (to try to reduce the length of the undulator) would require an increase in the deflection parameter. However, all other parameters remaining constant, increasing the deflection parameter would increase the radiation power faster than it would increase the photon flux. Therefore, let us (again, just for the moment) assume that we keep the deflection parameter itself fixed, at a value of about 1. Then, the number of undulator periods must be the same, for whatever energy electron beam is used.

If N_u and K are fixed, then to keep the radiation power constant, the undulator period λ_u must increase in proportion to the square of the electron beam energy. So, for an undulator at the 250 GeV point in the electron linac, the period must increase by a factor 2.78, compared to the period for an undulator at the 150 GeV point. For ILC, the undulator has period 11.5 mm, and total length 147 m. Therefore, in CLIC (Stage 1), with 250 GeV electron beam energy, the undulator period would be about 32 mm, and the total length would be a little under 410 m. This does not seem attractive, but on the scale of the entire facility, may be feasible.

However, after the energy upgrade, if kept at the end of the linac, the electron beam energy in the undulator would be 1.5 TeV. To keep the same photon flux and radiation power, the undulator period would have to increase to 1.15 m, and the total length would have to increase to 14.7 km. This is clearly not realistic. However, there are several factors that we have not so far taken into account, that could help to reduce this length.

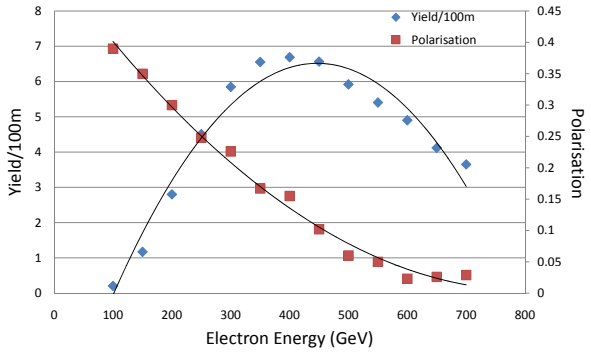

Figure 4.1: Positron yield (per 100 m of undulator) and polarisation as functions of electron beam energy from 100 GeV up to 700 GeV, with ILC undulator parameters.

4.2.2 Photon Energy

The first additional factor is the effect on the positron yield of increasing the photon energy. Fig. 4.1 shows the yield and polarisation for the ILC undulator-based positron source, with electron beam energy from 150 GeV up to 700 GeV. Note that the photon energy varies with the square of the electron energy. At 150 GeV, the average photon energy is about 10 MeV. At 300 GeV electron energy, the photon energy will increase to about 40 MeV. Above this energy, the yield reaches a maximum, then starts to decrease: this is because the parameters of the components following the target have not been re-optimised to allow for the increase in the energy of the positrons produced.

A similar effect can be seen if we consider the effect of the undulator period on the yield, in the case of ILC. Fig. 4.2 shows the positron yield as a function of undulator period, with all other parameters (including the deflection parameter) remaining the same, for two different electron beam energies. From Eq. 4.3 we see that the photon energy is inversely proportional to the undulator period. In Fig. 4.2, we see that if the undulator period is halved, then the yield increases by a factor of about 3.

For CLIC, let us assume that we can adjust the undulator parameters to increase the photon energy to about 40 MeV, and that this will increase the yield by (roughly) a factor of four. Therefore, we reduce the period of the undulator by a factor of four; and we also reduce the number of periods by a factor of four (since we need only one quarter as many photons). The overall length of the undulator is reduced by a factor 16. For Stage 1, our initial assumption was that the undulator period was 32 mm. Reducing

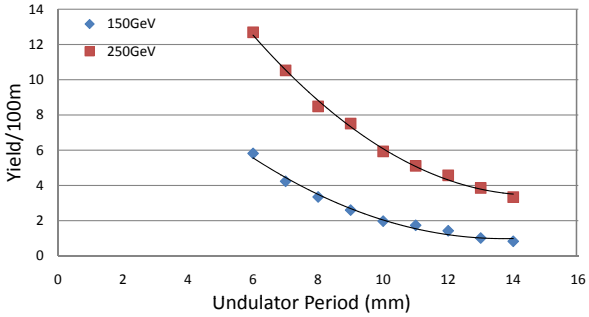

Figure 4.2: Yield per 100 m of undulator as a function of undulator period (deflection parameter 0.92), with 150 GeV electron beam energy (blue) and 250 GeV electron beam energy (red). The ILC damping ring acceptance is applied.

this by a factor of four would give a period of 8 mm; however, using modern equipment and techniques, it becomes increasingly difficult to wind the coils on a helical undulator with a period below about 11 mm. The brittleness of the superconducting wires also imposes constraints on the geometry that can be achieved [69][70][71]. Therefore, we set the undulator period to 11.5 mm. Since we do not increase the photon energy by a full factor of four, we do not reduce the number of periods by a full factor of four. Instead, we reduce the number of periods by the same factor we applied to the period itself. Then, the total length of the undulator would be 53 m. For Stage 2, we can reduce the period and the number of periods by a full factor of four. Then, we have a period of 288 mm, and a total length of 920 m.

4.2.3 Acceptance

The second additional factor that allows us to reduce the undulator length is the larger acceptance in CLIC, compared to ILC, for positrons produced from the source. The acceptance defines those particles that will survive from the positron source (exit of the matching device) to the exit of the damping ring. The acceptance is determined by physical and dynamic aperture limitations in the transport lines and damping rings. The reasons that CLIC has a larger acceptance than ILC are as follows.

In the case of ILC, the superconducting RF linac works most efficiently for long beam pulses. Although the beam is compressed to reduce the size of the damping ring, large (6.4 km) rings are still needed to accommodate each machine pulse. This makes it impractical to use a pre-damping ring, which could be optimised for a large

acceptance, without needing to achieve the very low emittances needed in the beams at the interaction point.

However, for CLIC, the machine pulses are much shorter, and the damping rings are correspondingly smaller. This makes it possible to use a pre-damping ring for the positron beam. The pre-damping ring is designed to have a large acceptance, but does not achieve a very small final emittance. But the final emittance is small enough that the beam can be injected efficiently into the main damping ring, which must have a very small final emittance, and will therefore have a smaller acceptance than the pre-damping ring.

We should emphasise that the acceptance of the systems downstream of the positron source is a complicated issue, depending on many different factors, including features of the design of the matching device, acceleration section, transfer line and damping ring. At the moment, the designs of all these systems are incomplete. Therefore, it is impossible to state with certainty what the acceptance will be. To some extent, design choices will depend on how the acceptance affects the positron source. For example, a larger aperture in the transfer line could improve the acceptance (if this were the limiting factor) and allow a reduction in the length of the undulator. However, increasing the aperture of the transfer line would increase the costs of the vacuum and magnet systems in the transfer line. Without a great deal of study and design work it is not possible to say what the optimum designs for all the various systems will be. Therefore, we consider the impact on the positron source of nominal values of the acceptance for CLIC, shown in Table 4.1. The results should provide some guidance for the acceptance actually required for the transport lines and damping rings in CLIC.

The acceptance of a damping ring is specified in terms of the maximum betatron amplitude and maximum energy deviation for a particle that will be captured by the damping ring. The horizontal betatron amplitude A_x is defined by:

$$A_x = \gamma \left(\gamma_x x^2 + 2\alpha_x x p_x + \beta_x p_x^2 \right), \tag{4.4}$$

where γ is the relativistic factor, x and p_x the horizontal coordinate and normalised momentum of the particle, and α_x, β_x and γ_x are the Twiss parameters. The vertical betatron amplitude is defined in a similar way. Note that the betatron amplitudes are constant for a particle moving through a simple (linear) magnetic lattice, or being accelerated in a linac. The specified acceptance values for the ILC damping rings and

Table 4.1: Nominal acceptance specifications for ILC damping rings and CLIC pre-damping ring.

	ILC	CLIC
Maximum total betatron amplitude, $A_x + A_y$	0.09 m	0.57 m
Maximum energy deviation	±0.5%	±1.6%

CLIC pre-damping rings [72] are given in Table 4.1. The values given here are the nominal specifications: in practice, the real acceptance will have a complicated shape in phase space, but particles with the betatron amplitudes and energy deviations shown in Table 4.1 should always be captured by the damping ring.

Note that the longitudinal acceptance for the damping ring is specified as a maximum energy deviation. This actually places a limit on the length of the bunch from the positron source: if the length of the bunch is significant compared to the wavelength of the RF in the accelerating section, then as the bunch is accelerated, particles at the head and tail of the bunch (which will be slightly off-crest) will get less energy than particles at the centre of the bunch (which will be on-crest). For the ILC and CLIC parameters, this "RF curvature" effect dominates the energy spread of the bunch by the time it reaches the damping ring. The longer the bunch, the larger the energy difference between the head or tail, and the centre of the bunch. For a maximum energy deviation of ±0.5%, particles for the positron source in ILC (with RF frequency 1.3 GHz) should be no more than ±5 mm from the centre of the bunch. For a given bunch length, the energy spread from the RF curvature increases with RF frequency. For CLIC, the bunch spacing is 0.5 ns, so the minimum RF frequency is 2 GHz: this means that the energy spread on a bunch with particles within ±5 mm of the centre of the bunch will be ±1.4%. However, this is still within the expected acceptance of the predamping ring. In the case that a smaller energy spread is required, then a section of linac operating at a higher harmonic frequency can be used to "flatten" the RF curvature. For example, with a 4 GHz section in CLIC, operating at 25% of the voltage of the 2 GHz RF (and phased to decelerate the beam), the energy spread on a bunch (with particles within ±5 mm of the centre) can be reduced to less than ±0.006%. The drawback is the additional cost, and possible aperture and wake field issues with a linac operating at 4 GHz. However, in principle, higher harmonic RF could be used to mitigate the effect of energy acceptance limitations in the predamping ring.

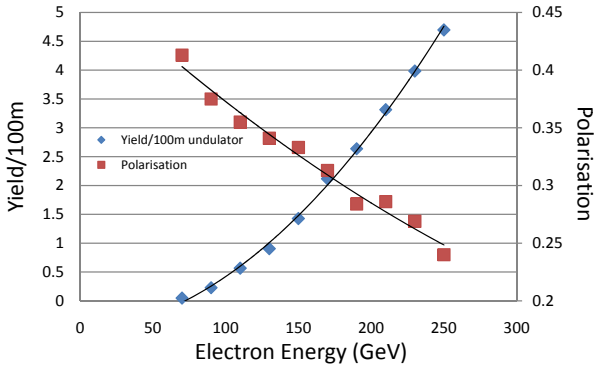

Figure 4.3: Positron yield and polarisation from 100 m of undulator (deflection parameter 0.92, and period 11.5 mm) as a function of electron beam energy. ILC damping ring acceptance is applied.

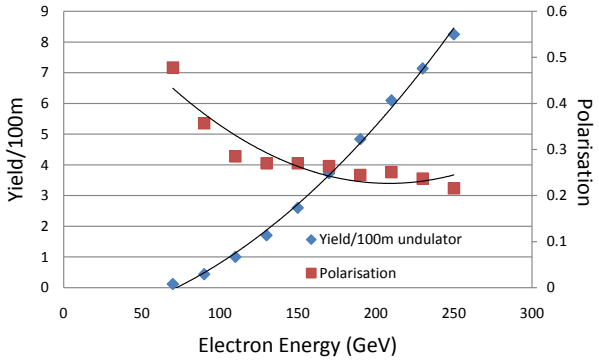

Figure 4.4: Positron yield and polarisation from 100 m of undulator (deflection parameter 0.92, and period 11.5 mm) as a function of electron beam energy. CLIC predamping ring acceptance is applied.

The larger acceptance in CLIC compared to ILC increases the yield by roughly a factor of 2, for the same photon parameters: compare the results shown in Fig. 4.3 (yield and polarisation as functions of energy for ILC) with those shown in Fig. 4.4 (yield and polarisation using the same parameters as Fig. 4.4, except that the CLIC predamping ring acceptance is applied). Therefore, we need only half the number of photons, and this means that we can reduce the length of the undulator by two. In Stage 1, the total length of the undulator would be 27 m; the period stays fixed at 11.5 mm. In Stage 2, the total length of the undulator would be 460 m, and the period would remain fixed at 288 mm. Now the undulator parameters in Stage 1 seem very realistic. For Stage 2, the undulator is still rather long. Note that in both cases, the radiation power on the target is about half what it will be for ILC, because of the large acceptance of the pre-damping ring.

4.2.4 Beam Current and Deflection Parameter

The final additional factor that allows us to reduce the undulator length is the beam current. If the electron current is reduced, the photon flux will also reduce, and the positron yield will be reduced in the same proportion (because all other characteristics of the synchrotron radiation will be unchanged). However, this does not affect overall machine performance, because the number of positrons in collision will still equal the number of electrons. Therefore, a reduction in current is no real loss as far as the photon flux is concerned; but it has benefits in allowing variations in other parameters. For example, if the electron beam current is halved, then we can also reduce the undulator period to reduce the overall undulator length, without any overall increase in the radiation power. However, for both Stage 1 and Stage 2, we have already arrived at the minimum undulator period. We cannot reduce the period below 11.5 mm in Stage 1 because of engineering constraints. We cannot reduce the period below 288 mm in Stage 2 because that would increase the photon energy to a point where the net positron yield would start to decrease. Therefore, it seems that the main benefit of reducing the electron beam current will be to reduce the radiation power load on the target.

In Stage 1, the rate of positron production required is about half that in ILC. Therefore, we can expect the total power on the target in Stage 1 to be less than a quarter of that in ILC.

For Stage 2, the rate of positron production required is about half that in Stage

Table 4.2: Undulator parameters for ILC, and for CLIC with undulator at fixed location during the upgrade from Stage 1 to Stage 2.

	ILC	CLIC Stage 1	CLIC Stage 2
Electron beam energy	150 GeV	250 GeV	1.5 TeV
Undulator period	11.5 mm	11.5 mm	115 mm
Undulator field	0.86 T	0.86 T	0.186 T
Deflection parameter	0.92	0.92	2.0
Total length	147 m	27 m	92 m
Photon energy at first harmonic	10 MeV	28 MeV	37 MeV
Photon beam power	131 kW	69 kW	102 kW
Positron yield (e^+ per e^-)	2.0	2.0	1.6
Polarisation	25%	20%	<1%

1. This would allow the power on the target to be reduced even further. However, it then makes sense to consider an increase in the deflection parameter: this will allow a reduction in the number of periods (and hence the length of the linac) while keeping the photon flux the same. We do not wish to increase the deflection parameter too far, because this will increase the proportion of photons in the higher harmonics, which produce very high energy positrons with a poor capture efficiency. However, an increase in the deflection parameter to a value $K = 2$ may be reasonable. If we reduce the number of periods by a factor of two at the same time, the photon flux will remain constant, and the total radiation power on the target will increase by a factor of two. The radiation power on the target is still less than half the power on the target in ILC, and the energy of the first harmonic in the undulator spectrum has reduced by a factor of roughly 0.4. Therefore, we can increase the undulator period by a factor 2.5, to restore the peak in the undulator spectrum to about 40 MeV; the power on the target will be about the same as for the ILC; but the total undulator length will now be 92 m.

4.2.5 Possible Undulator Parameters

The undulator parameters that we arrive at by the above arguments for CLIC Stage 1 and CLIC Stage 2, are compared with the parameters for ILC in Table 4.2. Note that the yield and polarisation are found from simulation, taking into account the acceptance of the damping ring. The yield and polarisation for CLIC Stage 1 are close

to the expected values. The preceding arguments are relatively safe in this case, because the parameters are close to those for ILC. The main difference is the higher electron beam energy (but 250 GeV for CLIC is less than a factor of two greater than 150 GeV for ILC), and the larger damping ring acceptance. Because of the larger damping ring acceptance, the undulator can be much shorter than in the case of ILC.

For CLIC Stage 2, the yield is a little smaller than expected; but given the approximations that we made in the preceding arguments, the result is quite good. The yield could be increased to 2 (positrons per electron) by a modest increase in length of the undulator. However, the polarisation has been lost. The reason is that positrons are captured that are produced from photons with a wide range of energies and angles. Photons at large angles with respect to the undulator axis have a different polarisation from those close to the axis. While the yield benefits from capturing a wider range of positrons, this is at the cost of the polarisation. In principle, the polarisation could be restored by collimating the (relatively) large angle photons, and increasing the length of the undulator to compensate the reduced photon flux. While an increase in undulator length (by, say, a factor of 2) may be conceivable, the photon beam produced from an electron beam with energy 1.5 TeV in the undulator has a very narrow divergence. This would make collimation to restore the polarisation very difficult.

4.3 Photon Collimator

The photon collimator has been described in Chapter 2: the main functions of the photon collimator are to protect downstream components from photon beam halo or mis-steering; and to provide the possibility of improving the polarisation. The design of a photon collimator for ILC has been discussed in detail in Chapter 3. This design has been developed for an undulator operating with electron beam energy 150 GeV. If the undulator for an undulator-based positron source in CLIC is placed at the same beam energy, then the ILC design already described could be used without modification. However, if the undulator is placed at a higher energy, for example 250 GeV (for Stage 1) or 1.5 TeV (for Stage 2), then the characteristics of the photon beam will be somewhat different, although the total photon power should be no larger (and even smaller) than in the ILC case. In the following subsections, we shall consider the impact of collimation on yield and polarisation, for the CLIC Stage 1 and Stage 2 parameters

shown in Table 4.2; that is, we assume that the positron source is located at the end of the electron linac in both stages of the project.

4.3.1 Photon Collimator for 250 GeV

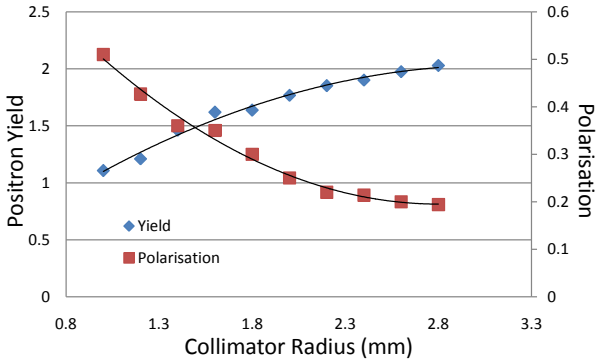

Figure 4.5: Positron yield and polarisation as functions of photon collimator aperture, for CLIC Stage 1 parameters shown in Table 4.2.

Fig. 4.5 shows how the positron yield and polarisation vary as a function of the collimator aperture (from 1 mm to 2.8 mm), with the CLIC Stage 1 parameters shown in Table 4.2. We see that although it is possible to achieve a relatively good level of polarisation (more than 50%), this requires very hard collimation, using a photon collimator aperture of 1 mm. This will reduce the positron intensity by a significant amount. But still, with the Stage 1 operational scenario as shown in Table 4.2, it would be possible to maintain a yield of more than 1 positron per electron. To restore the yield to 2 positrons per electron, the undulator length could simply be doubled to 54 m.

4.3.2 Photon Collimator for 1.5 TeV

Fig. 4.6 shows how the positron yield and polarisation vary as a function of the collimator aperture (from 0.1 mm to 1 mm), with the CLIC Stage 2 parameters shown in Table 4.2. With an electron beam energy of 1.5 TeV, even with an increased deflection parameter, the photon beam divergence is extremely small, making collimation difficult. We see from Fig. 4.6, that if the photon beam is collimated with an aperture of 0.1 mm radius, then polarisation of nearly 50% can be achieved. However, the positron yield would be only about 0.06. This is not practicable. To restore the yield to 1

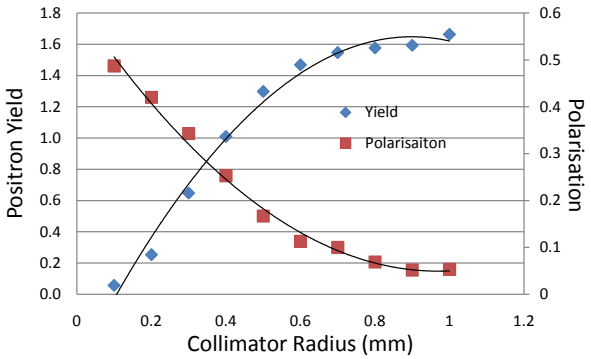

Figure 4.6: Positron yield and polarisation as functions of photon collimator aperture, for CLIC Stage 2 parameters shown in Table 4.2.

positron per electron, the collimator radius would need to be increased to 0.4 mm radius: this would give 25% positron polarisation. To then achieve a yield of 2 positrons per electron, without reduction in polarisation, the undulator length would need to be more than doubled, to over 200 m.

However, it is not clear that collimation with 0.4 mm radius would be practical. The system would be very sensitive to alignment and steering errors. Also, if the photon beam from the undulators needs to be "spread" by steering the electron beam between undulator sections to reduce the peak energy deposition in the target, then it would not be possible to use a collimator to improve the polarisation.

Although it does not appear promising to use a photon collimator to improve the polarisation of the positron beam in CLIC Stage 2 with an undulator at 1.5 TeV, a photon collimator may still be useful for protecting downstream systems from photon beam halo or steering errors.

4.4 Production Target

We have seen that for ILC, the high photon beam power means that the target must rotate at high speed, so that the energy deposition can be spread over a large volume. The rotation is beneficial for ILC because of the relatively long beam pulse: each pulse lasts for about 1 ms, so a rim velocity of about 100 m/s (diameter 1 m, revolution frequency 2000 rpm) means that the energy is spread over a distance of about 10 cm around the rim. However, for CLIC, the pulse duration is about 177 ns in stage 1 and

156 ns in stage 2. Even at a revolution frequency of 2000 rpm, the rim of a 1 m diameter target wheel will move less than 20 μm in this time. Therefore, for a single pulse, the density of the energy deposition will be about the same in a rotating target as in a static target.

In CLIC, the pulse repetition rate will be 50 Hz. Therefore, using the average beam power shown in Table 4.2, the photon energy per pulse will be of order 1 – 2 kJ. Assuming a similar deposition in the target (8% for 14.8 mm thickness) as in the case of ILC, and a similar spot size on the target (about 1.7 mm), then the energy deposition would be of order 200 J per pulse, in a volume of about 0.13 cm^3. With a target wheel material Ti-6%Al-4%V (density 4.4 g/cm^3 and specific heat capacity 0.53 J/g/K), the temperature rise per pulse would be a little under 650°C. Assuming a "slow" rotation (so that each pulse, separated by 20 ms, impacts a different part of the wheel), this may be a tolerable temperature rise. It is below the melting point of Ti-6%Al-4%V (1600°C), although shock waves created by the temperature changes may be an issue, as it is in the ILC collimators [73].

However, the divergence of the photon beam will decrease with increasing electron beam energy. At 1.5 TeV, the spot size radius could be ten times smaller than at 150 GeV. In that case, the peak temperature rise could be more than 60,000°C. This is clearly not practical. However, there are a number of possible solutions. One might be to use a liquid metal target, although this technology is still at the R&D stage. Another possibility might be to steer the electron beam between sections of undulator, so that the photon beam from each section of undulator is directed at a slightly different location of the target. In that case, the total radiation beam could be spread over a similar area to the case of ILC. The size and divergence of the positron beam at the exit of the target would still be dominated by scattering within the target, so there should be relatively little impact on the overall yield.

It may also be possible to reduce the energy deposition in the target by optimising the thickness. A thicker target will increase the yield (see Fig. 4.7). This would allow a reduction in the undulator length, and hence a reduction in the photon beam power. The fraction of photon beam power deposited in the target would increase, but the energy would be spread over a larger volume (the volume would increase roughly in proportion to the thickness). Overall, there should be a net benefit. However, we see in Fig. 4.7 that above a thickness of about 10 mm, the yield increases relatively slowly with

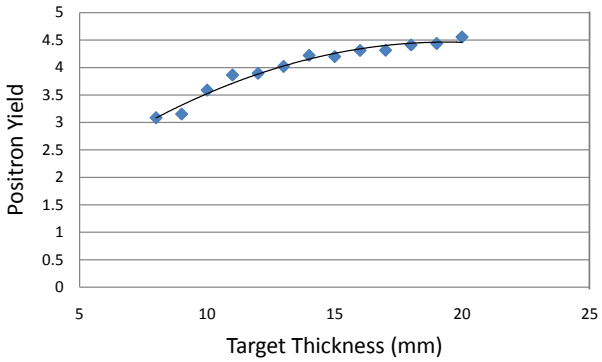

Figure 4.7: Positron yield as a function of target thickness in CLIC Stage 1.

the target thickness. Therefore, it seems unlikely that increasing the target thickness would allow any significant reduction in the temperature rise that would occur in the target.

To demonstrate that the target can survive the energy deposition of a single pulse of the photon beam in CLIC, for the case of an electron beam energy of 150 GeV (ILC undulator parameters), 250 GeV or 1.5 TeV (CLIC Stage 1 and Stage 2 parameters shown in Table 4.2) would require further work. However, if we assume that the target can survive, then the different time structure in CLIC provides an advantage over that in ILC. This is because the target could be rotated at relatively low speed: a very high speed of rotation provides no additional benefit. Then, the eddy currents induced in the target by its rotation in the strong magnetic field of the matching device will be less; and the power deposition and braking forces from the eddy currents should not be as much of a problem.

4.5 Matching Device

We have seen that for ILC, a matching device is required after the positron target, so that the phase space distribution of the positrons becomes correctly matched to the solenoid focusing field in the first accelerating section [74]. Immediately after the target, the positron beam has a small size but large divergence. In the accelerating section, it can have a relatively large size, but should have a small divergence. A matching device transforms the phase space distribution from the target so that it is appropriate for the solenoid focusing field in the accelerating section: this reduces the

overall loss of positrons following the target. A number of different types of matching device are possible, including: an adiabatic matching device (AMD) in which a solenoid field varies smoothly from the target to the first RF structure with a length of 10's of centimeter; and a quarter-wave transformer, in which the field changes in a step at an appropriate distance from the target. For ILC, we looked in detail at the effects of an adiabatic matching device. We will consider the same type of matching device for CLIC.

In an AMD, the longitudinal magnetic field varies with longitudinal distance z from the target according to:

$$B(z) = \frac{B_0}{1 + gz}, \tag{4.5}$$

where B_0 is the initial field at the target, and g is the taper parameter. Generally, the taper parameter should be small enough so that the "adiabatic condition" is satisfied:

$$\frac{gP}{eB_0} \ll 1, \tag{4.6}$$

where P is the particle momentum.

The key parameters for the AMD are the initial field B_0, the value of the taper parameter g, and the physical aperture. Because the positrons from the target have a very wide energy spread, it is not possible to achieve a perfect match between the target and the solenoid in the linac for all the positrons in the beam. Optimisation of the parameters to achieve a low rate of lost positrons (i.e. a good transfer efficiency) is best done by simulation. Tracking studies can also be used to investigate the effect of the AMD on the polarisation of the beam, although the impact is expected to be small because the polarisation is predominantly in the longitudinal direction.

Fig. 4.8 shows the transfer efficiency in CLIC Stage 1 (parameters shown in Table 4.2) as a function of initial field strength and taper parameter. Over a range from $10\,\mathrm{m}^{-1}$ to $60\,\mathrm{m}^{-1}$, there is a weak dependence on the taper parameter. A value of approximately $30\,\mathrm{m}^{-1}$ seems appropriate, from point of view of performance and engineering considerations [75].

There is a much stronger dependence on the initial magnetic field. If the field is increased from 1 T to 6 T, then the capture efficiency is improved from 30% to 75% (with taper parameter $30\,\mathrm{m}^{-1}$). The higher magnetic field gives a smaller cyclotron radius for positrons moving through the AMD, resulting in fewer losses. Although a

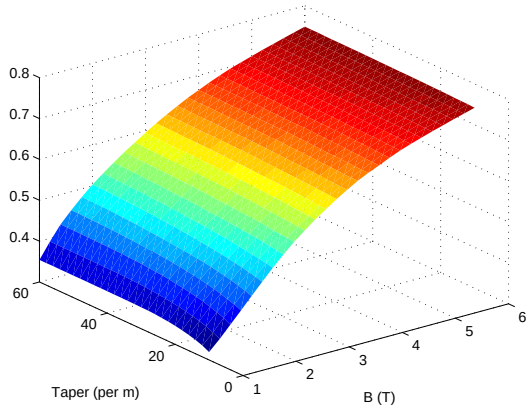

Figure 4.8: Transfer efficiency in an AMD for CLIC Stage 1 (250 GeV electron beam energy in the undulator) as a function of initial magnetic field strength and taper parameter.

higher magnetic field could give a higher transfer efficiency, a 6 T field is close to the engineering limit.

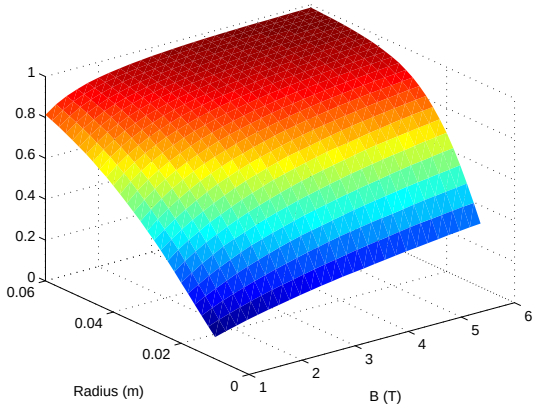

Figure 4.9: Transfer efficiency in an AMD for CLIC Stage 1 (250 GeV electron beam energy in the undulator) as a function of initial magnetic field strength and aperture radius.

Fig. 4.9 shows the transfer efficiency in CLIC Stage 1 (250 GeV electron beam in the undulator, parameters shown in Table 4.2) as a function of initial field strength and aperture. For all field strengths, there is a strong dependence on aperture. For a 6 T initial field, the transfer efficiency increases from 30% to close to 100%, as the aperture

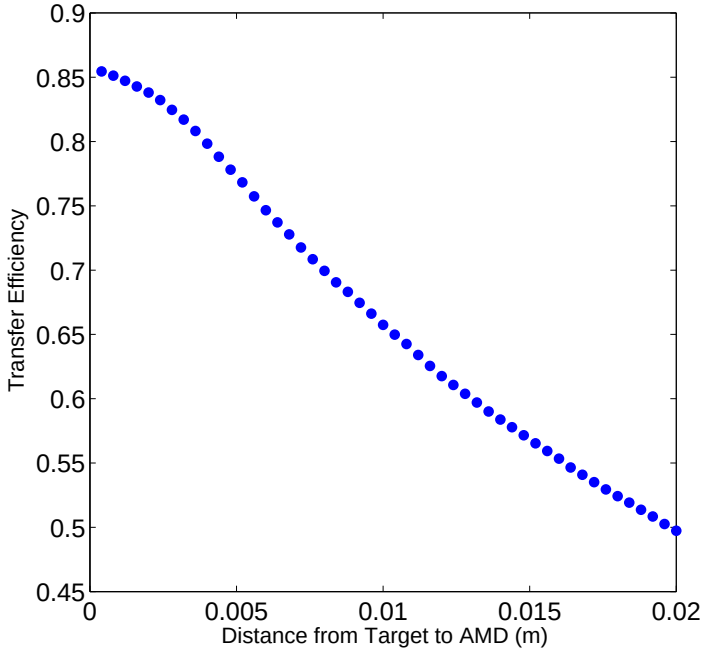

Figure 4.10: Positron transfer efficiency in an AMD as a function of the size of the gap from the target to the entrance of the matching device, using CLIC Stage 1 parameters (250 GeV electron beam in the undulator).

increases from 1 cm to 6 cm. Again, there are engineering limitations on the aperture: about 3 cm is realistic.

As mentioned above, the time structure of CLIC allows for a slow rotation speed of the target. This means that the target can be immersed in a strong magnetic field without strong effects from eddy currents. However, we can look at the effect of a gap between the target and the AMD on the capture efficiency. Fig. 4.10 shows the transfer efficiency as a function of the distance between the target and the AMD, for CLIC Stage 1 (250 GeV electron beam energy in the undulator). We can see that the transfer efficiency could reach 85% when there is only a small gap of 0.4 mm or less. However, a larger gap leads to a reduced transfer efficiency. At the point where the gap is 2 cm, the positron transfer efficiency will be reduced to 50%. It is clearly of benefit to have the target immersed in the field of the AMD, to eliminate any gap between the target and the AMD.

4.6 Conclusion

In this chapter, we have considered the use of an undulator-based positron source for CLIC. The different stages of CLIC operation, initially at 500 GeV centre of mass collision energy, and then at 1.5 TeV centre of mass collision energy, leads to a number of possibilities for the positron source configuration. The simplest option would be to locate the positron source so that the undulator operates with 150 GeV electron beam energy in both Stage 1 and Stage 2. This would mean that a positron source very similar to that planned for ILC could be used: the undulator parameters, photon collimator, target, and matching device could all have essentially the same parameters as in ILC. There would be two main differences, both arising ultimately from the different time structure of the beam in CLIC, compared to ILC.

1. CLIC will have a positron pre-damping ring with a much larger acceptance than the ILC damping rings. This means that a shorter undulator could be used for CLIC compared to ILC, producing the same positron yield (positrons per electron).

2. The target wheel in CLIC will not need to rotate so quickly as in ILC. The energy deposition per machine pulse in CLIC will be larger than in ILC, leading to peak temperature rises of several hundred degrees Celsius. The pulse length in CLIC is so short that rotating the target, even at quite high speed, will be of little benefit in spreading the energy deposition. The temperature rise in the target is an issue for CLIC. However, the low speed of rotation of the target wheel would mean that there would not be issues with eddy currents from the strong magnetic field of the matching device.

However, operating the undulator with an electron beam energy of 150 GeV at both Stage 1 and Stage 2 in CLIC would mean relocating the entire positron source during the upgrade. We have considered the possibility of keeping the source at the same physical location. This would reduce the amount of work needed in the upgrade from Stage 1 to Stage 2. However, there would be an increase in electron beam energy of 1.25 TeV in the undulator after the upgrade. In the case that the undulator is located at the end of the electron linac, the beam energy would increase from 250 GeV to 1.5 TeV. It would not be possible to use the same undulator in both Stage 1 and

Stage 2. However, we have seen that by taking advantage of the large acceptance of the CLIC pre-damping ring, it is possible to find undulator parameters (with larger period, and larger deflection parameter, but smaller magnetic field) that would allow the components of the positron source to remain in the same location in Stage 2, as in Stage 1. In principle, only the undulator would need to be replaced. The undulator in Stage 2 would need to be significantly longer than the undulator in Stage 1; however, the overall length would still likely be less than that needed for ILC.

Although it seems feasible to operate an undulator-based positron source with an electron beam energy of 1.5 TeV, there are a number of issues and disadvantages:

1. To achieve the necessary yield with an undulator of reasonable length, positrons over a large range of energies and angles must be captured. This is possible with the large acceptance of the pre-damping ring; however, there will be little or no polarisation of the positron beam.

2. The photon beam divergence will be extremely small, so it will be difficult or impossible to improve the polarisation by collimating the beam.

3. The photon beam spot size on the target will be very small, because of the small photon beam divergence. This means that the energy deposited by the photon beam in the target will be deposited in a very small volume. Without some method to spread the energy over a larger volume, the temperature rise will be above the melting point of the target material.

Regarding the polarisation, it may be possible to consider an upgrade not in two stages, but in three. Stage 1 would provide 500 GeV centre of mass collision energy, with about 25% positron polarisation, using a positron source similar to ILC, but with the undulator at the end of the electron linac (250 GeV). In Stage 2, when the collision energy is increased to 1.5 TeV, the undulator would be replaced, but the other components and location of the positron source would remain the same. Although the positron beam would not be polarised, the amount of work on the positron source needed during the upgrade (on construction and recommissioning) would be reduced, compared to re-locating the positron source. Finally, if positron polarisation is required, then there could be a Stage 3, in which the original (Stage 1) undulator is installed in the electron linac at the 150 GeV point, and the other components of the positron source are relocated accordingly.

Although there remains a lot of detailed study and design work to be done, it appears that an undulator-based positron source could be a realistic option for CLIC, with several options regarding upgrades.

5

Target Wheel Studies

5.1 Motivation and Goal of Target Experiment

In Chapter 3 we introduced the undulator-based positron source for ILC. One of the most important components is the positron production target. 10 MeV photons that are generated from the 147 m undulator will strike the target to produce electron and positron pairs. Because of the large pulse population and the long pulse length, the target needs to be rotated to reduce the average energy deposition per unit volume. The ILC positron production target has been designed as a wheel with 1 m diameter. The target rim is connected to the drive shaft by five equally spaced radial struts. The energy deposited in the target rim can effectively be reduced by rotating the target at a speed of a few thousand revolutions per minute. Positrons generated from the target have a large divergence angle; therefore, they need to be focused – the phase space needs to be properly matched to the focusing solenoid in the first acceleration section. Otherwise, many positrons will be lost by hitting the beam pipe or other components, causing damage. Hence, installing a matching device after the target could help to increase the capture efficiency to more than 40% [76].

The positron yield could be substantially improved if the target is (at least partially) immersed in the magnetic field of the matching device. However, immersing the target in a strong magnetic field leads to significant issues with eddy currents, arising from the rapid rotation of the target wheel. The eddy currents will generate heat, and provide a force acting against the target movement [77]. Research related to the positron production target, including studies of the effects of eddy currents, has been carried

out worldwide. Detailed modelling of the eddy currents is sufficiently complex that there is significant uncertainty in the results of simulations [78]. In order to benchmark the simulations, and provide a solid basis for understanding the issues and optimising the design, experimental studies are necessary. Such studies have been performed at Daresbury Laboratory, using a full-scale prototype of the ILC target wheel [79].

The main goal of the experiment was to investigate the mechanical and thermal issues associated with rotating the wheel in a strong magnetic field. It has not been possible (and there was never any intention) to test the prototype target wheel for actual positron production. Although some aspects of the design have been simplified (for example, there are no cooling channels incorporated in the wheel), all relevant features for determining the eddy current effects are present [80]. The experiment is designed to allow measurement of the magnetic field, torque on the wheel, and temperature of the wheel, at different rotation speeds, magnetic fields strengths, and depths of immersion in the magnetic field. By comparing experimental data with simulation results, the aim is to benchmark the simulation codes and allow optimisation of the design to reduce the effects of eddy currents, as necessary.

In this chapter, we will introduce the construction of the target wheel prototype, and the overall design of the experiment, including the instruments used for measuring the magnetic field, the torque, and the temperature of the wheel. We will then discuss the predictions (from simple analytical models and simulations) of the torque and the temperature rise from eddy currents. We will then present experimental results, and compare these with the predictions from the analytical models and simulations.

5.2 Experiment Design

5.2.1 Target Construction

The target wheel prototype is the same design and same size (1 m diameter) as the present design for the ILC positron target wheel. The material is Ti-6%Al-4%V. During measurements, the prototype target wheel will be partially immersed in the field of a dipole magnet to simulate the effect of a matching device. The field can reach strengths of up to 1 T; this is less than the field that may be used in a matching device (which may be up to 6 T), but is sufficient to allow benchmarking of the simulations. The prototype target wheel could in principle be rotated at up 2000 rpm, giving a rim

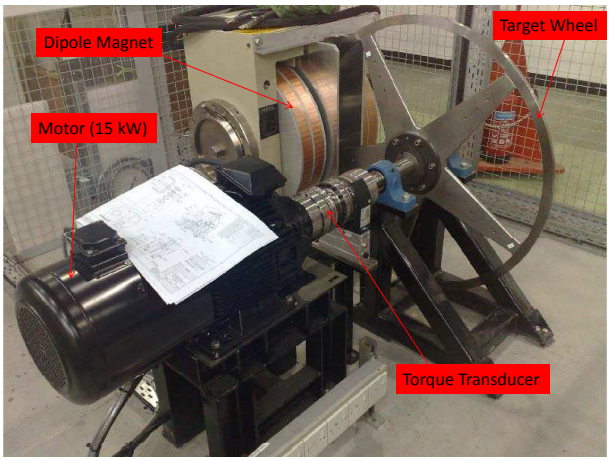

Figure 5.1: Target wheel experiment at Daresbury Laboratory, before installation of the safety cage.

velocity of about 100 m/s; however, for safety reasons, the speed during operation was limited to 1500 rpm. Fig. 5.1 shows the experimental set-up, including target wheel, motor and magnet. At the stage shown in the figure, the installation was nearly complete. After the picture was taken, the target was enclosed in a safety cage, to protect against the consequences of any mechanical failure during rotation of the wheel at high velocity. Visible in the picture is the motor that can provide a power of 15 kW. A torque transducer is incorporated in the shaft connecting the motor with the target wheel. The rim of the prototype target wheel will be partially immersed in a dipole magnetic field, which can have a strength up to 1 T. The field is provided by a magnet with two cylindrical pole caps, with 250 mm diameter. During operation, the gap between the pole caps is 50 mm. The position of the target wheel is fixed; however, the supporting structure of the magnet is adjustable, so the magnet can be moved in the plane of the target wheel. This allows the depth of immersion of the wheel in the magnetic field to be varied over a range of 50 mm.

Fig. 5.2 shows the fully finished target wheel prototype experiment installation. The target wheel and magnet are locked into a yellow cage for safety reasons. Additionally, in the direction of the operator, there are sandbags stacked to human height, just in case of a mechanical failure during operation. There are several interlocks that have been installed in the safety cage. If the cage door is opened or is not closed properly, the power supply to the motor will be cut off, and operation will be terminated immediately.

Figure 5.2: Target wheel experiment at Daresbury Laboratory, enclosed in the safety cage.

In the safety cage, there are two cameras installed so that the operator can remotely monitor the target wheel while it is in rotation. This is an additional safety measure, so that any unusual movement of the target wheel can be seen, and the motor shut down accordingly. Beside the rim of the target wheel, there are two arms holding two infrared thermal cameras directed at the target rim: these cameras provide information on the temperature of the rim. One of the effects of the eddy currents is a heating of the target wheel. Because of the heat expected to be generated, an air cooling system will also be provided for the safety cage. Construction of the experiment was completed in 2009. We will present a summary of the data, including some analysis and comparison with simulations and analytical models, below.

5.2.2 Magnetic Field

As described in the previous section, the production rate of positrons in the ILC positron source can be increased if the production target is immersed in a magnetic field. In the target wheel experiment at Daresbury, it is important to be able to provide a range of field strengths and immersion depths, so as to be able to understand properly the effects of eddy currents generated when the target wheel is rotated at high velocity in the magnetic field. Fig. 5.3 shows an engineering drawing of the cross section of

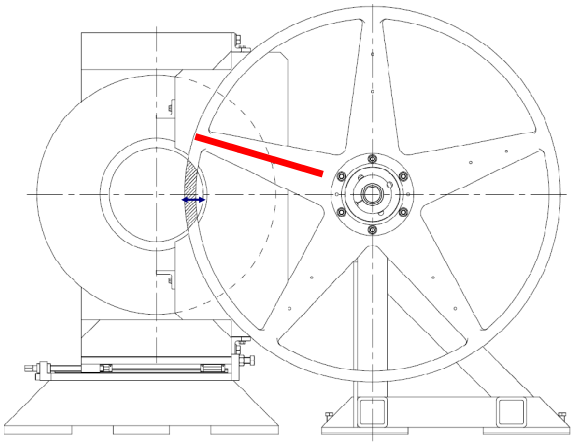

Figure 5.3: View of the target wheel at full immersion in the field of the magnet.

the target wheel, partially immersed in the magnetic field. The immersion depth is adjustable, by moving the magnet in the plane of the wheel. The maximum immersion depth is 50.25 mm. A magnetic field sensor (Hall probe), attached to one strut of the target wheel, can be used to map the field strength seen by a point on the wheel, as a function of angular orientation of the wheel.

The results of magnetic field measurement, with a peak field strength of 0.48 T are shown in Fig. 5.4. There are four different immersion depths shown, 20.25 mm, 30.25 mm, 40.25 mm and 50.25 mm. In each case we see a large fringe field, with relatively slow increase and decrease of the field strength. The width of the region of constant field (essentially, the region within which the magnetic field sensor is directly between the poles) varies with immersion depth, with the deepest immersion showing the largest constant field region. As we shall see later, the fringe field plays a significant role in the generation of a torque opposing the rotation of the wheel.

Fig. 5.5 shows field strength measurements with constant immersion depth, but different currents in the coils of the magnet. The width of the constant field region, and of the fringe field, is roughly the same each time; however, as expected, the strength of the peak field varies. The peak field, with a current of 100 A in the coils, is 1.42 T.

The results of the experimental measurements of the field have been compared with calculations using the 3D FEA code Opera, and found to be in good agreement. Fig. 5.6 [81] shows a comparison between the magnetic field measurements and two different

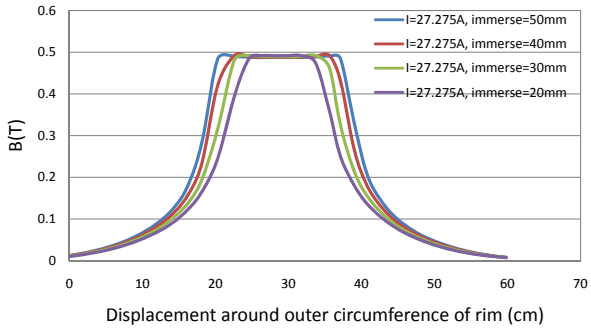

Figure 5.4: Field mapping obtained with Hall probe attached to the wheel rim. There is a constant current in the coils of the magnet, but the position of the magnet is varied to provide different immersion depths (corresponding to the different colour lines) of the target wheel.

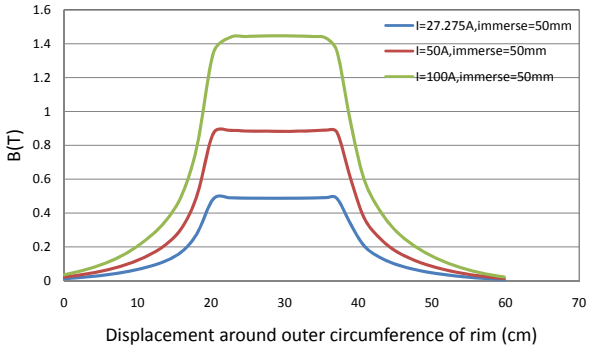

Figure 5.5: Field mapping obtained with Hall probe attached to the wheel rim. The immersion depth is constant, but different currents (corresponding to the different colour lines) in the coils of the magnet are used.

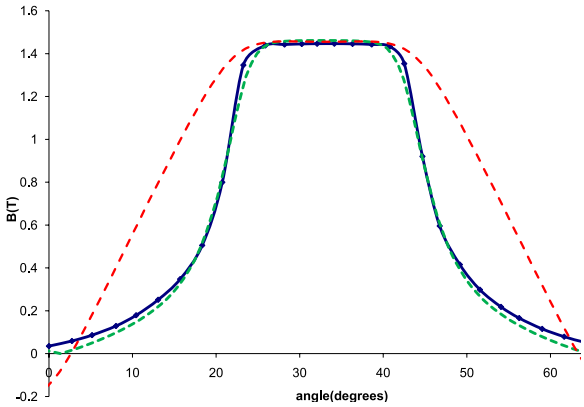

Figure 5.6: The magnetic field strength as a function of the angle around target rim from an arbitrary zero position. The measured values are shown in blue; the air-core model is shown in red dashes, and the steel-core model is shown in green dots.

models of the magnet: one with a steel core, and one with an air core. The current in the coils in this case was 100 A, and the immersion depth was 50.25 mm. There is reasonably good agreement between the measured values and the OPERA results using the steel core magnet model.

5.2.3 Instrumentation

There are several instruments used in the experiments for data collection.

1. The torque transducer [82] is incorporated in the shaft linking the drive motor to the target wheel. The torque transducer provides important data on the force required to keep the wheel rotating at a given velocity: the "braking force" as a function of magnetic field and rotational velocity is a key characteristic of the eddy currents.

2. The infrared thermal camera is the main tool for measuring the thermal condition of the target rim. Before installation in the experiment itself, the camera was calibrated against a thermometer and another thermal camera (with megapixel resolution), using a piece of material of the same composition as the target wheel. During the operational stage, only the infrared thermal camera was placed in the cage. The temperature changes are another important characteristic of the eddy currents.

3. The magnetic field sensor (Hall probe) is attached to a spoke of the target wheel, close to the outer edge of the rim. By manually rotating the wheel so that the sensor passes through the magnetic field, the field as a function of orientation of the wheel can be determined. The shape of this curve is an important factor in determining the size and effect of the eddy currents.

5.3 Models and Predictions

5.3.1 Analytical Model

Although the prototype target wheel is the same size and shape as the present design for the ILC positron source, the field produced by the magnet cannot reach the levels that may be used in a matching device. Therefore, it is not possible to make measurements of the eddy current effects in the exact conditions that the real target wheel would experience. It is necessary to use simulations to predict the effects: the goal of the experiments using the prototype target wheel is to validate the simulations.

Before discussing the simulations, we develop an analytical model of the system. Although some simplifications are necessary, this will give us an appreciation of the physics, and allow us to judge whether the results from the simulations are reasonable. The problem will be formulated as follows. We consider an infinitely long metal bar, with rectangular cross-section, moving at constant velocity v through a magnetic field. The direction of motion is parallel to the (infinite) length of the bar. The magnetic field is perpendicular to the direction of motion, but the strength varies as a function of position. The situation is illustrated in Fig. 5.7. We choose axes so that the bar is moving in the z direction, and the magnetic field is in the x direction. The edges of the bar are parallel to the x and y axes; let the lengths of the edges in the x and y directions be a_x and a_y, respectively.

The bar represents the rim of the target wheel. The model neglects effects associated with the fact that the motion is circular, i.e. that different points on the rim are actually moving in different directions, and have some acceleration. However, if the radius of the wheel is large compared to the cross-sectional dimensions of the rim, and compared to the extent of the magnetic field, then these effects should be small. Our goal is to calculate the eddy currents generated in the bar in this model, and then to find the resulting force on the bar. In the case of the target wheel, this force, multiplied by the

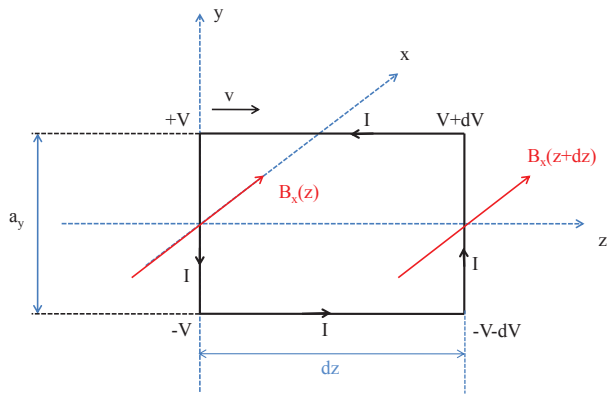

Figure 5.7: Simplified model of the target wheel moving in a magnetic field, allowing analytical calculation of the eddy currents and the resulting forces.

radius of the wheel, gives the decelerating torque on the target wheel arising from the eddy currents.

In the simple model shown in Fig. 5.7, a voltage is induced in the y direction from the motion of the metal bar through the magnetic field. Consider a short section of the bar of length dz. If the field strength varies as a function of z, then the induced voltage will also vary as a function of z. Referring to the voltages shown in Fig. 5.7:

$$2V = v\,(B_x)_z\,a_y, \tag{5.1}$$

$$2(V+dV) = v\,(B_x)_{z+dz}\,a_y. \tag{5.2}$$

Thus, the voltage difference between two points with the same x coordinate, and with $y = a_y$, but with a (small) separation dz between the z coordinates, will be:

$$dV = \frac{1}{2} v \frac{dB_x}{dz}\,dz\,a_y. \tag{5.3}$$

The difference in voltage leads to a current flow in the metal bar, in the z direction. Since the voltage varies linearly with y, the current density J as a function of y is given by:

$$J(y) = \sigma \frac{dV}{dz}\frac{y}{a_y/2} = \sigma v \frac{dB_x}{dz}\,y, \tag{5.4}$$

where σ is the conductivity of the material. Then the total current dI in a thin slice of the bar of height dy and extending across the full width a_x of the bar is:

$$dI(y) = J(y) a_x\,dy = \sigma v \frac{dB_x}{dz}\,a_x y\,dy. \tag{5.5}$$

If we imagine closing a current loop with current flowing parallel (or anti-parallel) to the y axis, then there will be a force on the section of the bar, resulting from the field acting on the induced current:

$$d^2F_z = (B_x)_z \, dI(y)2y - (B_x)_{z+dz} \, dI(y)2y = -2\frac{dB_x}{dz} dI(y)y \, dz. \tag{5.6}$$

Substituting from Eq. (5.5) gives:

$$d^2F_z = -2\sigma v \left(\frac{dB_x}{dz}\right)^2 a_x y^2 \, dy \, dz. \tag{5.7}$$

The total force on the section of the bar of length dz is found by summing over the force generated by currents at all positions of the bar:

$$dF_z = -2\sigma v \left(\frac{dB_x}{dz}\right)^2 a_x \, dz \int_0^{a_y/2} y^2 \, dy = -\frac{1}{12}\sigma v \left(\frac{dB_x}{dz}\right)^2 a_x a_y^3 \, dz. \tag{5.8}$$

The total force on the bar is obtained by integrating over the entire length of the bar:

$$F_z = -\frac{1}{12}\sigma v \, a_x a_y^3 \int \left(\frac{dB_x}{dz}\right)^2 dz. \tag{5.9}$$

We have assumed that the field is uniform in the x and y directions. However, we can generalise the expression for the total force by incorporating the factor a_x and one of the factors of a_y into the integral, which then becomes a volume integral:

$$F_z = -\frac{1}{12}\sigma v \, a_y^2 \int \left(\frac{dB_x}{dz}\right)^2 dV. \tag{5.10}$$

Notice that the force is in the direction opposite to the velocity of the bar: the currents induced by the motion of the bar in the magnetic field act against the motion of the bar. Also notice that the force depends on the square of the derivative of the field along the direction of motion. In a uniform field, there is no force. This is why the fringe field in the target wheel experiment is important. The size of the force also depends on the conductivity of the material (a non-conductor will experience no force, as we would expect) and on the velocity [83].

The power required to keep the bar in motion at constant velocity is readily found from the braking force:

$$P = -v \, F_z = \frac{1}{12}\sigma v^2 \, a_y^2 \int \left(\frac{dB_x}{dz}\right)^2 dV. \tag{5.11}$$

This is also equal to the power dissipated in the eddy currents, as may be shown by calculating the ohmic losses directly.

Finally, for the case of a rotating wheel of radius r, the torque required to keep the wheel rotating at constant angular frequency $\omega = v/r$ is given by:

$$\tau = -r\,F_z = \frac{1}{12}\sigma\omega r^2\,a_y^2 \int \left(\frac{dB_x}{dz}\right)^2 dV. \tag{5.12}$$

Notice that the torque has a strong dependence on the size of the rim: assuming that the rim is fully immersed in the field, and that the field is approximately uniform in the radial direction, the torque varies as the cube of the width of the rim (i.e. $\tau \propto a_y^3$). In the case of the target wheel, the rim is connected to the drive shaft by five spokes. At each spoke, the value of a_y is large compared to the value where there is no spoke. Therefore, although each spoke is quite thin, the spokes may make a significant contribution to the total (average) torque. If we estimate the torque using Eq. (5.12) neglecting the spokes, then we expect that we will underestimate the true value.

Nevertheless, let us apply the above results to our positron target prototype, to give some feeling for the values we might expect for the torque and the power dissipation from the eddy currents. The material Ti-6%Al-4%V has a conductivity of $5.8 \times 10^6\,\Omega^{-1}\mathrm{m}^{-1}$. The target rim width a_y is approximately 30 mm, and target rim thickness a_x is equal to 15.6 mm. Let us consider the "worst" case: revolution frequency of 2000 rpm (rim velocity approximately 100 m/s); peak field of 1.45 T, and immersion depth of 50.25 mm. In this case, performing the integral under the derivative of the curve shown in Fig. 5.6 gives:

$$\int \left(\frac{dB_x}{dz}\right)^2 dV \approx 0.019\,\mathrm{T}^2\mathrm{m}. \tag{5.13}$$

Then we find that the torque is approximately 43 Nm, and the power dissipated is approximately 9 kW.

5.3.2 Simulation Results from ANL

A more detailed simulation model has been developed by researchers at Argonne National Laboratory (ANL). The parameters used in the simulation (specifically, the target wheel dimensions, and field profile) are close to the values for the target wheel experiments at Daresbury: the rim width used was 30 mm (the same as for the prototype),

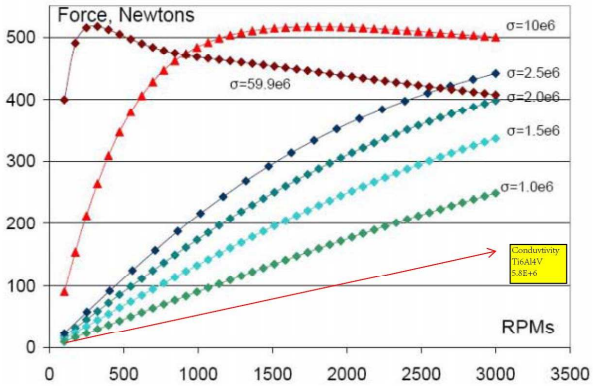

Figure 5.8: Stopping force as a function of rotation frequency for different conductivities, from ANL simulations [84]. For titanium alloy Ti-6%Al-4%V, the conductivity is $5.8 \times 10^5\,\Omega^{-1}\mathrm{m}^{-1}$.

and thickness was 14 mm (15.6 mm in the prototype). The peak field was 1.5 T; the magnetic poles had 25 mm diameter, and separation 50 mm. The immersion depth was about 50 mm. Some simulations have been done in ANL, the results giving the braking force as a function of rotation frequency and conductivity are shown in Fig. 5.8 which has been discussed into detials in paper [84],

We can see that for a reasonably small conductivity, the stopping force roughly follows a linear relationship to the rotating speed. At high velocities or conductivities, rotational effects become important. Also, the eddy currents generated by the motion of the wheel in the external magnetic field generate their own magnetic field, which acts to reduce the overall strength of the field within the wheel. In effect, the "skin depth" (the depth to which the external field penetrates the target) starts to become small compared to the dimensions of the wheel; at this point, the force required to keep the wheel turning stops increasing with frequency, and can even reduce with increasing frequency. Our simple model neglects these effects, and just predicts a simple linear relationship between force and frequency. For our target prototype, the material is Ti-6%Al-4%V, which has a conductivity of $5.8 \times 10^5\,\Omega^{-1}\mathrm{m}^{-1}$. Up to 3000 rpm we expect that with this conductivity, the relationship between force and rotational velocity will be, to a good approximation, linear. Although the ANL results do not include the case for a conductivity $5.8 \times 10^5\,\Omega^{-1}\mathrm{m}^{-1}$ and rotational velocity 2000 rpm, we can make a linear interpolation from the graph. We find that the torque predicted by the

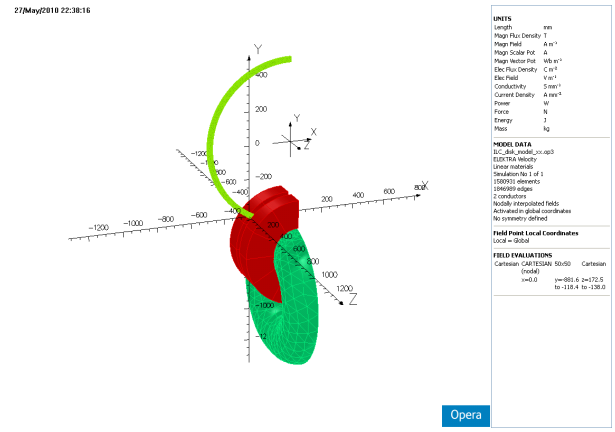

Figure 5.9: Model of the target wheel experiment constructed in Opera.

simulations is around 50 Nm, which is of the same order of magnitude as the value of 43 Nm predicted by our simple analytical model.

5.3.3 Opera Model

The forces on the target wheel rotating in a magnetic field can also be calculated using the commercial 3D FEA code Opera. Fig. 5.9 shows the model of the target wheel experiment constructed in Opera. The magnetic field is produced by a steel core, which placed in the middle of the red coils. The thin green ring represents the target rim. In this model, only the target rim has been included, and there are no spokes. The model can be used to simulate various aspects of the experiment. For example, we have already shown (in Fig. 5.6) a comparison between the magnetic field distribution predicted from this model, and the distribution found in our experimental measurements. However, the model can also be used to calculate the torque on the target wheel when it rotates at a given velocity within the field. Generally, we find that the results are in reasonable agreement with the analytical model. The results from Opera are presented in more detail below, when they are compared with the experimental results.

5.4 Experimental Results

5.4.1 Preliminary Tests

The torque transducer incorporated in the drive shaft connecting the motor with the target wheel records both the torque applied to the target wheel from the motor, and the speed of rotation of the target wheel. Altogether, there are four channels returning data from the torque transducer: Torque 1 (returning torque values at a rate of 2400 Hz); Torque 2 (torque values at a rate of 600 Hz); Angle; and Speed. Data can be recorded over a maximum time period of 180 s. During the initial test runs, the magnet was kept turned off.

With the motor turned off and the wheel stationary (and with zero current in the magnet coils), the torque transducer still returns non-zero values for the torque. These values indicate the noise level, which is of order 1 Nm.

Fig. 5.10 shows the results of a typical test run, with the torque and speed recorded over a period of 60 s. Initially, the motor controller was set to drive the wheel at a nominal speed of 33 rpm. After about 28 s, the motor was switched off, so the wheel slowed to a stop; after a further few seconds, the motor was switched on again, and the wheel was driven at a nominal rate of 15 rpm. We see that while the speed of the wheel was set at 33 rpm, the torque fluctuated between +4 Nm and -4 Nm. Also, the speed of 33 rpm was not actually achieved: instead, the speed fluctuated between about 29 rpm and 30 rpm. The reasons for this are not clear. At the moment the motor was switched off, there was a peak in the torque of -8 Nm, from the inertia of the wheel driving the motor. While the wheel was stationary, there was a small level of noise on the torque data. There was a peak (of about 4 Nm) in the torque as the motor was re-started; then there was again a fluctutation in the torque data, but between lower limits than before, corresponding to the lower speed of rotation of the wheel.

From the speed and torque data returned by the torque transducer, it is easy to calculate the power required to keep the wheel in motion. For example, in the test run shown in Fig. 5.10, with the speed of the wheel at a (nearly) steady value of about 30 rpm, the maximum torque value was about 4 Nm: therefore, the maximum power needed to keep the wheel in motion was about 12.6 W.

Note that when changing the speed of the motor, the rate of acceleration or deceleration can be specified. Although an “instantaneous” stop command can be issued, in

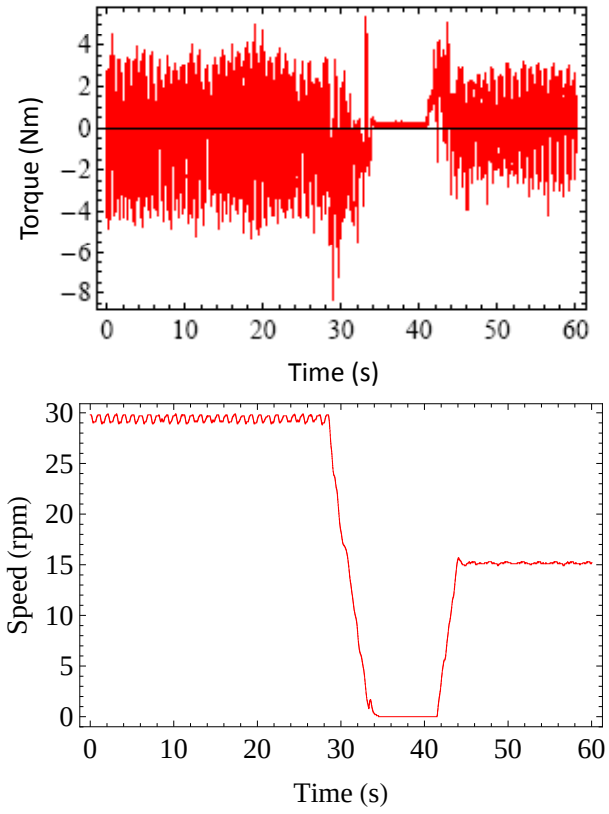

Figure 5.10: Data from torque transducer channel Torque 1 (top) showing the target wheel rotating with nominal speed set at 33 rpm; then stopping for a few seconds; and then finally restarting and accelerating to a speed of 15 rpm. The bottom plot shows simultaneous data from the torque transducer Speed channel.

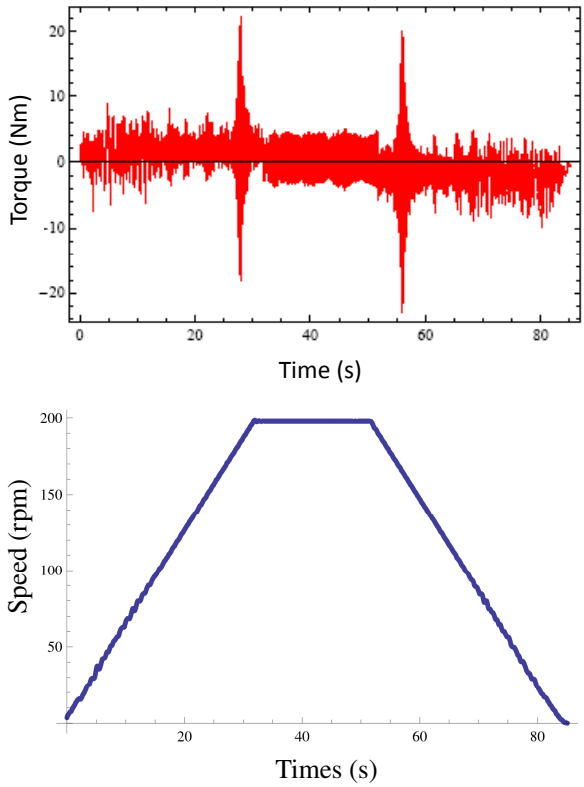

Figure 5.11: Data from torque transducer showing the target wheel accelerating from rest to a speed of 198 rpm; maintaining this speed for about 20 seconds; and then finally decelerating to rest. The top plot shows the torque; the bottom plot shows the speed.

practice this would be dangerous if the wheel were rotating at high speed, with possible damage being caused to the torque transducer or the motor.

The low-speed tests showed that the system behaved qualitatively as expected; however, we found that the rotation speed of the wheel did not necessarily match the speed set for the motor controller. Some regular oscillations in the speed were visible in the measurements from the torque transducer. Also, the torque values returned by the torque transducer showed large, rapid fluctuations, which needed to be averaged out to obtain meaningful values to compare with theoretical predictions.

Further tests were carried out with the wheel rotating at a higher speed. Fig. 5.11 shows results from a test in which the wheel was accelerated to 198 rpm, maintained at that speed for about 20 seconds, then decelerated to a stop. During the early stage of the acceleration, the torque reached a maximum value of about 8 Nm. However, as the

wheel reached a speed of 174 rpm, there was a peak in the torque (which reached more than 20 Nm), before the torque returned to a similar level as during the early part of the acceleration. Similar behaviour was observed during deceleration, with a similar peak in the torque at the same speed of 174 rpm.

Note that although there are still clearly large fluctuations in the torque readings, the average value is clearly positive during acceleration and steady rotation, and negative during deceleration.

In order to confirm the large value reached by the torque at 174 rpm, the motor controller was programmed to accelerate the wheel to this speed, maintain the same speed for a period of about 18 seconds, then decelerate the wheel to a stop. The torque data collected during this run are shown in Fig. 5.12. We see that the torque reaches an even higher value than before, about 30 Nm. This is about four times larger than the usual value reached during acceleration up to 198 rpm. Although the reasons for the large increase in the torque at the particular speed of 174 Nm are not fully understood, the increase is reproducible, and likely to be the result of a mechanical resonance. A more detailed model of the system, including many aspects of the motor and drive shaft as well as the wheel itself, would be needed in order to understand the resonance properly. However, this would be very difficult to do because of the complexity (for example) of the motor, and predictions of such resonances from a mechanical model would likely not be very reliable. This issue is of some potential concern for the ILC positron production target, since if a strong resonance occurred close to the nominal operating speed of 2000 rpm, it is possible that some damage could occur to the system. In the case of the experiments described here, it was important to monitor the torque data closely, and avoid operating for any length of time at speeds where resonances were observed.

5.4.2 Torque Measurements

After a number of test runs at low speed (up to 200 rpm), torque data were collected over a range of speeds up to 1500 rpm, for various magnetic field strengths and depths of immersion of the target in the magnetic field. Although the speed of the wheel was limited in the experiments to 1500 rpm for safety reasons, the nominal operating speed of the target wheel in the ILC positron source is 2000 rpm. Therefore, the results shown here include an extrapolation to 2000 rpm.

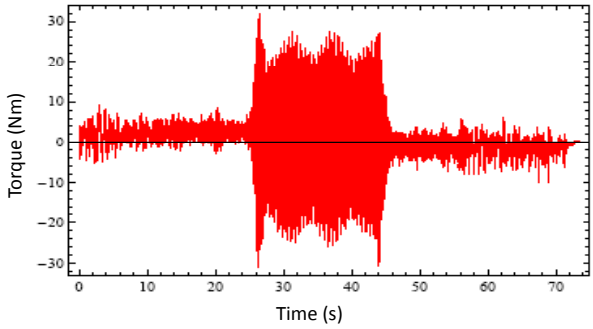

Figure 5.12: Data from torque transducer showing the torque as the target wheel is accelerated from rest to a speed of 174 rpm; maintained at this speed for about 18 seconds; and then finally decelerated to rest.

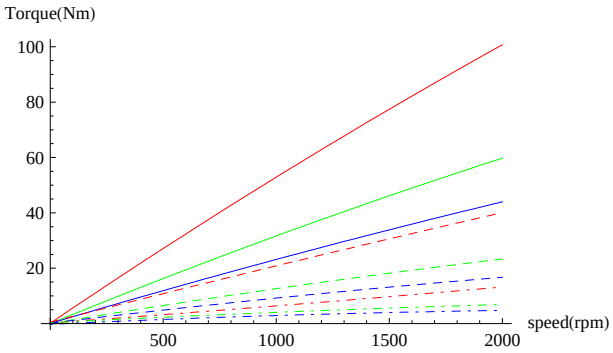

Figure 5.13: Torque as a function of rotation speed for different immersion depths and magnetic field strengths. Red, green and blue lines show immersion depths 50.25 mm, 30.25 mm and 20.25 mm, respectively. Solid, dashed, and dot-dashed lines show magnet currents 100 A (1.44 T peak field), 50 A (0.9 T) and 27.275 A (0.485 T) respectively.

Fig. 5.13 shows the torque as a function of rotation speed for a range of field strengths and immersion depths. The solid lines show the results with a magnet current of 100 A, corresponding to a peak magnetic field of 1.44 T; the dashed lines show the results with 50 A magnet current (0.9 T peak field); and the dot-dashed lines show the results with 27.275 A (0.485 T). The red, green and blue lines in each case show immersion depths of 50.25 mm, 30.25 mm and 20.25 mm, respectively. We see that there is a (close to) linear relationship between torque and rotation speed, as expected from the simple theoretical model, and the simulations. Also, the torque increases with field strength and with immersion depth.

From the results, we can calculate the power dissipation in the wheel. If we extrap-

olate to 2000 rpm, then at the highest field and immersion depth, the power dissipation would be 21 kW. This is significantly larger than the value of 9 kW expected from our theoretical model. The reason is that the torque is larger than expected either from theory or from simulations. This becomes clear if we make a more detailed comparison between the theoretical and experimental results.

5.4.3 Torque Data: Comparison with Models

Fig. 5.14 shows the torque as a function of rotation speed when the target is immersed at a depth of 50.25 mm in a magnetic field of peak strength 0.485 T. The blue line represents the experimental data; the red dots show the calculation results based on the analytical model developed in Section 5.3.1; and the blue dots are the simulation results from Opera (Section 5.3.3). Note that the analytical model is applied in the form (from Eq. (5.12)):

$$\tau = \frac{1}{12}\sigma\omega r^2\, a_x a_y^3 \int \left(\frac{dB_x}{dz}\right)^2 dz, \tag{5.14}$$

where z is the distance around the rim, a_x the thickness of the wheel, and a_y the width of the rim (the difference in radius between the inner surface and outer surface of the rim). Note that the model omits the spokes where there is (locally) a large value of a_y, though there is a strong dependence on a_y in the formula.

From Fig. 5.14 we see that the torque obtained from the experiment is more than three times larger than calculated from either the analytical model or from the Opera simulation. The analytical model and Opera simulation are in reasonable, though not exact, agreement. One possible reason for the difference between the experimental results and the analytical or simulation results, is the geometry of the target wheel. In both the analytical model and the Opera simulation, we included only the target rim, and not the spokes. Because of the strong dependence on a_y, a complete geometry with five spokes included will lead to a higher eddy current, and so a larger torque.

Ideally, we should implement the complete geometry into the Opera simulations. Unfortunately, this would require use of the Carmen module in Opera, for which we do not have access to a licence. Therefore, we explore the dependence on the rim width by considering a modified target wheel geometry in which the spokes are still excluded, but we consider increasing the width of the rim by 50%, from 30 mm to 45 mm. The

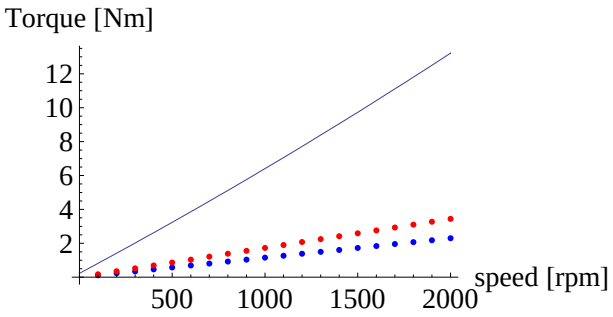

Figure 5.14: Comparison between experimentally measured torque (solid line), analytical estimate (red dots) and Opera simulation (blue dots), for the prototype target wheel immersed at a depth of 50.25 mm in a magnetic field with peak value 0.485 T.

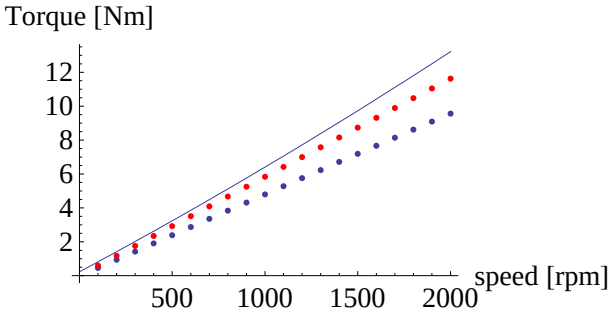

Figure 5.15: As Fig. 5.14, but with the rim thickness increased by 50% to 45 mm in the analytical and Opera simulation models, to account for the effect of the spokes.

results are shown in Fig. 5.15. The results from the analytical model and the Opera simulation are now in much better agreement with the experimental results.

5.4.4 Temperature Measurements

Since the eddy currents induced by the rotation of the wheel in a strong magnetic field lead to energy dissipation in the wheel by ohmic losses, measurements of the temperature of the wheel under various conditions potentially offer a way to characterise the eddy currents. Because of the high speed of rotation of the wheel, the most practical way to measure the temperature rise during rotation is by means of a thermal camera. However, since the characteristics of the thermal radiation from an object depend on the surface properties of the material, it is necessary to calibrate the camera for the particular application. Fig. 5.16 shows the equipment used for the calibration. The fan-shaped metal block is a sample from the same material used for the construction

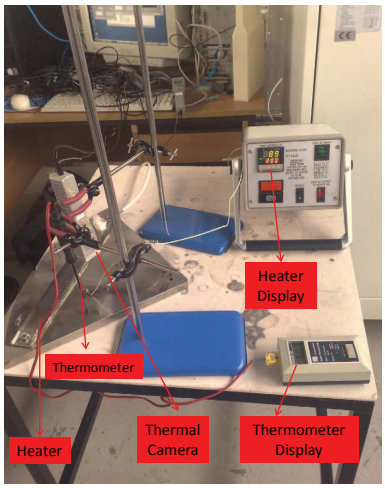

Figure 5.16: Equipment for titanium alloy material thermal test and thermal camera calibration.

of the prototype target wheel. There is a heater attached to the upper surface of the block. On the right-hand far corner of the table is the heater controller, which can be used to monitor the temperature of the heater. Two devices will be used to monitor the temperature of the metal block, at a position about 5 mm away from heater. The first device is the thermal camera, and the second is a thermometer.

The results from the calibration are shown in Fig. 5.17. We see that the heater raises the temperature of the metal block from 15℃ to 185℃, as read from the heater controller. The blue dots show the readings from the thermometer (placed about 5 mm away from the heater); the blue line shows a linear fit of the data. The thermometer measures a temperature rise from 15℃ to 166.4℃. The fit line has a gradient of 0.892. Considering the distance from the heater to the thermometer, and the thermal conductivity of the titanium alloy, the thermometer appears to be reasonably accurate. The purple dots in Fig. 5.17 show the temperature measured by the thermal camera, with the solid purple line showing a linear fit. There is a significant difference between the temperature reading from the thermal camera, and the temperature indicated by the thermometer. The thermal camera shows a temperature increase from 15℃ to 120℃; the linear fit has a gradient of 0.615.

The most likely reason for the discrepancy between the temperature readings from the thermometer and the camera is that the camera has not been set correctly for the thermal emissivity of the titanium alloy. In general, many inexpensive cameras will be

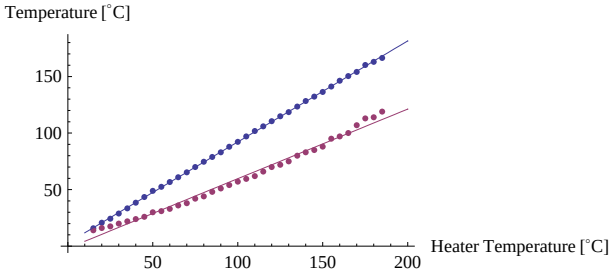

Figure 5.17: Results from thermal camera calibration measurements. We increase the heater temperature from 0 to 200 as shown x-axis. The blue dots are the temperature reading from thermometer and red dots are the reading from thermal camera.

set for an emissivity of around 0.95; however, our test material is a piece of polished titanium alloy, for which the emissivity could be in the range 0.08 to 0.19. Although there will inevitably be some uncertainty in the results of the temperature readings from the camera, we can use the results shown in Fig. 5.16 to determine a more accurate value for the temperature of the target wheel, from the temperature value returned from the thermal camera.

Fig. 5.18 shows a sample image from the megapixel thermal imaging camera. The heater temperature was 185℃. A short distance from the heater, the temperature of the block is around 100℃: there is a large temperature gradient because of the relatively poor thermal conductivity of the material. Most of the block remains in the temperature range 18℃ to 30℃. If there is a large power dissipation from the eddy currents in the ILC positron production target, then it could be difficult to provide sufficient cooling, because of the poor thermal conductivity.

Two thermal imaging cameras were installed within the safety cage of the target wheel experiment, and directed towards the rim of the prototype target wheel. Fig. 5.19 shows the temperature measured as a function of rotation speed, when the wheel is immersed at a depth of 30.25 mm within a magnetic field with peak 1.44 T. We see that the direct reading from the thermal imaging camera shows a temperature increase from 23℃ to 54℃ as the speed of rotation increases from 200 rpm to 1200 rpm. Using the calibration data, we infer that the real temperature increase was from 40℃ to 91℃.

Assuming that the temperature of the rim is determined by an equilibrium between heating from eddy currents and radiative cooling, we can make a check on the consistency between the temperature measurements and the torque measurements. From

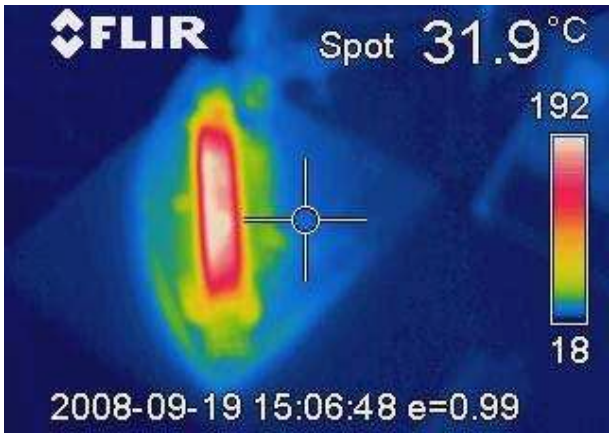

Figure 5.18: Sample image from megapixel thermal imaging camera.

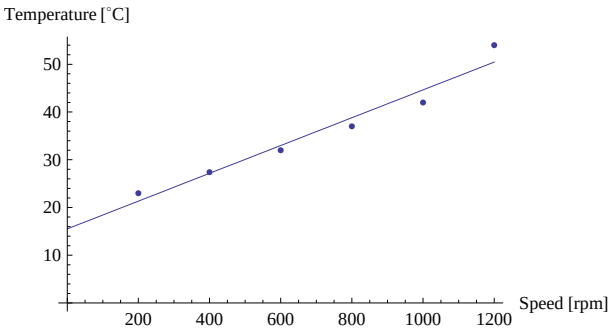

Figure 5.19: Temperature of wheel rim as a function of rotation speed for the wheel immersed at a depth of 30.25 mm in a magnetic field with peak strength 1.44 T. The temperature shown is taken directly from the camera (calibration factor not applied).

Stefan's law, the thermal power radiated by an object of surface area A, emissivity ε, and (absolute) temperature T is:

$$P = A\varepsilon\sigma T^4, \tag{5.15}$$

where σ is Stefan's constant:

$$\sigma \approx 5.67 \times 10^{-8}\,\mathrm{Js^{-1}m^{-2}K^{-4}}. \tag{5.16}$$

The surface area of the rim of the wheel, neglecting the spokes, is $A \approx 0.278\,\mathrm{m}^2$. The main uncertainty in applying Stefan's law is in the emissivity. Therefore, we calculate the power generated by eddy currents from the torque data:

$$P = \omega\tau, \tag{5.17}$$

and calculate the emissivity of the surface of the wheel from the measured temperature under the same conditions (rotation speed, field strength and immersion), assuming that the thermal radiation power Eq. 5.15 is equal to the mechanical power Eq. 5.17. Note that we neglect thermal energy absorbed by the wheel from its surroundings.

With a peak field of 1.44 T and immersion 30.25 mm, the torque at a revolution speed of 200 rpm is approximately 4 Nm (see Fig. 5.13). This gives a mechanical power of about 84 W. The measured temperature (after applying the calibration factor) of the rim under these conditions is about 40℃. Therefore, using Stefan's law, an emissivity of about 0.55 would be needed, to provide a radiation power of 84 W. This is a credible figure, if somewhat larger than expected.

When the revolution speed is increased to 1200 rpm, under the same magnetic field conditions, the torque increases to about 22 Nm. This implies a mechanical power of more than 2.7 kW. The measured temperature of the rim under these conditions is about 91℃. Again applying Stefan's law, we find an emissivity of about 10 would be required to provide the thermal radiation power: this is clearly unphysical. There are a number of possibilities to explain the results. The first is that the measured torque is too large. However, the Opera model and analytical estimate suggest that neglecting the spokes in the wheel, the torque would only be about a factor of four lower. If the torque were equal to the value predicted by the models rather than the experimentally measured value, the emissivity would still need to be about 2.5, which is still unphysical.

The second possibility is that the real temperature is higher than the measured temperature, even after applying the calibration factor. But with an emissivity of 0.55, the temperature of the rim would need to be more than 470℃ to give a thermal radiation power of 2.7 kW. It seems unlikely that the temperature reading could be so much in error.

Finally, there is the possibility that effects we have neglected play a significant role in determing the equilibrium temperature. For example, the rim will cool by conduction through the spokes, as well as by radiation, and also by convection through the air around the wheel. Given the relatively poor thermal conductivity of the spokes, it seems unlikely that conduction could account entirely for the discrepancy between the thermal radiation power and the mechanical power calculated from the torque and the revolution speed. However, at high revolution speeds, convection could provide significant cooling for the target wheel.

The most likely explanation is that all three possibilities play some role. Thus, effects other than eddy currents (such as friction) make some contribution to the torque - so the mechanical power calculated from the torque overestimates the power generated by eddy currents. Also, the thermal imaging cameras are not giving a completely reliable value for the temperature of the target wheel. And in addition, thermal effects such as conduction and (more probably) convection make a significant contribution to the cooling of the target wheel, leading to a lower equilibrium temperature than would be expected from radiation effects alone. To take all these effects properly into account would require a considerable amount of further work, which is beyond the scope of the present project.

5.5 Conclusion

In this chapter, we have discussed experimental studies aimed at understanding mechanical issues for the ILC positron source production target. In particular, there are concerns regarding the effects of eddy currents generated if the target spins at high speed in the strong magnetic field of a matching device. The eddy currents can lead to large forces opposing the rotation of the target, and can generate significant thermal loads by ohmic losses in the material of the target.

To address these concerns, a full-scale target prototype has been constructed. Me-

chanical and thermal tests have been carried out, based on measurements of torque and temperature rise when the target spins at different speeds in a magnetic field of adjustable strength. The results of the measurements can be compared with results from simplified analytical and simulation (Opera) models.

The analytical model for the torque resulting from the eddy currents gives some understanding of the important factors. In particular, there is a strong dependence on the width of the rim of the target wheel, and on the gradient of the magnetic field as a function of position around the rim. The torque scales linearly with the conductivity of the material, and with the revolution speed. The torque predicted from the analytical model is in reasonable agreement with the torque predicted by a computational model, using Opera. However, the measured torque is three or four times larger than the theoretical predictions. A likely explanation for this is that eddy currents in the spokes, which are neglected in the analytical and simulation models, make a significant contribution to the overall torque. Unfortunately, our present simulation tools are not capable of handling the more complex geometry that would include the spokes. However, we have shown that a moderate increase in rim width can have a significant impact on the torque from the eddy currents.

There is still considerable uncertainty in the results of the thermal measurements. In particular, there is rather poor agreement, particularly at high rotation speeds, between the mechanical power dissipation and the thermal power dissipation. However, the thermal power dissipation was calculated assuming that all the power was dissipated by radiation, and it is likely that conduction and (to a greater extent) convection also play a significant role.

Despite continuing uncertainties (which seem not likely to be easily addressed) the target wheel experiment has led to a better understanding of the mechanical and thermal issues associated with rotating the ILC positron production target in the strong magnetic field of a matching device. This understanding should help with future design optimisation, and with evaluating configuration options that could affect the operating parameters.

6

Summary and Conclusions

6.1 Summary

The demands on positron sources have increased with successive generations of accelerators. Storage ring colliders need relatively low power sources, because the particles can be accumulated over time in the storage ring. Even for SLC, the only linear collider to be built so far, a conventional positron source was sufficient. However, future linear colliders aiming at high energy and luminosity will need quantities of positrons more than an order of magnitude greater than in SLC. Furthermore, the range of physics studies can be greatly increased if polarised positrons are available.

ILC and CLIC are the main linear collider projects presently under study. The challenges for the positron sources for these machines are such that different types of source can be considered, including: a conventional source; an undulator-based source (currently the baseline for ILC); and a Compton source (currently the baseline for CLIC).

Conventional positron sources are based on impacting a high-energy (multi GeV) electron beam on a target. Gamma-ray photons are generated by bremsstrahlung in the target, and electron-positron pairs are then created from the gamma rays, again by interaction with the target material. The target needs to be thick, because of the need for both bremsstrahlung and pair creation to take place in the same target. Energy deposition tends to be high; although this is not too much of a problem for low power sources required by storage ring colliders, it is an issue for future linear colliders. One solution would be to use multiple conventional sources, combining the beams in a

damping ring. It is not possible to produce polarised positron beams from conventional sources.

The availability of electron beams with tens or hundreds of GeV energy makes it possible to consider an undulator-based source for a future linear collider. Undulators are well-established as insertion devices operating in light sources, with electron beam energies of a few GeV. In that regime, they generally produce photons up to X-ray energies, which would be too low for pair creation. However, with electron beam energies of 100 GeV or more, it is possible to produce gamma rays from undulators with reasonable parameters. The gamma rays impact a target, and produce positrons by pair creation. Because the beam incident on the target is already a photon beam, the target can be thinner than in a conventional source; and the energy deposition can be lower for a given rate of positron production. Furthermore, by using a helical undulator to produce polarised photons, polarised positrons can be produced. The disadvantage for a linear collider, is that the production of positrons depends on the high energy electron beam that is used for collision. The design and operation will be complicated, and constrained by the fact that the production of the positron beam is coupled to the electron beam. The production of polarised positrons from a helical undulator has already been demonstrated in the E166 experiment at SLAC [24].

In a Compton source, gamma rays are produced by Compton scattering photons in a laser from electrons in a storage ring. This approach has the advantage of being able to produce polarised positrons, without coupling the positron production to the colliding electron beam. However, this is still a new concept that requires substantial R&D.

The undulator-based source for ILC is a relatively mature design. In particular, the undulator has been studied intensively, and a prototype has been constructed and tested. We have modelled the entire system from the undulator to the end of the first positron acceleration (RF) section, using computer simulations and analytical methods. In particular, we have looked closely at the positron yield and polarisation. Our results confirm the expected results. We have extended previous studies by looking closely at options for a photon collimator, considering the possibility to improve the polarisation of the positron beam (albeit at the expense of some reduction in the positron yield). We have compared two possible designs for the photon collimator, looking at collimation efficiency, energy deposition and activation.

Although the present baseline for CLIC is a Compton source, an undulator-based positron source is an option. In principle, the ILC design could be adapted relatively easily for CLIC. The required rate of positron production is lower for CLIC than for ILC. However, there is a potential issue with the energy deposition in the target. In ILC, the pulse length is relatively long, about 1 ms. This means that by rotating the target at high velocity (about 100 m/s at the rim) the energy in the pulse can be spread over a relatively large volume (compared to a stationary target). The density of energy deposition can then be kept within engineering limits. For CLIC, although the average rate of positron production needed is lower than in ILC, each machine pulse is much shorter, about 177 ns. Even with a target moving at 100 m/s, the density of energy deposited would be about the same as in a stationary target. A further issue for the design of an undulator-based source for CLIC is the upgrade path. Initially, in Stage 1, CLIC will operate with 500 GeV centre of mass collision energy. The energy at the end of the linac will be 250 GeV for both beams. However, the intention is to upgrade the machine in Stage 2, to operate with 3 TeV centre of mass collision energy. This will likely be achieved by extending the linacs. The beam energy at the location of the undulator in an undulator-based positron source would then increase by 1.25 TeV. It is not feasible to develop a design for the positron source that would operate over such a wide range of energy. The options are either: to move the positron source to a new location; or, to replace the undulator. In principle, the first option, to move the positron source to a new location, requires little further study. However, since all the components would need to be moved, and long transport lines would be needed to take the positron beam to the damping ring, this may be an expensive option. We have therefore considered a possible scenario for the second option.

Finally, one of the main issues for the ILC undulator-based positron source is the eddy currents generated by rotating the target in the strong magnetic field of the matching device. The matching device is required to minimise beam losses between the target and the first acceleration section; however, greatest transfer efficiency is achieved if there is no gap between the target and the matching device. The high speed of the target wheel rotation in the field of the matching device then leads to strong eddy currents. To understand the heating and mechanical effects of these eddy currents, experimental studies of a prototype target wheel have been carried out at Daresbury laboratory. We have analysed the data and presented the results of these studies, and

made comparisons with the theoretical and simulation models.

6.2 Conclusions

For ILC, we find good agreement between the analytical and various simulation tools used to study the system, from the photon spectrum and polarisation from the undulator, to the positron yield and polarisation at the end of the first acceleration section. Our studies are based on the present ILC baseline parameters, with an undulator of length 147 m, deflection parameter 0.92, period 11.5 mm, using an electron beam energy of 150 GeV. The system should produce a sufficient number of positrons.

We compared two different designs for a photon collimator for ILC. By comparing the collimation efficiency, energy deposition, activation, and production of secondary particles, we find that one of the designs ("Model 2") has some advantages. As well as a lower energy deposition and activation, there are fewer secondary particles that exit the Model 2 collimator, compared to Model 1.

The target is one of the most important and difficult components in the system. For ILC, to spread the energy deposition from the photon beam, the target needs to rotate at high speed (2000 rpm, giving a rim velocity of 100 m/s). As well as the energy deposition, issues such as the positron yield and polarisation, and the effects of eddy currents need to be taken into account in the design. Optimisation of the target (material, geometry, rotation speed) is a complex multi-dimensional problem. However, our studies show that the present baseline design, using titanium alloy with a thickness of 0.4 radiation lengths, seems suitable, and there appear to be few benefits in changing any of the design options or parameters.

Between the target and the first acceleration section, a matching device is needed to match the phase space distribution of the positrons from the target to the solenoid focusing in the RF. The matching device produces a strong longitudinal magnetic field. The positron capture is most efficient if the field extends up to (and into) the target, without any gap. However, when the target rotates at high speed, eddy currents are then generated that have undesirable effects, including heating, and braking forces. Nevertheless, we can consider optimisation of the parameters of the matching device. In particular, for an adiabatic matching device, we can study the capture efficiency and polarisation of the positron beam, as functions of the peak field, taper parameter and

length of the matching device. Theoretically, all these parameters can be optimised for given distributions at the entrance and exit of the matching device. However, the optimum parameters depend on the beam energy: this is not well defined for the positron from the target, because the energy spread is extremely large. Therefore, optimisation is best done by simulation. We find that a high initial field (around 6 T) is needed to achieve a good capture efficiency. However, there is a relatively weak dependence on the taper parameter, and the nominal value of $30\,\mathrm{m}^{-1}$ seems appropriate.

With a peak field of 6 T on the target, the eddy currents generated by the rotation of the target will have strong effects. To reduce the effects, we can consider introducing a gap between the target and the matching device. However, the capture efficiency falls rapidly as the gap is increased. For example, a gap of 1 cm between the target and the matching device leads to a loss of 35% of the positrons from the target.

Although a Compton source is the current baseline for CLIC, it is still interesting to consider an undulator-based source as an alternative. Because of the similarities between CLIC and ILC, it is possible to adopt the ILC design with few changes. For the first stage of operation of CLIC, with 500 GeV centre of mass collision energy, the undulator for the positron source could be placed at the end of the linac (250 GeV electron beam energy), or part of the way along the linac, for example with an electron beam energy of 150 GeV as in ILC. In either case, an undulator based source with parameters similar to those for ILC should work well. In fact, CLIC can benefit from the possibility of having a pre-damping ring for the positrons. A pre-damping ring is feasible for CLIC because the pulse length is relatively short, which means the damping rings (which must store an entire beam pulse) can be small. For ILC, the damping rings must be several kilometres in circumference; in that case, it becomes strongly undesirable to build a pre-damping ring in addition to the main damping ring, because of the cost. However, for CLIC, the larger acceptance that is possible in a pre-damping ring has a big impact on the overall yield of the positron source. As a result, the undulator length can be significantly reduced in CLIC (to about 30 m) compared to ILC, and this helps to reduce the peak energy deposition in the target.

One drawback of the short pulse length in CLIC is that the peak energy deposition in the target cannot be significantly reduced by rotating the target. The speed with which the target would need to be rotated, so that it travels an appreciable distance during the CLIC pulse duration of 177 ns, is not realistic. Some rotation of the target is still

desirable, so that the energy from different pulses is deposited in different locations on the target. However, since the pulse repetition rate is relatively slow in CLIC (120 Hz), this rotation can be relatively slow. This reduces the impact of eddy currents from the matching device; but the energy deposition from a single pulse becomes more of a concern.

In the second stage of CLIC, for operation at 3 TeV centre of mass energy, the electron beam energy at the original location of the positron source undulator will increase significantly, by about 1.25 TeV. Without changing either the location or the design of the undulator, the photon power would increase dramatically, meaning that the target would be quickly destroyed. One option would be to relocate the undulator so that the electron beam energy is the same as before. However, this would also mean relocating the photon collimator, the target station and matching device, and the linac used to accelerate the positrons to the damping ring energy. A very long transport line would also have to be installed, to carry the positrons from the source to the damping ring. These modifications would add to the cost and complexity of the upgrade. An alternative would be to leave the positron source in the same location, and just replace the undulator. We have studied the second option: our results show that by using an undulator with a longer period and slightly larger deflection parameter, operating an undulator-based positron source with an electron beam energy of 1.5 TeV appears feasible. Again, significant advantage can be taken from the large acceptance of the pre-damping ring to keep the undulator length reasonable.

One drawback with an undulator-based positron source with 1.5 TeV electron beam energy is that the positron polarisation is lost. This is because the capture efficiency of the positrons is very high. Photons far from the axis of a helical undulator have a different polarisation compared to photons that are close to the axis. In the ILC, the photons that are far from the axis can be collimated, or produce positrons that have lower energy and are outside the acceptance of the system. Therefore, photons close to the axis are more likely to produce captured positrons than photons far from the axis. As a result, the polarisation of the positron beam in ILC can be relatively high. However, with an electron beam energy of 1.5 TeV, the divergence of the photon beam from the undulator is extremely small, making collimation very difficult or impossible. Furthermore, all photons are likely to produce positrons that are within the acceptance of the system. Therefore, photons with a full range of polarisation contribute to the

positron beam, and the positron polarisation is extremely small.

A further drawback with an undulator-based source operating with 1.5 TeV electron beam energy is that the photon beam power on the target is high. Since pulse duration in CLIC is very short, it is not possible to spread the energy deposition by rotating the target. It is not clear if a good solution for the target in this case can be found: this should be the major focus of attention, if the option of replacing the undulator in a fixed location during the CLIC Stage 2 upgrade is studied further.

Finally, we reported the results from the target wheel experiments at Daresbury Laboratory. This experiment was designed to investigate the effects of the large eddy currents that would be induced in the ILC positron target, when the target is rotated at high velocity in the strong magnetic field of a matching device. The results have been compared with simulation and analytical models. Although it is possible to understand the major effects from relatively simple analytical models, the detailed behaviour depends strongly on the shape of the magnetic field, and on the geometry of the wheel itself. Experimental studies therefore included measurements of the magnetic field profile, and measurements of the torque acting on the wheel and the temperature of the wheel, with a range of rotational velocities, magnetic field strengths, and immersion depths of the wheel in the magnetic field.

Measurements of the magnetic field were found to be in good agreement with the predictions of magnetic modelling codes. We also found good agreement between the various (simulation and analytical) models for the torque on the wheel under various conditions. However, the torque acting on the wheel was found to be up to a factor of three larger than that predicted by the models. This may be due to effects not properly included in the models, such as the spokes in the wheel. Further, more detailed modelling work would be needed to confirm this. Although some temperature measurements have been made, the results are not accurate or reliable enough at this stage to draw any firm conclusions.

Despite continuing concerns with the positron target, which will need further work, our studies show that the design of the undulator-based positron source for ILC is mature, and should achieve the performance necessary. An undulator-based positron source is also an interesting option for CLIC. In Stage 1, a design very similar to ILC could be used. There is also the possibility of keeping the source in a fixed location, and just replacing the undulator in the upgrade to Stage 2, if the peak energy deposition

in the positron target can be handled.

Bibliography

[1] V.N. Baier. Forty Years of Acting Electron Positron Colliders. *hep-ph/0611201*, 2006.
http://arxiv.org/PS-cache/hep-ph/pdf/0611/0611201v1.pdf. 2

[2] L. Paoluzi. e^+e^- Colliding Beams Physics. *Acta Phys. Pol. B5 (1974) 839.*, 1974. 2

[3] C. Biscari. Accelerators R&D. *Proceedings of Science*, 2009.
http://pos.sissa.it/archive/conferences/084/019/EPS-HEP%202009-019.pdf. 2

[4] B. Carlo. AdA: The First Electron-Positron Collider. *Physics in Perspective*, 6(2):156–183, Jun 2004.
http://dx.doi.org/10.1007/s00016-003-0202-y. 2

[5] M. Ye and Z. Zheng. BEPC, The Beijing Electron-Positron Collider. *Nuclear Physics B-Proceedings Supplements*, pages 156–183, 1988.
http://www.sciencedirect.com/science/article/B6TVD-481MXMF-1F/2/d324db35a3c3584d9981c1bea6e3ebd8. 2

[6] X. Yu, Y. Chen, X. Wang, and M. Liu. Operation Status of The Beijing Electron-Positron Collider. *Proceedings of APAC 2004*, 2004.
http://accelconf.web.cern.ch/accelconf/a04/PAPERS/MOP10003.PDF. 5

[7] Guo, X. et. al. Positron Source. *Nuclear Physics*, pages 66–70, 2006. 6

[8] S.N. Ganguli. The story of large electron positron collider. *Resonance*, 7(10):30–44, October 2002.
http://dx.doi.org/10.1007/BF02835541. 6

[9] E. Keil. LEP Parameter List. *CERN/ISR-LTD/76-51*, 1976. http://cdsweb.cern.ch/record/323326/files/197703227.pdf. 7

[10] http://www2.slac.stanford.edu/vvc/experiments/slc.html. 7

[11] S. Ecklund. The SLC Positron Source Design and Performance. http://www.slac.stanford.edu/cgi-wrap/getdoc/nkpslc97-004.pdf. 8

[12] A.V. Kulikov, S.D. Ecklund, and E.M. Reuter. SLC Positron Source Pulsed Flux Concentrator. *SLAC-PUB-5473*, 1991. http://www.slac.stanford.edu/cgi-wrap/getdoc/slac-pub-5473.pdf. 8

[13] K. Desch. Electron-Positron Linear Collider. *Particle Physics and the Universe*, 2005. http://dx.doi.org/10.1007/3-540-26798-0-33. 9

[14] F. Amman. Electron Positron Storage Rings: Status and Present Limitations. *Nuclear Science, IEEE Transactions on*, 1969. http://ieeexplore.ieee.org/xpls/abs-all.jsp?arnumber=4325443. 9

[15] K. Floettmann. Positron Source Options for Linear Colliders. *Proceedings of EPAC 2004, Lucerne, Switzerland*, 2004. http://accelconf.web.cern.ch/AccelConf/e04/PAPERS/TUZACH01.PDF. 10

[16] T. Ince and R.K. Keeler. Positron Resolution of ATLAS Electromagnetic Endcap Calorimeter. *CERN-THESIS-2006-051*, 2005. http://cdsweb.cern.ch/record/989091?ln=hr. 11

[17] J.A. Clarke. *The Science and Technology of Undulators and Wigglers*. Oxford University Press, 2004. http://dx.doi.org/10.1093/acprof:oso/9780198508557.001.0001. 12, 30, 32

[18] K. Masao. Laser compton update. *ILC Positron Source Meeting*, 2007. 13, 26

[19] R. Chehab et al. An Hybrid Positron Source For CLIC. *CERN CLIC Workshop*, 2008. 14, 25, 110

[20] N. Phinney et al. International Linear Collider Reference Design Report. *ILC Publications*, 2007.

http://www.linearcollider.org/about/Publications/Reference-Design-Report. 15, 16, 65, 68

[21] H. Braun, R. Corsini, J. Delahaye, A. Roeck, S. Doebert, G. Geschonke, A. Grudiev, C. Hauviller, S. Weisz, and W. Wunsch. CLIC 2008 Parameters. *CERN-OPEN-2008-021 and CLIC-Note-764*, 2008. http://cdsweb.cern.ch/record/1132079/files/CERN-OPEN-2008-021.pdf. 15, 109

[22] W. Gai and W. Liu. Positron Source for Linear Colliders. *AIP Conference Proceedings*, 1160(1):67–73, 2009. http://link.aip.org/link/?APC/1160/67/1. 19

[23] D.J Scott. An Investigation into the Design of the Helical Undulator for the International Linear Collider Positron Source. 2008. http://epubs.cclrc.ac.uk/bitstream/2980/Duncan-Scott-Thesis.pdf. 19

[24] G. Alexander, J. Barley, Y. Batygin, S. Berridge, V. Bharadwaj, G. Bower, W. Bugg, F.-J. Decker, R. Dollan, Y. Efremenko, V. Gharibyan, C. Hast, R. Iverson, H. Kolanoski, J. Kovermann, K. Laihem, T. Lohse, K. T. McDonald, A. A. Mikhailichenko, G. A. Moortgat-Pick, P. Pahl, R. Pitthan, R. Pöschl, E. Reinherz-Aronis, S. Riemann, A. Schälicke, K. P. Schüler, T. Schweizer, D. Scott, J. C. Sheppard, A. Stahl, Z. M. Szalata, D. Walz, and A. W. Weidemann. Observation of polarized positrons from an undulator-based source. *Phys. Rev. Lett.*, 100(21):210801, May 2008. 20, 110, 160

[25] L. Zang, A. Wolski, and I. Bailey. Studies on the Role of a Photon Collimator for the ILC Positron Source. *Proceedings of EPAC 2008*, 2008. http://accelconf.web.cern.ch/accelconf/e08/papers/mopp079.pdf. 20

[26] R. Tomás. Overview of the compact linear collider. *Phys. Rev. ST Accel. Beams*, 13(1):014801, Jan 2010. http://prst-ab.aps.org/pdf/PRSTAB/v13/i1/e014801. 23

[27] L. Rinolfi. CLIC Main Beam Injectior Complex Review. *CLIC09 Workshop*, 2009. 25, 109

[28] F.R. Elder, A.M. Gurewitsch, R.V. Langmuir, and H.C. Pollock. Radiation from Electrons in a Synchrotron. *Phys. Rev.*, 71(11):829–830, Jun 1947. http://prola.aps.org/pdf/PR/v71/i11/p829-5. 30

[29] A. Hofmann. Synchrotron Radiation From the Large Electron-positron Storage Ring LEP. *Physics Reports*, 64(5):253 – 281, 1980. http://www.sciencedirect.com/science/article/B6TVP-46TY56G-B/2/d422a3cc58fa1c9c3f2d2fa6aef447d1. 30

[30] G. Stephenson. Special Relativity for Physicists. *New York, Longmans, Green*, 1958. 31

[31] C. Xiao. Liendar-Wiechert Potential and Consequent Fields. *Phys 463, E and M III.* http://physics.usask.ca/xiaoc/phys463/notes/note19.pdf. 32

[32] J.H. Poynting. On the Transfer of Energy in the Electromagnetic Field. *Phil. Trans. 175: 277*, 1884. http://puhep1.princeton.edu/ mcdonald/examples/EM/poynting-ptrsl-175-343-84.pdf. 33

[33] B. George, H. Arfken, and J. Weber. Mathematical Methods for Physicists. *Harcourt: San Diego*, 2001. 34

[34] B.M. Kincaid. A Short-period Helical Wiggler as An Improved Source of Synchrotron Radiation. *Journal of Applied Physics*, 48(7), 1977. http://ieeexplore.ieee.org/xpls/abs-all.jsp?arnumber=5103840. 34, 35

[35] G. Battistoni, S. Muraro, P.R. Sala, F. Cerutti, A. Ferrari, S. Roesler, A. Fasso, and J. Ranft. The FLUKA code: Description and Benchmarking. *AIP Conference Proceeding 896, 31-49*, 2007. http://adsabs.harvard.edu/abs/2007AIPC..896...31B. 42

[36] A. Fasso, A. Ferrari, J. Ranft, and P.R. Sala. FLUKA: a multi-particle transport code. *CERN-2005-10 (2005), INFN/TC, SLAC-R-773*, 2005. http://www.osti.gov/energycitations/product.biblio.jsp?osti-id=877507. 42

[37] C.W. Fabjan and T. Ludlam. Calorimetry in High-Energy Physics. *Ann. Rev. Nucl. Part. Sci*, 32, 1984.
http://arjournals.annualreviews.org/doi/abs/10.1146/annurev.ns.32.120182.002003. 45, 46

[38] I.R. Bailey et al. Development of A Positron Production Target for the ILC Positron Source. *Proceedings of EPAC 2006*, 2006.
http://www.slac.stanford.edu/cgi-wrap/getdoc/slac-pub-12659.pdf. 49

[39] A. Wolski. Dynamical Maps for Linear Elements. *Linear Dynamics, Lecture 4*, 2006.
http://pcwww.liv.ac.uk/ awolski/. 50

[40] R. Chehab. Positron Sources. *Proceedings of Cern Accelerator School*, page 664, 1992.
http://cas.web.cern.ch/cas/CAS-Proceedings.html. 53

[41] R. Chehab. Positron Sources. *Proceedings of Cern Accelerator School*, page 668, 1992.
http://cas.web.cern.ch/cas/CAS-Proceedings.html. 54

[42] R.H. Helm. Adiabatic Approximation for Dynamics of a Particle in the Filed of a Tapered Solenoid. *Technical Report, SLAC Report No.4*, 1962.
http://www.slac.stanford.edu/pubs/slacreports/reports03/slac-r-004.pdf. 54

[43] W. Gai. Positron Source for Linear Colliders. *JPOS 2009, Jefferson Lab*, 2009.
http://conferences.jlab.org/JPOS09/talks/Gai.ppt. 65

[44] J.A. Clarke et al. An Investigation into the Design Parameters and the Subsequent Manufacture and Testing of a 4m Superconducting Helical Undulator Module for the International Linear Collider Positron Source. *PACS No 07.85. Qe, 85.70.ay*, 2008. 66

[45] I.R. Bailey et al. Eddy Current Studies From the Undulator-based Positron Source Target Wheel Prototype. *Proceedings of IPAC'10, Kyoto*, 2010.
http://accelconf.web.cern.ch/accelconf/IPAC10/papers/thpec033.pdf. 66

[46] V. Bharadwaj, Y. Batygin, R. Pitthan, and J. Sheppard. Design Issues for the ILC Positron Source. *Proceedings of 2005 Particle Accelerator Conference, Knoxville*, 2005.
http://ieeexplore.ieee.org/xpls/abs-all.jsp?arnumber=1591422&tag=1. 66

[47] J.C. Sheppard. Helical Undulator Radiation. *Stanford Linear Accelerator, Menlo Park, California 94025*, 2002.
http://www.hep.princeton.edu/ mcdonald/e166/LCC%20notes/LCC-0095.pdf. 67

[48] A. Bungau et al. Design of the Photon Collimators for the ILC Positron Helical Undulator. *Proceedings of EPAC'08*, 2002.
http://accelconf.web.cern.ch/accelconf/e08/papers/mopp008.pdf. 68

[49] N. Golubeva and V. Balandin. private correspondence. 2006. 69

[50] A. Mikhailichenko. Collimator for ILC. *Proceedings of EPAC'06*, 2006.
http://accelconf.web.cern.ch/AccelConf/e06/PAPERS/MOPLS105.PDF. 69

[51] L. Zang, I. Bailey, and A. Wolski. Studies on the Role of a Photon Collimator for the ILC Positron Source. *Proceedings of EPAC'08*, 2008.
http://accelconf.web.cern.ch/accelconf/e08/papers/mopp079.pdf. 71

[52] A. Fassa, A. Ferrari, J. Ranft, and P.R. Sala. FLUKA User Manual: Gamma Incident.
http://www.fluka.org, 2008. 71

[53] A. Fassa, A. Ferrari, J. Ranft, and P.R. Sala. FLUKA User Manual: Polarised Electron/Positron/Gamma Incident.
http://www.fluka.org, 2008. 71

[54] A. Ushakov, E. Elsen, K. Flottmann, S. Riemann, and K. Sanosyan. Radiation Levels and Activation at the ILC Positron Source. *EUROTeV-Report-2006-052*, 2006.
http://accelconf.web.cern.ch/AccelConf/e06/PAPERS/WEPLS046.PDF. 87

[55] Induced Radioactivity. *7th FLUKA Course, NEA, Paris*, 2008. 87

[56] H. Stelzer and C. Weibbacher. Investigation of the Temperature Rise Duo to Eddy Currents in Large Chopper Disks Operated at Polarised Neutron Beamlines.

Nuclear Instruments and Methods in Physics Research, 2008. http://www.sciencedirect.com/science/article/B6TJM-4SWN0JK-4/2/68e63313a5eb008a102b229eb4c9eafa. 96

[57] Y.K. Batygin. Positron Collection in the ILC. *Workshop on Positron Source for the International Linear Collider*, 2005. 97

[58] A. Wolski. SAMM: Simple Accelerator Modelling in Matlab. *Version 1.0*, 2009. http://pcwww.liv.ac.uk/ awolski/mai-links-computercodes.htm. 100

[59] H. Wang and W. Liu. Design and Prototyping of the AMD for the ILC. *Proceedings of PAC07*, 2007. http://accelconf.web.cern.ch/accelconf/p07/PAPERS/THPMN092.PDF. 105

[60] P. Logachev et al. Ultimate Abilities of Cnventional Positron Source. *Proceedings of APAC07*, 2007. http://accelconf.web.cern.ch/accelconf/a07/PAPERS/TUC3MA03.PDF. 109

[61] L. Rinolfi et al. CLIC Positron Source for the Baseline Configuration. *POSIPOL 2010 Workshop*, 2010. http://kds.kek.jp/conferenceOtherViews.py?view=standard&confId=4686. 110

[62] L. Rinolfi et al. The CLIC positron source based on Compton schemes. *presented at PAC09, CLIC Note 788*, 2009. http://cdsweb.cern.ch/record/1212994/files/CERN-ATS-2009-086.pdf. 110

[63] I. Bailey and L. Zang. CLIC Undulator Option for Polarised Positrons. *CLIC 08 Workshop*, 2008. http://indico.cern.ch/contributionDisplay.py?sessionId-3&contribId-82&confId=30383. 110

[64] W. Liu, W. Gai, L. Rinolfi, and J. Sheppard. An Undulator Based Polarized Positron Source for CLIC. *Presented at IPAC10*, 2010. http://accelconf.web.cern.ch/AccelConf/IPAC10/papers/thpec035.pdf. 110

[65] R. Chehab et al. Positron Source for e^+e^- Colliders: Application to ILC and CLIC. *IPNL/IN2P3/CNRS, University Lyon 1*, 2008. 110

[66] L. Zang, A. Wolski, and I. Bailey. Undulator Based Positron Source Optimisation for CLIC. *Proceedings of IPAC10*, 2010. http://accelconf.web.cern.ch/accelconf/IPAC10/papers/thpec034.pdf. 110

[67] L. Zang. Undulator Based Positron Source for CLIC. *LCABD Collaboration Meeting*, 2009. 111

[68] P.J Duke. Synchrotron Radiation. *Oxford Series on Synchrotron Radiation*, 2000. 113

[69] D. Scott et al. Design Considerations for a Helical Undulator for The Production of Polarised Positrons for TESLA. *Proceedings of EPAC 2004*, 2004. http://accelconf.web.cern.ch/AccelConf/e04/PAPERS/MOPKF064.PDF. 116

[70] Y. Ivanyushenkov et al. Development of a Superconducting Helical Undulator for a Polarised Positron Source. *Proceedings of 2005 Particle Accelerator Conference*, 2005. http://accelconf.web.cern.ch/AccelConf/p05/PAPERS/MPPT033.PDF. 116

[71] Y. Ivanyushenkov et al. Status of R&D on a Superconducting Helical Undulator for The ILC Positron Source. *Proceedings of PAC07*, 2007. http://accelconf.web.cern.ch/AccelConf/p07/PAPERS/THPMN071.PDF. 116

[72] M. Korostelev. private correspondence. 2006. 118

[73] J. L. Fernandez-Hernando et al. Material Damage Test for ILC Collimators. *Proceedings of PAC07*, 2007. http://accelconf.web.cern.ch/AccelConf/p07/PAPERS/THPMN072.PDF. 125

[74] R. Chehab. Angular Collection Using Solenoids. *Submitted to Elsevier*, 2000. http://muonstoragerings.web.cern.ch/muonsto%ragerings/Workshop/Contributions/ACC17.pdf. 126

[75] R. Pausch. Magnetic Fields of the Optical Matching Devices Used in the Positron Source of the ILC. *DESY Summer Students Programme 2010*, 2010. http://www-zeuthen.desy.de/summerstudents/reports2010/final-report-rpausch.pdf. 127

[76] J. Elias-Miro. Positron Production for a Linear Collider. *University Autonoma de Barcelona*, 2010. 133

[77] W.R. Smythe. On Eddy Currents in a Rotating Disk. 1942. 133

[78] S. Antipov et al. Simulations of the Rotating Positron Target in the Presence of OMD Field. *Proceedings of PAC07*, 2007.
http://accelconf.web.cern.ch/accelconf/p07/PAPERS/THPMN087.PDF. 134

[79] I.R. Bailey et al. A Study of Mechanical and Magnetic Issues for a Prototype Positron Source Target. *Proceedings of EPAC08*, 2008.
http://accelconf.web.cern.ch/Accelconf/e08/papers/mopp072.pdf. 134

[80] I.R Bailey et al. A Prototype Target Wheel for the ILC Positron Source. *Proceedings of EPAC08*, 2008.
http://accelconf.web.cern.ch/accelconf/e08/papers/mopp069.pdf. 134

[81] I.R. Bailey et al. Eddy Current Studies from the Undulator-Based Positron Source Target Wheel Prototype. *Proceedings of IPAC10*, 2010.
http://accelconf.web.cern.ch/accelconf/IPAC10/papers/thpec033.pdf. 137

[82] Omega Engineering. Omega Torque Transducer TQ504 User's Guide. *User's Guide*. 139

[83] A.D Abramov et al. Eddy-current Loss in a Rotating Magnetic Field. *Russian Physics Journal*, 14:25–28, 1971.
http://dx.doi.org/10.1007/BF00819855. 142

[84] S. Antipov et al. Numerical Studies of International Linear Collider Positron Target and Optical Matching Device Field Effect on Beam. *Journal of Applied Physics*, 2007.
http://ieeexplore.ieee.org/xpls/abs-all.jsp?arnumber=4944134&tag=1. xii, 144